Centre de Desenvolupament de Sensors, Instrumentació i Sistemes

Departament d'Òptica i Optometria

UNIVERSITAT POLITÈCNICA DE CATALUNYA

Adaptive Self-Mixing Interferometry for Metrology Applications

Reza Atashkhooei

A thesis submitted in fulfillment of the requirements for award of the degree

Doctor of Philosophy

in

Optical Engineering

Thesis advisor:

Dr. Santiago Royo

Terrassa, 2013

UNIVERSITAT POLITÈCNICA DE CATALUNYA
BARCELONATECH
Escola de Doctorat

Acta de qualificació de tesi doctoral

Curs acadèmic: 2012-2013

Nom i cognoms: REZA ATASHKHOOEI

DNI / NIE / Passaport: X9166250Z

Programa de doctorat: INGENIERÍA ÓPTICA

Unitat estructural responsable del programa: DEPARTAMENTO DE ÓPTICA Y OPTOMETRÍA

Resolució del Tribunal

Reunit el Tribunal designat a l'efecte, el doctorand / la doctoranda exposa el tema de la seva tesi doctoral titulada ADAPTIVE SELF-MIXING INTERFEROMETRY FOR METROLOGY APPLICATIONS.
Acabada la lectura i després de donar resposta a les qüestions formulades pels membres titulars del tribunal, aquest atorga la qualificació:

☐ APTA/E ☐ NO APTA/E

(Nom, cognoms i signatura)	(Nom, cognoms i signatura)
President/a	Secretari/ària

(Nom, cognoms i signatura)	(Nom, cognoms i signatura)	(Nom, cognoms i signatura)
Vocal	Vocal	Vocal

_____, _____ d'/de _____ de _____

El resultat de l'escrutini dels vots emesos pels membres titulars del tribunal, efectuat per l'Escola de Doctorat, a instància de la Comissió de Doctorat de la UPC, atorga la MENCIÓ CUM LAUDE:

☐ SÍ ☐ NO

(Nom, cognoms i signatura)	(Nom, cognoms i signatura)
Presidenta de la Comissió de Doctorat	Secretària de la Comissió de Doctorat

Barcelona, _____ d'/de _____ de _____

Santiago Royo, Catedrático de Universidad de la Universidad Politécnica de Cataluña

CERTIFICA

que Reza Atashkhooei, Licenciado en Física Aplicada, ha realizado bajo su dirección, encuadrado en el programa de Doctorado de Ingeniería Óptica del Departamento de Óptica y Optometría de la Universidad Politécnica de Cataluña, el trabajo:

"Adaptive Self-mixing Interferometry for Metrology Applications"

para optar al grado de Doctor por la Universidad Politécnica de Cataluña.

Y para que conste, de acuerdo con la legislación vigente, firma el presente certificado,

Santiago Royo

Terrassa, 2013

Acknowledgements

First and foremost, I would like to show my deepest gratitude to my supervisor, Dr. Santiago Royo, respectable, responsible and resourceful scholar, who has provided me with valuable guidance at every stage of this Thesis. Without his enlightened instructions, impressive kindness and patient, I could not have completed my thesis. His keen and vigorous academic observation enlightens me not only in the present thesis but also in my future career.

I would like to express my gratitude to Dr. Ferran Laguarta Bertran from Technical University of Catalonia, and Dr. Mario Montes Usategui from University of Barcelona, who kindly accepted to review my research work despite their busy schedules at this time of the year. I am also honoured by presence of Dr. Dragan Indjin from University of Leeds who has kindly accepted to be a part of the jury.

I would also like to thank Dr. Thierry Bosch and Dr. Usman Zabit for their kind support in my research activities. It was a great pleasure collaborating with them and I deeply appreciate their warm personalities.

I shall extend my thanks to the staff of CD6 research centre (Centre for Sensors, Instruments, and Systems development (CD6-UPC)) for their great technical assistance. I would particularly like to thank Xavier Murcia Navarro of the Mechanical Workshop and Fermín Alarcón Escobar of the Electronics Workshop for their help in the design and fabrication of the mechanical and electrical parts needed for my experiments. I am also indebted to the technical support and friendly encouragement of Jordi Riu and Jordi Segura. I would specially like to thanks the administration staff of CD6, Cristina Cusidó Masip, Rosa Maria Sanchez Valero, Maite Masana, Alicia Sanchez Nabau and Teresa Solé Murillo.

I am also thankful for the good humor and patience of my colleagues in the Lab., Irina Sergievskaya, Miguel Ares Rodriguez, Mikel Aldaba Arévalo, Cristina Martínez González, Harold Zuluaga, Carlos Garcia, Anna Giner Tort, Francisco Javier Burgos Fernández, and my fellow PhD students, Francisco Javier Azcona, Jorge Mendez, Ajit Jha.

Last but not least, on a personal note, what I feel for my parents, my mother Shaheen and my father Ali, is more profound than mere words. They have sacrificed a lot during my research abroad. Without their encouragement and understanding, it would have been impossible for me to finish this work. I hope that my work will be a source of happiness for them even if I have wavered along the way. I would also like to express my special gratitude to Afsaneh, Afshin, Neda, my siblings, my best friends all my life, for their loving and endless support.

Abstract

Within the category of optical interferometers, optical feedback interferometry, also known as self-mixing interferometry, has recently shown a great potential in a large range of metrology applications as it is compact in size, cost effective, robust, self-aligned, and simple. In this phenomenon, a portion of the emitted laser beam re-enters to the laser cavity after backreflection from the target, causing the wavelength of the laser to change, modifying the power spectrum and consequently the emitted output power, which can be detected for measurement purposes. In such a setup, the laser operates simultaneously as the light source, the light detector, and a compact coherent detector. It is thus a compact and self-aligned micro-interferometer.

The present PhD pursued improving the performance of optical feedback interferometry based sensors using a novel and compact optical system. A solution using an adaptive optical element in the form of a voltage programmable liquid lens was proposed for automated focus adjustments. The amount of backreflected light re-entering the laser cavity could be controlled, and the laser feedback level was adjusted to the best condition in different situations. Feedback control enabled the proposal of a novel solution called differential optical feedback interferometry, which improved the measurement resolution down to nanometre order, even if the displacements were below half-wavelength of the laser, for first time in this type of sensors. Also, two novel solutions have been proposed for the control of the speckle effect which appears when the displacements of the target are large. The adaptive optical head developed has been used in real time to control the presence of speckle effect by tracking the signal to noise ratio of the emitted power of the laser and modifying the spot size if required, using a feedback loop. Besides, a sensor diversity solution has been proposed to enable enhancements in signal detection in fast targets, when real time control cannot be applied. Finally, two industrial applications of the technique with the presence of some sort of speckle noise have been presented. A complete measurement procedure for the control of motor shaft runout in permanent magnet electrical motors, enabling complete monitoring of the displacement of the shaft has been developed and implemented in practice. A second application in the monitoring of polymer-reinforced beams used in civil engineering under dynamic loading was also demonstrated.

This PhD, thus, has contributed to the field of optical feedback interferometry sensors through the development of an optics-based adaptive solution enabling, for the first time, the real time control of feedback level and (for slow-moving targets) of speckle noise. Enhancement of speckled signals using diversity techniques has also been demonstrated. Besides, novel research lines emerge from this Thesis, in particular out of the suggestion of a novel high resolution technique based in differential optical feedback interferometry.

Key words: Self-mixing, Optical feedback, Interferometry, Adaptive optics, feedback control, differential interferometry, speckle control, sensor diversity, shaft runout tracking, beam deformation measurement.

Table of Contents

List of Figures

List of Tables

List of Abbreviations

Abbreviation	Description
2D	Two-dimensional
3D	Three-dimensional
ADC	Analog to digital converter
AFM	Atomic force microscopy
AGC	Automatic gain control
AOH	Adaptive optical head
BF	Back-facet
BST	Bright speckle tracking
DOFI	Differential optical feedback interferometry
FCM	Fringe counting method
FF	Front-facet
FFT	Fast Fourier Transform
FL	Focusing lens
FPGA	Field programmable gate array
FPLD	Fabry-Perot cavity LD
FWHM	Full width at half maximum
GFRP	Glass Fiber Reinforced Polymer
LD	Laser diode
LDV	Laser Doppler velocimetry
LEF	Linewidth enhancement factor
LL	Liquid lens
LPF	Low-pass filter
LVDT	Linear vertical differential transducer
MEMS	Micro-electro-mechanical systems
OFI	Optical feedback interferometry
OOP	Optical output power
PD	Photodiode
PI	Physik Instrumente
PMSM	Permanent magnet synchronous motor
PUM	Phase-unwrapping method
PZT	Piezoelectric transducer
RMS	Root mean square
SMI	Self-mixing interferometry
SNR	Signal to noise ratio
VCSEL	Vertical-cavity surface-emitting laser
WFE	wave front error

1. Introduction

The use of laser based techniques, among other techniques and solutions proposed for metrology applications, is constantly increasing due to their non-contact nature and the measurement precisions attainable. Among the available laser based sensors in the market, classical interferometers offer the highest precision measurements. However, the cost of some of the elements involved and the number of optical components used in the setup complicates using them in several industrial applications. Moreover, optical alignment and the required quality of the environmental conditions can be quite restrictive for those systems and add complexity to the measurement process.

Within the category of optical interferometers, optical feedback interferometry (OFI), also called self-mixing interferometry (SMI) has the potential to overcome some of the complexities of classical interferometry, as it is compact in size, cost effective, robust, self-aligned, and it doesn't require a large number of optical components in the experimental configuration. Besides, it provides accuracies which are useful in a range of relevant applications. In OFI, the emitted laser beam from the cavity is backreflected from a (typically diffusive) target and part of the initial beam re-enters the laser cavity. This feedback interferes inside the laser medium modifying the lasing wavelength and leading to modifications in the power spectrum, which introduce changes in the emitted power. Usually, an embedded photodetector monitors the intensity of the laser beam, whose information is later used to extract the information about the state of the target (velocity, displacement, distance...) out of the abovementioned changes in the optical output power (OOP). The compact experimental configuration of OFI typically includes the laser itself, normally a solid-state one, a monitor photodiode normally embedded within the laser package, and a focusing lens to focus the laser beam on the target surface. This simplicity makes it very attractive from the industrial point of view.

In the past decade, a big effort has been made to improve the measurement resolution of OFI and to increase its measurement range, which is limited, among other factors, by the speckle phenomenon. There is still a drawback in OFI setups which is the need for a skilled operator to adjust the beam focus on the target to get the desired amount of backreflection of the laser beam (and subsequently to get the desired feedback level) for correct measurements. Depending on the characteristics of the target surface, to have the desired amount of beam reflection in the laser cavity (not so weak to lose the feedback signal, not so strong to bring the laser to chaotic states) the laser beam may need to be defocused or focused on the target, a procedure manually done by adjusting the relative position of the focusing lens against the front facet of the laser.

In the present thesis, a novel solution which uses an adaptive optical element in the form of a voltage programmable liquid lens is proposed for automated focus adjustments. It is shown that by using this novel optical element, the amount of backreflected light which re-enters the laser cavity can be controlled, and subsequently the laser feedback level can be adjusted to the best measurement condition. This enables

OFI to be used in operator-free conditions, for the first time to our knowledge, using adaptive control of the feedback level.

Also, we propose the use of adaptive feedback control in one relevant application called differential optical feedback interferometry (DOFI), a double laser solution proposed in this thesis for the first time. DOFI improves the measurement resolution and performance of OFI down to the nanometre level, pretty far below the typical resolutions of the basic technique. DOFI also enables for the first time measurement of phenomena where changes in the optical path are below the half-wavelength limit present in all OFI applications. This new technique combines the signals from two lasers, one vibrating on a piezoelectric linear stage while pointing at the target, and another one (stationary) pointing to the linear stage. Differences from the signals in both lasers enable to extract sub-wavelength displacements of the target. However, for the system to achieve the best performance, both lasers should have the same feedback level, so the adaptive solution presented in this thesis can be used to properly adjust feedback level of each laser to the desired value. However, due to the complexity of the detailed experimental setup the proposal of the technique and its feasibility check are included, although its detailed modelling, implementation, validation and application is left as future work.

Furthermore, the same adaptive solution which has been used to deal with feedback level control has also been applied to control the speckle effect which appears in large displacements of the target. To our knowledge, this adaptive solution is the second practical solution ever described for speckle management. Thus, a real-time solution for speckle control including a feedback loop for controlling the signal to noise ratio (SNR) of the OOP along a displacement of the target of some centimetres is presented. Since the time response of the adaptive lens to focus change is limited to 80ms, the solution will not be suitable for fast displacements of the target, where an alternative technique (sensor diversity) will be proposed. Sensor diversity in OFI is proposed to combine the signal obtained from two lasers simultaneously, each of them under different measurement conditions and yielding different speckle patterns which combined, improve the accuracy of the measurements.

As real-world applications of speckle control situations, two industrial applications of OFI in which the speckle effect limits the measurement range, are demonstrated to show the applicability of the solution. One of the applications is a detailed methodology for shaft runout tracking in electric motors, which shows that, with controlled speckle features, OFI performs adequately as a non-contact proximity probe with resolution limited by the constraints defined by the setup, not the technique. A full procedure for the measurement including compensation techniques for typical experimental problems, and a validation using a commercial laser Doppler vibrometer with a much higher cost is presented. A second application involving the measurement of deformation in composite reinforced beams due to dynamic loads, typically used in civil engineering, is also described in detail. Again, results obtained using OFI are validated against a conventional linear vertical differential transducer (LVDT), a contact probe, yielding adequate results.

Thereby, the main work of this thesis deals with feedback control and speckle control using the adaptive solution presented, and its related applications. The rest of the thesis has been divided in five additional chapters, subdivided in a small number of sections, and organized as follows.

The second chapter has been dedicated to present the theoretical foundations of OFI. In the first section of this chapter, the theoretical basis of OFI is generally introduced and the applications of OFI in various fields are presented. Later in the second section, the theoretical model describing the phase equation, the output power of the laser, and the effective parameters affecting the feedback interference will be described. Then, in the third section, the different feedback levels and its corresponding shape of the optical power signal will be investigated. Afterwards, the fourth section reviews the most usual signal processing techniques used in OFI. Later, we will include a short section with a description of the speckle phenomena, its effect in the performance of the OFI sensor, and the available techniques described in the literature to deal with the speckle problem, in special when large displacements of the target are involved. We will close this Section with a brief conclusion.

The third chapter presents the research work performed within this Thesis around feedback control. It starts with the considerations on design and fabrication of the prototype of adaptive optical head which uses a liquid lens for adaptive feedback control, which later on will be also applied to speckle control. The second section of this chapter presents the results for feedback control in OFI using the optical head presented. In this section, the experimental configuration, the control algorithm, and the experimental results achieved are described in detail. The last section of this chapter is dedicated to proposing the DOFI technique, a double laser solution for accuracy requirements down to the nanometre level in which adaptive feedback control can be used to adjust the relative feedback levels and thus improve the performance of the technique. Again a brief conclusion section closes the chapter.

The fourth chapter presents the solutions for speckle control proposed to improve the performance of OFI in large displacement measurements. At first, the speckle effect and the effective parameters in the speckle characteristics are investigated in an OFI setup, and then a speckle control technique using the adaptive optical head proposed is demonstrated. To overcome the limitations of fast-moving targets, a sensor diversity solution for speckle control will be proposed as well. A brief conclusion will be the last section of this chapter.

In the fifth and final chapter, as applications of the speckle control solutions proposed, two specific applications of OFI sensors in conditions where the speckle effect may be present are presented. This includes a novel procedure for shaft runout measurement in electric motors, and a method for the measurement of beam deformations under dynamic loads. The last section of this chapter has been dedicated to a brief conclusion of this chapter.

A summary of the main conclusions of the work will be presented at the end of thesis in a sixth chapter, followed by the list of bibliographic references used and the list of publications achieved along this work.

2. Theoretical foundations

2.a. Basics of optical feedback interferometry

OFI has been extensively studied during the past decades [Kane 2006] [Donati 2004] and has been presented as a compromising solution for vibration, displacement, velocity and absolute distance measurement for a large range of applications [Donati 2012] [Ottoneli 2009].

The optical feedback interference or self-mixing phenomenon occurs when a small fraction of the emitted laser beam is back reflected from a moving target, and partially enters to the laser cavity, so this reflected light is mixed (self-mixed) with the standing wave present inside the laser medium. Due to the self-mixing of the beams inside the laser cavity, the frequency of the emission of the laser becomes modified and a periodic variation in the OOP of the laser occurs. Usually, this variation is monitored using a photodetector located at the back facet of the laser, as shown in Fig. 2.1. Different types of self-mixing signals may appear depending on the level of feedback present for each given experiment, and will be analyzed later.

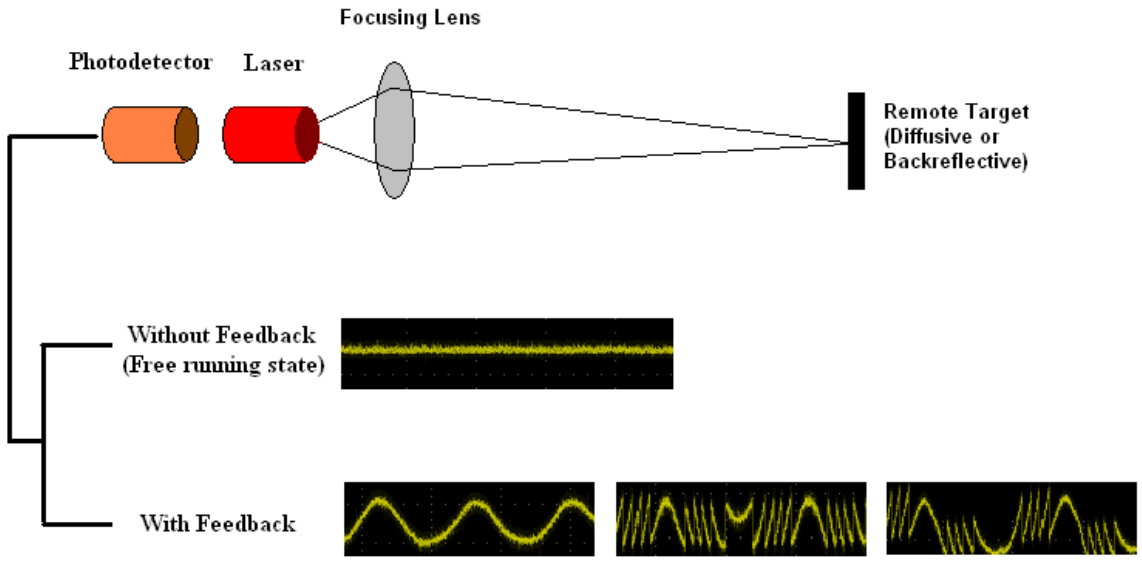

Figure 2.1. Schematic diagram of the typical OFI configuration. When part of the laser beam re-enters the cavity, the existent feedback level determines the shape of the OOP fluctuation (see section 2c).

OFI was first reported in gas lasers for detection of the Doppler shift due to the displacement of the remote reflector [Rudd 1968]. Later, it has been presented as a complete self-aligned interferometer for measurement purposes [Donati 1978]. Afterwards, it was demonstrated as a velocimeter using a semiconductor laser diode (LD) with a photodetector in the laser package [Shinohara 1986]. Many

different applications of OFI have appeared in the literature since then, and may be found elsewhere [Donati 2011] [Bosch 2006].

Semiconductor lasers represent a complete laser family with a very broad range of spectral outputs, narrow linewidths and single frequency emission. Moreover, many commercial laser diodes contain a monitor photodiode mounted in the same laser package to monitor the OOP of the laser in order to compensate the threshold current instability due to temperature variations. The integrated photodiode provides a direct method to monitor the OOP variations which appear due to interference with the backreflected beam, making semiconductor lasers exceptionally suited to OFI applications. A simpler approach has been presented based on sensing directly the variations of the junction voltage in semiconductor lasers under feedback has been proposed for sensing applications [Kliese 2008], although the signal to noise ratio gets worse than in case of using the monitor photodiode. It is also worth mentioning here that two different geometries of the cavity have been demonstrated in semiconductor lasers showing the OFI effect, namely Fabry-Perot cavity LDs (FPLDs) and vertical-cavity surface-emitting lasers (VCSELs) [Kane 2005] [Donati 2004]. Both are easily found in the market and present different performances. While FPLDs typically deliver larger amounts of power, VCSELs produce rounder, smaller spots due to their emission mechanism, thus enabling better focusing of the beam. In all cases, lasers need to be single mode and biased well above its threshold intensity value to have low side-mode content [Donati 2012].

In a typical OFI configuration, a collimating lens is the only optical element, required for focusing the beam on the target. However, free-lens OFI working in short distances (below 5cm) has also been reported [Perchoux 2010]. Thus, OFI sensors provide a robust, self-aligned, compact, and small in size sensing tool when compared to traditional double or common path interferometric setups, such as Michelson, Mach-Zehnder, Fizeau, or Sagnac [Hecht 2002]. Besides its compactness and self-alignment, the simplicity of the approach also makes it extremely cost-effective, making it especially suitable for industry-oriented applications.

A review of the main measurement configurations including displacement, velocity, absolute distance measurement and some other applications are briefly presented in the following paragraphs.

2.a.1. Displacement measurements

Many types of sensors have been developed for displacement measurements such as resistive, capacitive, inductive, magnetic, piezoelectric, ultrasonic and optical sensors [Wilson 2005] [Shieh 2001]. Among them, optical ones, including intensity-based sensors, triangulation, time of flight, confocal, Doppler or the different types of interferometric sensors have been extensively studied and developed due to their noncontact nature and high precision [Berkovic 2012]. OFI sensors have been exploited in particular in displacement measurements as they represent a compromising solution within the optical sensor family

when considering cost, simplicity, compactness, precision and robustness [Norgia 2003] [Servagent 1998].

In OFI, when the LD is pointed to a fixed target (with no movement), the frequency and the OOP of the laser remain constant. Unlikely, changing the distance between the target and the laser leads to variation of the spectral properties and to OOP fluctuations of the laser. Figure 2.2 shows a typical experimental OOP variation due to a sinusoidal displacement of the target.

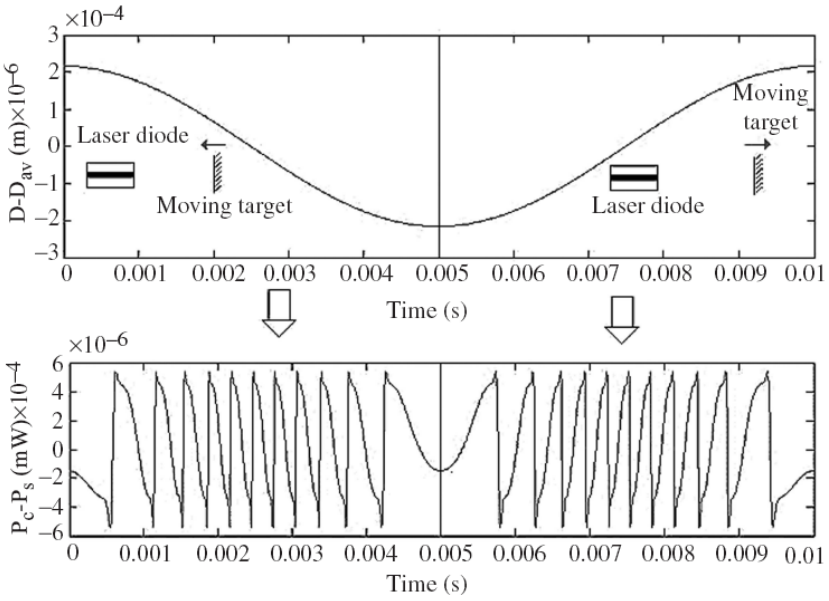

Figure 2.2. Experimental saw-tooth variation of OOP (below) due to a sinusoidal displacement of the target (above) [Zabit 2010b].

Saw-tooth like fluctuations of the OOP have been generated due to the variation of the distance to the target, that is, to the existence of changes in the optical path between the laser and the target. The OOP of the LD subject to feedback (P) can be expressed as [Bosch 2001]

$$P = P_s(1 + m.\cos\varphi_c) \tag{2.1}$$

Where P_s is the power of the laser in the free running state, the parameter m is the modulation coefficient of the optical feedback interference, and $\varphi_c = 2\pi v_c \tau_D$ is the phase of the optical power signal of the LD, where v_c is the optical frequency of the laser under feedback, $\tau_D = 2D/c$ is the external round trip delay with D being the distance to the target from the front facet of the LD and c the speed of light. In similarity with conventional interferometric techniques, every fringe period which appears in the OOP corresponds to a 2π phase shift which corresponds to a half-wavelength ($\lambda/2$, with λ the laser wavelength) change of optical path difference [Norgia 2003] following

$$|\Delta(2\pi\, v_c\, \tau_D)| = 2\pi \;\Leftrightarrow\; 2(\Delta D)\, v_c = c \;\Leftrightarrow\; \Delta D = c/2v_c = \lambda / 2 \tag{2.2}$$

where ΔD is the displacement of the target which generates a 2π phase shift in the power signal. The easiest way to measure the displacement of the considered target out of the OOP fluctuations is thus the fringe counting method (FCM) which allows to measure the displacement with half-wavelength resolution (see subsection 2.d.2.1) [Donati 1995].

Several methods have been developed for increasing the basic half-wavelength resolution of displacement measurements in OFI. A linear interpolation method was developed in 1998 by Servagent et al [Servagent 1998] applying linear interpolation of inter-fringe values for saw-tooth like OOP variations, enabling a resolution of $\lambda/12$ for displacements up to several micrometres. However, this method is limited to moderate feedback regime. Another approach is the active heterodyne technique which uses a pair of LDs, each one with its own external cavity [Takahashi 1996]. In this approach, the first LD is the reference laser and the other is used for target displacement detection. To estimate the displacement, a heterodyne arrangement including an avalanche photodiode, a spectrum analyser and a microwave counter was used to measure the heterodyne beat frequency. A resolution of 5nm was reported for this approach.

Two more very powerful methods for displacement reconstruction were proposed by Merlo and Donati [Merlo 1997] and Bes [Bes 2006] in order to enhance the accuracy of measurements obtained. Both methods are discussed in more detail in subsecion 2.d.2, where the most relevant signal processing algorithms for displacement reconstruction are presented in detail Although the signal processing involved usually carries on a relevant computing load and each algorithm has some applicability limits which need be taken into account, these techniques have been shown to reduce the attainable accuracy to the order of some tenths of nanometre for displacements of a few microns.

Other more robust and reliable solutions have been proposed, but they tend to be complex to implement and interpret. As an example, a technique based on a differential evolutionary algorithm [Doncescu 2007] has been proposed for noisy signal processing of OFI signals.

2.a.2. Velocity measurements

As already mentioned, velocimetry was in fact the first application of OFI (in a gas laser) as early as 1968 [Rudd 1968]. Optical feedback interferometry is well suited in the category of laser Doppler velocimetry (LDV), where they represent a compromising solution when compared to conventional velocimeters due to its already discussed features [Scalise 2004].

Velocity measurement in OFI is based on the detection of the Doppler frequency in the recovered signal, which is related to the velocity of the target by a simple expression like

$$F_D = \frac{2V_F}{\lambda} \tag{2.3}$$

where V_F is the velocity of target relative to the laser in the direction of the beam, and F_D is the Doppler frequency, which corresponds to the frequency of the saw-tooth like OOP variations of the LD under feedback caused by the moving target. The Doppler frequency can be easily recovered applying a Fast Fourier Transform (FFT) to the OOP of the LD, or using a FFT oscilloscope in real time.

Figure 2.3 shows a typical experimental result where a FFT has been directly applied to the OOP of the LD under feedback [Scalise 2004]. In this example, the target is a rotating disc with a white rough front surface rotating with constant velocity, with its surface tilted 30º relative to the optical axis of the laser. The Doppler frequency in this signal appears as a peak in the Doppler spectra at 24.3KHz, corresponding to a velocity of 11.6mm/s. Actually, obtaining the velocity using OFI is quite simple as after applying the FFT to the acquired OOP, the Doppler frequency corresponds to the maximum amplitude in the spectrum, and velocity can be directly determined using equation (2.3).

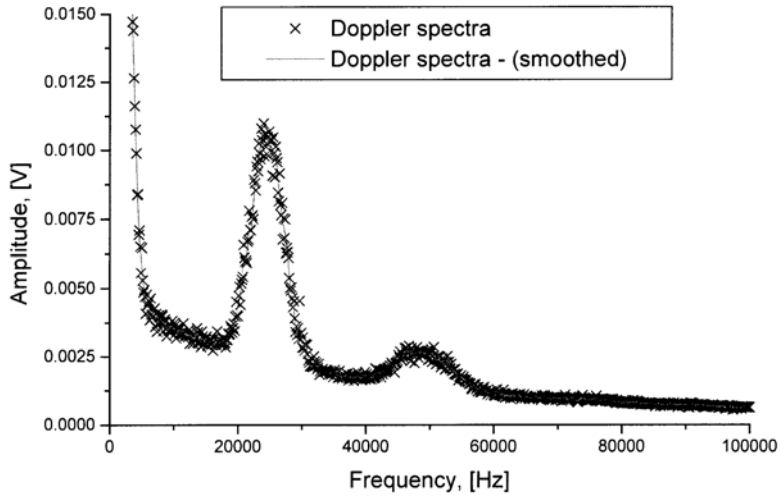

Figure 2.3. Doppler signal obtained from an OFI based laser Doppler velocimeter. Crosses are the values of FFT out of the experimental OOP, and the solid line an smoothed spectra obtained using a seven-point adjacent averaging method [Scalise 2004].

OFI is thus an excellent candidate for a simple, low-cost velocimetry sensor [Krehut 2003]. Target velocities can be determined with maximum relative errors of 5% for velocities up to 200km/h [Bosch 2001]. This approach has been thoroughly reviewed, including an extended external cavity model, for the development of OFI based applications in microfluidics [Campagnolo 2013].

For applications subject to temperature variations which lead to laser wavelength instability, and subsequently to an increase of the experimental error, VCSEL-based OFI is more reliable than the equivalent FPLD-based sensors at short distances (below 50cm) [Perchoux 2007]. VCSELs are in general less sensitive to temperature variations and have a very low threshold current and price, which makes them very good candidates for on-board automotive velocimeters.

2.a.3. Absolute distance measurement

Several laser range finder techniques have been developed for absolute distance measurements, rather than just the relative measurements we described in Section 2.a.1. They are broadly classified in families including geometrical or triangulation, time-of-flight, and interferometric techniques [Amann 2001]. Among them, interferometric techniques are the most accurate ones at the price of being very expensive solutions not easy to implement at all. OFI belongs to the family of interferometric techniques but is more attractive due to its low-cost approach and compactness. Recently, an absolute distance sensor based on OFI with a working range of 3m and an accuracy of 0.3mm was reported by Norgia et al [Norgia 2007].

In the previously described setups, the displacement of the target modulates the emission wavelength of the LD leading to fluctuations in OOP. Unlikely, in absolute distance measurement the target is stationary, so the optical path length of the laser beam in the external cavity is constant during the measurement. In order to measure distance, the LD emission wavelength is modified using a triangular waveform modulation of the injection current, so we can produce interferometric fringes fully equivalent to the ones introduced by optical path length variations [Gouaux 1998]. In this case, however, they are induced by the changes of wavelength in the laser cavity caused by the modulation of the incoming current. In fact, OOP variations are superimposed to the triangular waveform, as shown in Fig. 2.4.

Applying a triangular current modulation, and, consequently having a wavelength variation of $\Delta\lambda$ leads to a modification of the wave number ($k=2\pi/\lambda$) in the shape of

$$\Delta k = 2\pi \frac{\Delta\lambda}{\lambda^2} \tag{2.4}$$

where $\Delta\lambda$ depends on the electrical characteristics of the laser diode. Therefore, the wave number variation results in an optical phase change of $\Delta\varphi$ in a round trip of:

$$\Delta\varphi = \Delta k \cdot (2s) = 4\pi \frac{\Delta\lambda}{\lambda^2}.s \tag{2.5}$$

where s is the distance from the front facet of the laser to the stationary target.

Thus, now we can easily relate phase changes directly with the absolute distance to the target, s. Since every 2π change of the phase corresponds to a fringe in the signal, therefore the phase change for the number of fringes (N) appearing in the OOP will be $\Delta\varphi = 2\pi N$. Thereby, the target distance can be obtained simply by counting the number of fringes (N) in the acquired OOP and using the following relationship

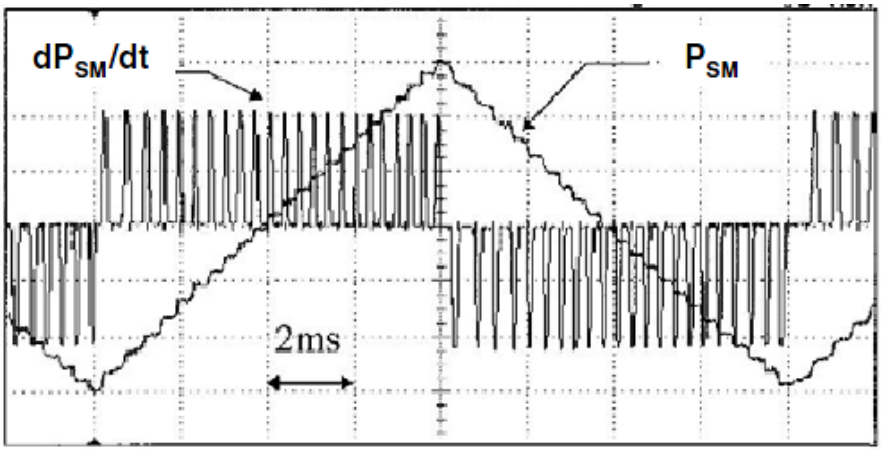

Figure 2.4. OOP of the LD (P_{SM}) obtained from the current-modulated OFI sensor and its derivative for absolute distance measurement [Giuliani 2002].

$$s = N\frac{\lambda^2}{2\Delta\lambda} \tag{2.6}$$

The resolution of this method is limited to the fringe quantization error of $\lambda^2/2\Delta\lambda$. Obviously, the resolution depends on the wavelength shift of the laser and on the wavelength itself.

2.a.4. Other applications

In addition to the main general-purpose applications of OFI described before, some other applications have been proposed along the last years. In this Section we are going to briefly review them grouped in five different general categories.

2.a.4.1. Surface profile measurement

One family of OFI applications is three-dimensional (3D) imaging and surface profile measurement. 3D imaging based on the absolute distance measurement was developed by Bosch et al in 1998 [Bosch 1998]. In this method, the surface distance from the laser has been measured point by point with 0.1% vertical resolution in a 1-3m distance range. OFI has also been combined with confocal microscopy to measure the surface microprofile in different approaches from several authors [Wang 2004] [Juskaitis 1994] [Rea 1996]. Surface classification based on the speckle modulation in OFI has also been reported [Ozdemir 2001]. This application takes advantage of the relationship existing between the speckle modulation frequency induced in the OFI signal and surface characteristics like texture, reflectivity and roughness.

2.a.4.2. Measurement of physical parameters

OFI-based measurements of physical quantities such as thickness of a transparent slab with accuracy comparable to a mechanical calliper [Fathi 2010], simultaneous estimation of yaw, pitch (two rotation angles) and linear displacement as a 3 degree-of-freedom motion sensor with half-wavelength resolution

[Ottonelli 2008], and integral strain characterization of materials under mechanical and thermal deformations with submicron resolution [Dabbicco 2011] have been reported.

As a different but much related family of applications, different laser-related parameters characteristic of semiconductor lasers, such as linewidth [Giuliani 2000], or the linewidth enhancement factor (LEF) [Yu 2004] [Villafranca 2008] have been measured using the OFI technique.

2.a.4.3. Biomedical applications

Due to its cost-effectiveness, and the capacity of red and infrared light to penetrate the surface of the skin, several in-vivo biomedical applications of OFI have been proposed. Amongst them, measurements of the shape of the arterial pulse wave [Hast 2002], of blood cell velocity distribution in microchannels [Campagnolo 2012] [Campagnolo 2012b], of the amount of blood flow [Koelink 1994], and of muscle amplitude of vibration [Mul 1992] have been performed. A low-cost instrument based on OFI for real time measurement of blood flow, particularly developed for extracorporeal blood circulator systems has been designed and presented by Norgia [Norgia 2010]. Also, OFI has been used to reduce the motion artifacts which appear in pulse oximeters measuring the patient's heart rate and blood oxygenation [Wijshoff 2012].

2.a.4.4. Sensors for specific applications

A scroll sensor based on OFI for the detection of multidirectional motion has also been introduced by Liess [Liess 2002]. Moreover, by applying it to the finger surface, an input device has been demonstrated for hand-held applications with performance comparable to a computer mouse [Pruijmboom 2008]. Besides, OFI has been used as a height control sensor for near-field data storage applications [Fang 2007].

2.a.4.5. Characterization of sensor performance

Another wide field of application has been the characterization of the performance of different types of sensors. OFI has been applied to measure mechanical resonance and to characterize the mass-spring system in different types of micro-electro-mechanical systems (MEMS) [Annovazzi-Lodi 2001] [Annovazzi-Lodi 2003]. Moreover, OFI has been used for absolute calibration of measurement microphones as a laser pistonphone [Sadikoglu 2004].

Therefore, we can conclude that OFI has been used in an expanding range of applications in the vibrometry, displacement and velocity sensing fields in the late years. Its wide applicability, accuracy, self-alignment and cost, and the characteristics of its measurement principle make it a very practical solution for a wide scope of applications in the science and industrial arenas.

2.b. Theoretical model

In order to investigate the physical principle of OFI, and to see how the laser frequency and OOP are changing due to the optical feedback interference, the behaviour of the laser subject to feedback has to be compared with the laser behaviour in its free running state (without feedback). The equivalent cavity model is a general-purpose model enabling to explain most of the effects present in OFI, and to introduce most of its relevant parameters. For setting up the model, at first we will obtain a description of the lasing condition without feedback taking into consideration the main effects in the cavity when no feedback is present. Then, we will modify the cavity in order to take into account external feedback effects, so we can model how the laser frequency changes under feedback. We will then be able to describe and formulate the OOP variations in presence of feedback interference and see which are the most relevant parameters involved. In its normal free running state, without feedback involved, the lasing medium can be modelled as a two-facet Fabry-Perot cavity with a length l (Fig. 2.5). Based on the classical definition of the reflection coefficient at an interface [Hecht 2002], the relationship between the electrical fields inside the laser cavity can be established as

On the back-facet (BF) interface: $$E_{1\to 2}(z=0) = r_1' \cdot E_{2\to 1}(z=0) \tag{2.7}$$

On the front-facet (FF) interface: $$E_{2\to 1}(z=l) = r_2 \cdot E_{1\to 2}(z=l) \tag{2.8}$$

Where r'_1 and r_2 are reflection coefficients of the electric field at the BF and FF of the cavity, respectively, $E_{1\to 2}(z = 0)$ is the electrical field travelling from BF to FF at BF interface, $E_{2\to 1}(z = 0)$ is the travelling electrical field from FF to BF at BF interface, and $E_{1\to 2}(z = l)$ is the travelling electrical field from BF to FF at FF interface; finally, $E_{2\to 1}(z = l)$ is the electrical field travelling from FF to BF at FF interface.

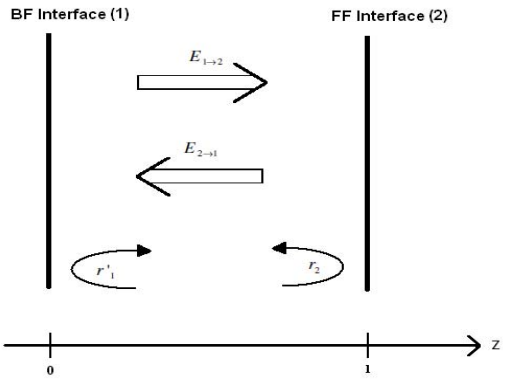

Figure 2.5. Schematic arrangement of a Fabry-Perot cavity in the free running state.

The electrical fields propagating along z-axis can be then expressed as [Hecht 2002]:

$$E_{1\to 2}(z) = E_{1\to 2}(0)\exp(-j\beta z - \frac{\gamma z}{2}) \tag{2.9}$$

$$E_{2\to 1}(z) = E_{2\to 1}(l)\exp(-j\beta(l-z) - \frac{\gamma(l-z)}{2}) \tag{2.10}$$

Where β is the propagation constant and γ is the absorption coefficient of the active medium. From equations (2.7) to (2.10), it can be seen that the emission condition for sustained laser oscillation in a two-facet cavity can be described as

$$r_1' r_2 \exp(-j\beta l - \gamma l) = 1 \tag{2.11}$$

which of course is the classical free-running state lasing condition required for the sustainability of the stationary wave inside the laser cavity.

In OFI, however, there are three relevant interfaces with noticeable reflections, which include the two facets of the laser as before, but also a second cavity defined by the target surface. Thus, two separate cavities can be considered for the lasing condition: the internal cavity, already present in the free running state condition, plus an external cavity formed by the target surface and the front facet of the laser, as shown in Fig. 2.6.

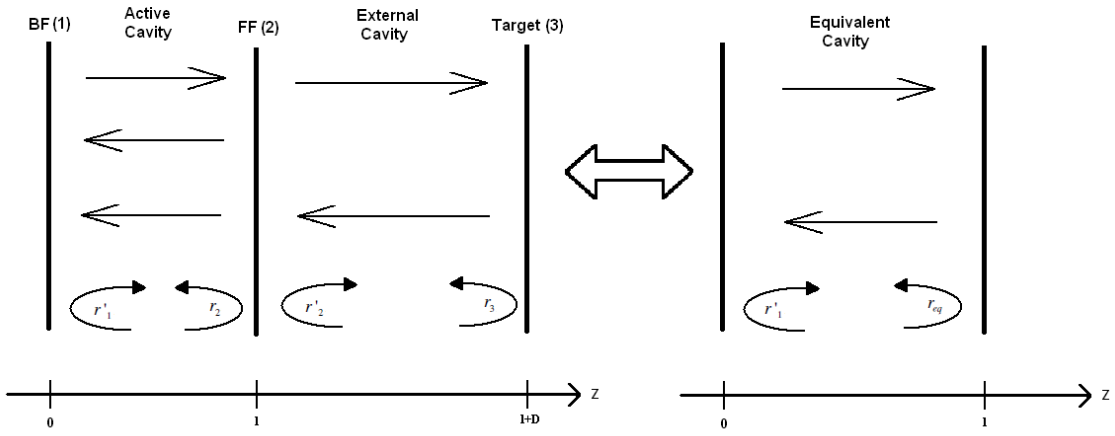

Figure 2.6. Schematic arrangement of internal, external and equivalent cavities.

In order to attain the final model of the laser subject to feedback, a single equivalent cavity is considered as the combination of the performance of the internal and external cavities (Fig. 2.6). In this model, multiple reflections within the external cavity are neglected due to the assumption of small target reflectivity ($r_3 << r_2$).Thereby, the equivalent complex amplitude reflectivity (r_{eq}) is obtained from [Bosch 2006]

$$r_{eq} = r_2.[1 + \kappa.\exp(-2j\pi\nu_c\tau_D)] \tag{2.12}$$

Wherein

$$\kappa = \varepsilon \frac{r_3}{r_2}(1 - r_2^{\,2}) \tag{2.13}$$

Where κ is the feedback coupling coefficient and ε is the mode mismatch factor, a parameter accounting for the fraction of reflected light re-entering into the active cavity. In this fashion the laser under feedback is reduced to a single equivalent cavity with length l, where r'_1 and r_{eq} are the reflection coefficients of the back and front facets of the resultant cavity. So, by replacing r_2 in equation (2.11) by r_{eq} from equation (2.12), a modified emission condition for the equivalent cavity obtained when a laser is under feedback can be obtained in the shape of [Lang 1980]

$$\nu_c - \nu_s + \frac{C}{2\pi\tau_D}.\sin(2\pi\nu_c\tau_D + \arctan(\alpha)) = 0 \tag{2.14}$$

Where

$$C = \frac{\tau_D}{\tau_l}\kappa\sqrt{1+\alpha^2} \tag{2.15}$$

Where ν_s is the optical frequency of the laser in free running state, $\tau_l = 2\mu l/c$ is the active cavity round trip delay, μ is the group refractive index without feedback, and α is the LEF of the laser, which depends on the characteristics of the laser and can be measured experimentally [Villafranca 2008] [Henning 1983]. The parameter C is referred to as "coupling factor" and is related to the external feedback strength or feedback level present in the setup. It discriminates four well known feedback regimes described in the literature which are very weak, weak, moderate and strong feedback regimes [Tkach 1986], which will be detailed related to typical OOP signals in Section 2,c. . Equation (2.14) is also known as the phase equation in literature. Although the three-mirror approach discussed above reaches to the phase equation, there is a more detailed description, known as the Lang-Kobayashi equations which includes the carrier state concentration. Lang-Kobayashi set of equations are the most complete description of the dynamics of the single mode semiconductor laser subject to optical feedback effects. These detailed equations can be written as [Donati 2012] [Lang 1980]

$$\frac{dE}{dt} = \frac{1}{2}\left[G_N(N-N_0) - 1/\tau_p\right]E + \left(\frac{\kappa}{\tau_D}\right)E(t-\tau_D)\cos\left[2\pi\nu_s t + \varphi(t) - \varphi(t-\tau_D)\right]$$

$$\frac{d\varphi}{dt} = \frac{1}{2}\alpha\left[G_N(N-N_{thr}) - 1/\tau_p\right] + \left(\frac{\kappa}{\tau_D}\right)\frac{E(t-\tau_D)}{E(t)}\sin\left[2\pi\nu_s t + \varphi(t) - \varphi(t-\tau_D)\right] \tag{2.16}$$

$$\frac{dN}{dt} = J\eta/ed - N/\tau_r - G_N(N-N_0)E_0^{\,2}(t)$$

Where G_N is the modal gain, N the carrier density, N_{thr} the carrier density at threshold, N_0 the carrier density at inversion, τ_p the photon lifetime inside the cavity, τ_r the carrier lifetime, J the pumping current density, η the internal quantum efficiency on the active layer thickness d, and e the elementary charge of electron.

Although equations (2.16) are obviously more detailed than those attained from the equivalent cavity model, and much better suited to the description of the feedback phenomena in semiconductor lasers, it has been shown elsewhere that the steady-state solutions obtained are fully equivalent in both approaches. In particular, the frequency of emission of the semiconductor laser is described in both approaches from the phase equation (2.14).

Let's now investigate the relationship of the frequency shifts introduced by feedback with the OOP emitted from the laser. According to literature, the threshold current (I_{th}) of a semiconductor laser is the injected current which causes the gain in the cavity to become equal to the losses due to absorption and scattering inside the cavity. Therefore, once the gain reaches the threshold gain, lasing starts to occur. The threshold gain (g_{th}) is affected by feedback and has been shown to vary due to feedback interference as [Koelink 1992]

$$\Delta g_{th} = -\frac{\kappa}{D}\cos(2\pi\nu_c\tau_D) \tag{2.17}$$

Thus, the threshold current of the laser is changed due to the threshold gain variation. For weak optical feedback ($\kappa << 1$), the threshold current variation (ΔI_{th}) may be obtained from

$$\Delta I_{th} = \frac{eV}{T_s a\Gamma}\Delta g_{th} \tag{2.18}$$

Where V is the active volume of the laser cavity, T_s the spontaneous recombination rate, a the differential gain at threshold, and Γ the mode confinement factor.

Since the gain curve of the semiconductor laser is almost linear once above the threshold gain [Koelink 1992], thereby the OOP (P) of the laser operating above threshold gain can be obtained as [Coldren 1995]

$$p = \frac{\Omega h\nu}{e}(I_{op} - I_{th}) \tag{2.19}$$

Where Ω is the wall-plug efficiency of the laser, h is the Planck's constant, ν is the laser frequency, and I_{op} is the operating current of the laser. Thus, the OOP of the laser under feedback in which the threshold current variation is considered added to the threshold current can be written as

$$P = \frac{\eta h\nu}{e}(I_{op} - (I_{th} + \Delta I_{th})) \tag{2.20}$$

And by substitution of equations (2.17) and (2.18) into equation (2.20) yields

$$P = \frac{\eta h \nu_c (I_{op} - I_{th})}{e}\left(1 + \frac{eV\kappa}{T_s a \Gamma D (I_{op} - I_{th})}\cos\left(2\pi\nu_c \tau_D\right)\right) \tag{2.21}$$

A general simplified form of equation (2.21) is normally used in the literature, expressed as [Bosch 2001]

$$P = P_s\left(1 + m.\cos(2\pi\nu_c \tau_D)\right) \tag{2.22}$$

Equation 2.22 expresses the form of the signal which should be expected from the photodiode monitoring the OOP of the LD under feedback, which will be used as experimental data in most OFI setups. We will discuss about feedback levels and its effect on the shape of the OOP along the following subsection.

2.c. OFI under varying feedback levels

The behaviour of a single mode semiconductor laser under feedback has been extensively studied and modelled in the last decade [Plantier 2005] and the notable influence of C (the coupling factor, directly related to the level of feedback present) on the laser operation has been investigated in depth [Kane 2006] [Donati 2004].

Continuing our description from the phase equation, when the target starts to move, the optical path length of the external cavity becomes changed. The wavelength of the laser is slightly modified due to the optical feedback interference following the phase equation (equation (2.14)). The phase equation can be written as

$$\Delta\phi = \nu_c - \nu_s + \frac{C}{2\pi\tau_D}\cdot\sin(2\pi\nu_c\tau_D + \arctan(\alpha)) \tag{2.23}$$

where $\Delta\phi$ is called the excess phase, which is introduced due to the presence of feedback. Figure 2.7 shows the simulated plots of excess phase as a function of (ν_c – ν_s) for different values of the coupling factor C.

In order to satisfy both the phase equation and the lasing condition for a laser under feedback, one or more solutions for the emission frequency have to be found which set the excess phase to zero. Figure 2.7, the number of solutions is directly dependent on *C* value.

As illustrated, for $C < 1$, which corresponds to low feedback levels (blue plot), only one solution for emission frequency may be found corresponding to a single lasing mode. Differently, for values of $C > 1$, when the feedback is stronger, several solutions for the phase equation may be found. In this case the

laser works only in one of the solutions which normally corresponds to the mode with narrowest spectral width [Mourat 2006].

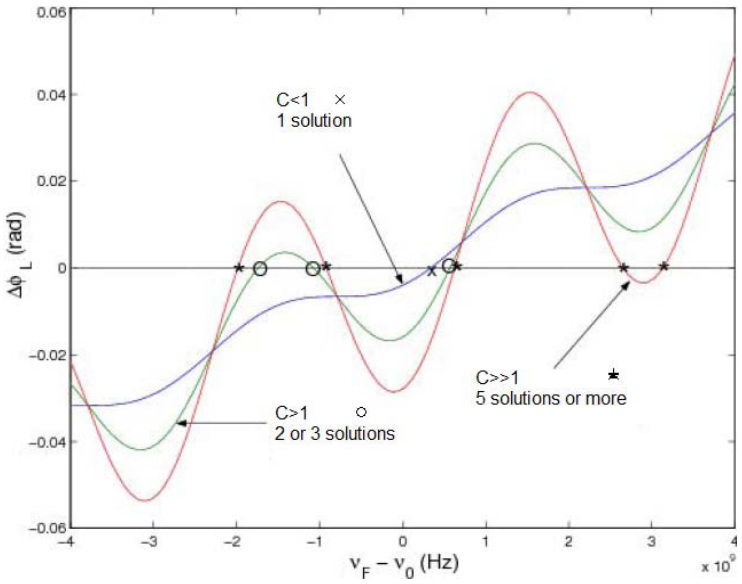

Figure 2.7. Simulation results of excess phase ($\Delta\phi$) versus change in the emission frequency ($\nu_c - \nu_s$, *which read* $\nu_F - \nu_0$ *in the figure*) for different feedback levels [El Assad 2008].

When the target distance changes or the injection current of the laser is modified, the emission frequency of the laser and the OOP vary according to equations (2.14) and (2.22). The shape of the OOP variation notably depends on C value, as shown in Fig. 2.8 where simulation results for the shape of the OOP signal are presented for different levels of feedback, assuming a sinusoidal displacement of the target [El Assad 2008].

Thereby C is a parameter of great importance in experimental arrangements, as it may be used to discriminate the four different levels of optical feedback manifested in the four different possible shapes of the OOP signal [Giuliani 2002]:

- For $0 < C < 0.1$, the very weak feedback regime appears. In this regime, OOP is a cosine periodic function according to equation (2.22), and there is a single solution to the excess phase. The SNR of the OOP signal is small in comparison with the SNRs which may be found in other regimes. The OOP is symmetrical and faces with directional ambiguity if used for displacement measurements, as far as it is impossible to distinguish the two directions of displacement. According to the definition of C (equation 2.15), this case may appear in very short target distances, or in the case of surfaces where back-reflected energy from the target is very small.

- For $0.1 < C < 1$, the weak feedback regime appears. In this regime there is still only one solution for the excess phase, but the fringes become distorted, and the OOP appears asymmetrical and saw-tooth like. The slope of the fringes contains the information on the direction of displacement of the target, and the SNR is much larger than in the very weak feedback regime.

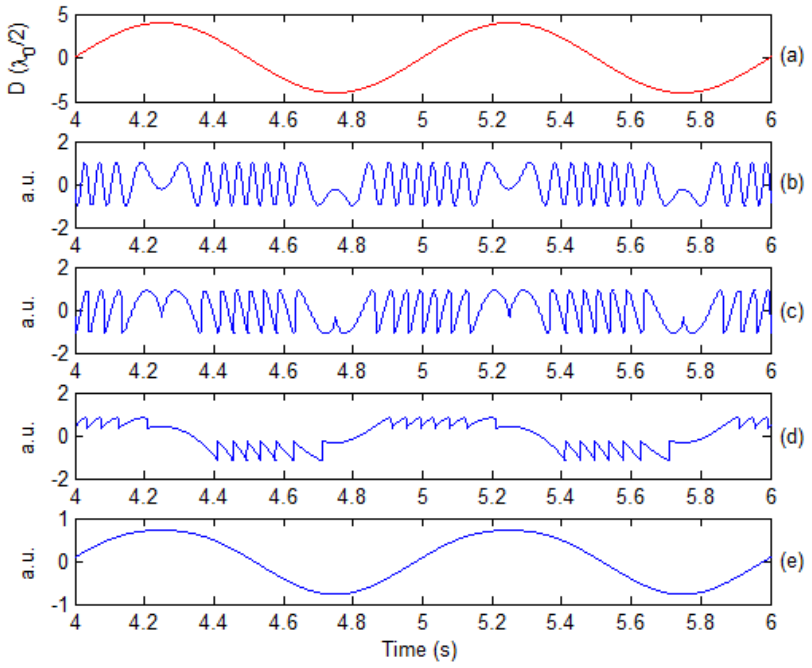

Figure 2.8. Simulated OOP of a laser under feedback for a sinusoidal displacement of the target and for different C values: (a) Displacement of the target; (b) C=0.1, (c) C=1, (d) C=7, (e) C=30 [El Assad 2008].

- For $1 < C < 4.6$, the moderate feedback regime is obtained. In this level, up to three solutions for phase equation can be obtained, so the shape of the OOP becomes saw-tooth like and exhibits hysteresis as the working solution of the phase equation may depend on the history of the experiment, distorting the measurement and leading to a fringe-loss condition. SNRs are comparable to those in the weak regime.

- For $C > 4.6$, we are considering the strong feedback regime. Usually this case can be obtained in large distances and with cooperative retro-reflective (corner cubes) or reflective (mirror-like) targets. In this regime, the number of solutions for phase equation can be more than three and subsequently the OOP shows from larger hysteresis. In some cases, even mode hopping between the possible solutions can take place leading to failure of the measurements.

For $C > 1$, when multiple solutions for the phase equation are found and the hysteresis increases, we may find the totally undesired fringe loss condition, which leads essentially to the disappearance of peaks in the OOP signal. In this case, we may obtain less fringes than expected in the achieved OOP, leading to significant inaccuracies in the measurements.

Interestingly, the fringe loss condition can be predicting using the feedback phase value combined with the corresponding coupling factor. The frontier condition which sets the limit in the number of solutions present in the phase equation may be shown to look like [Zabit 2010]

$$\Phi = (2k+1)\pi \pm \arccos\left(\frac{1}{C}\right) \mp C.\sin\left[\arccos\left(\frac{1}{C}\right)\right] \tag{2.24}$$

Where k is an integer and Φ is the feedback phase from equation (2.23) which can be depicted as

$$\Phi = 2\pi\nu_s\tau_D + \arctan(\alpha) \tag{2.25}$$

Figure 2.9 demonstrates the number of fringes (N) occurring when $C > 1$ in a given experiment, for certain sets of (C,Φ) pairs. In the considered experiment, the target displacement amplitude was set to 6λ, corresponding to an expected value of 12 fringes in the OOP signal. The position of the target was kept constant along the experiment.

For a fixed Φ value, it may be observed how a variation in C of 2π leads to the undesired disappearance of two fringes. Differently, for a fixed C value, changing the value of Φ will result in the disappearance of a single fringe. As a consequence, it is evident that the combined values of C and Φ need be taken into account to predict the appearance of the fringe loss condition [Tartwijk 1995].

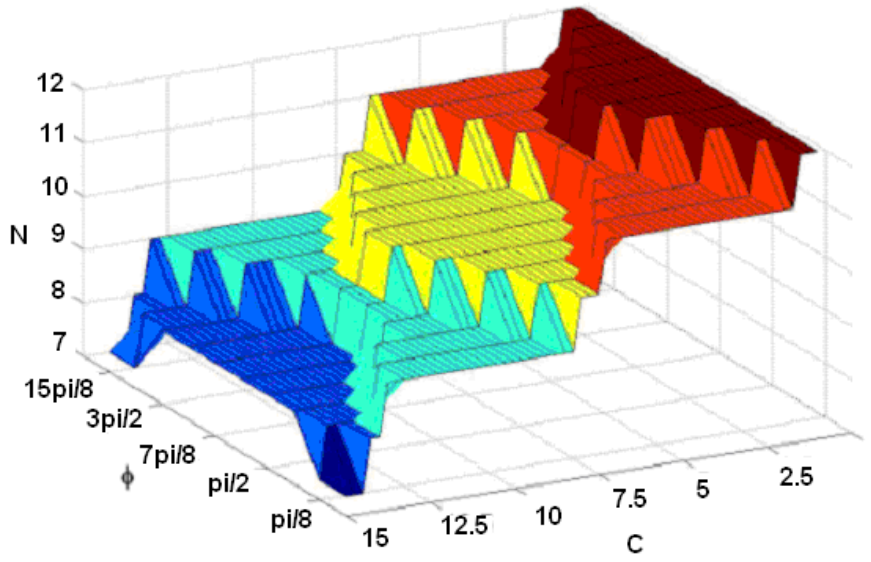

Figure 2.9. Number of fringes occurring for different sets of (C, Φ) values, for a target displacement amplitude of 6λ [Zabit 2010].

Therefore, the preferred C value for reliable experimental measurements of OFI is set close to 1, in the frontier between the weak and moderate feedback levels. For $C << 1$ (very weak regime) we have directional ambiguity combined with low SNR values. In the opposite case, for $C > 1$ we have hysteresis processes in the phase variation due to the existence of multiple solutions of the phase equation, leading to signal instability and fringe-loss, spoiling the accuracy of the measurements taken. Alternatives for large C values such as fringe-loss compensating algorithms have been proposed by Zabit et al [Zabit 2010], which can recover the first four fringes lost.

2.d. Signal processing

This thesis will be mainly focused on applications of OFI based on displacement measurement. In this section we will review with some detail the signal processing methods described in the literature related to displacement reconstruction out of the OOP signal variation.

In practical applications, the OOP signal can be affected by a number of unwanted and uncontrollable noise sources, which in several cases adds on to the faintness of the OOP signal to be detected. This leads to loss of signal quality and to severe decrease in the measurement accuracies. Thereby, signal processing is a key issue in experimental OFI, and will typically involve a pre-processing stage to reduce the effects of noise and to enhance the signal, followed by one of the different displacement reconstruction algorithms.

2.d.1. Pre-processing

The compactness and robustness of OFI makes it ideal for industrial metrology applications where, unfortunately, a number of parasitic phenomena are present and may introduce different types and levels of noise into the OOP of the LD. These unwanted phenomena include typically mechanical coupling, electromagnetic disturbances, and power and wavelength fluctuations due to temperature variations and inaccuracies in the LD driving source. Inevitably, these noise sources distort the OOP leading to decrease of SNR, yielding the detection of fringes more complex and consequently decreasing the accuracy of the measurement.

The types of noise which appear more frequently in OOP signals are some form of fast varying white-like noise (compared to the OOP fringe frequency, which is typically much slower) (Fig. 2.10(a)); sparkle-like noise as random spikes added onto the OOP (Fig. 2.10(b)); and multiplicative noise which appears in the shape of slow-time fluctuations of the amplitude envelope of OOP fringes (Fig. 2.10(c)) [Fan 2011][Wei 2007].

Several signal pre-processing solutions have been proposed from different fields in order to efficiently remove these noise sources and improve the SNR of the OOP. The most successful have been the classical moving-average filter [Zabit 2009] (essentially a low-pass filter), a Kaiser-based FIR filter combined with a median filter [Yu 2007], neural network interpolation [Wei 2007], and a filter based on the wavelet transform combined with a median filter [Sun 2011].

In many applications, the moving-average filter has been shown its ability to successfully eliminate the additive white-like noise from the OOP signal, so somehow it has become the gold standard in OOP signal pre-processing. However, due to its nature it can’t remove efficiently other types of noise. A very relevant issue to be considered in the pre-processing of the OOP signal is the fact that the application of the filter should not change the location of the fringes in the OOP signal, while at the same time it should keep the underlying waveform unchanged.

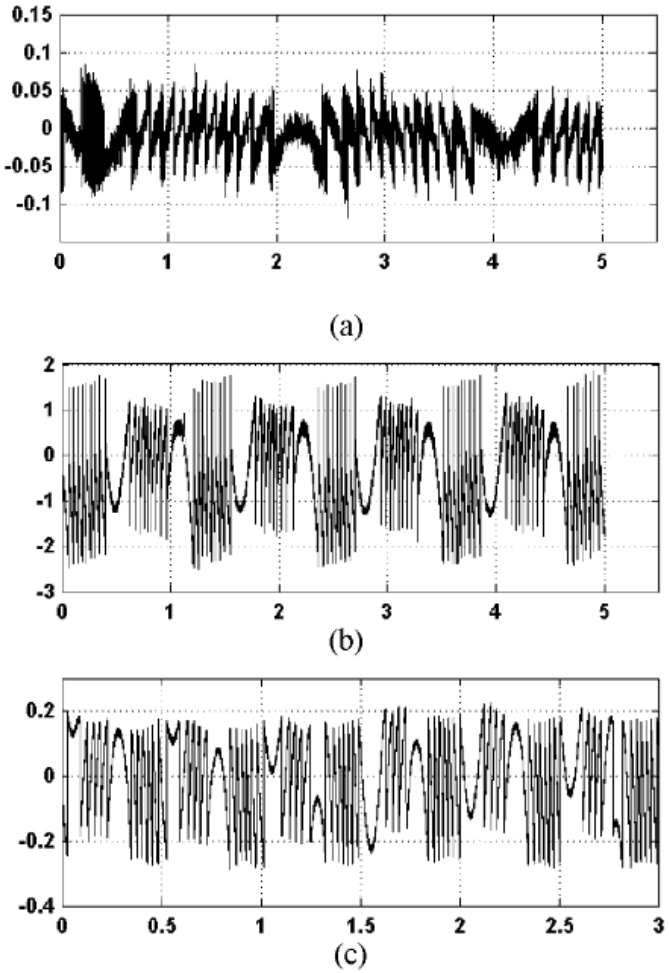

Figure 2.10. Experimental OOP (volts) versus acquisition time (seconds) with added noise. OOP is affected as dominant noise source with (a) white-like noise, (b) sparkle-like noise (c) multiplicative noise [Yu 2007].

For this reason, a Kaiser-based FIR filter combined with a median filter has been proposed, as the median filter eliminates the sparkle-like noise while the Kaiser window band-pass filter removes both the high frequency noise and the slow envelope fluctuations in the OOP signal [Yu 2007].

An interesting solution proposed for removing noise sources from OOP signals is neural network interpolation combined with a median filter. It efficiently removes several noise types, although the method is complicated to implement and rather time consuming. It is shown that applying this pre-processing algorithm with a particular reference displacement reconstruction algorithm (phase-unwrapping method described in subsection 2.d.2.3) could improve the measurement accuracy down to $\lambda/25$ for weak feedback and to $\lambda/20$ for moderate feedback [Wei 2007].

A wavelet transform based filter combined with a median filter, implemented on a field programmable gate array (FPGA), has also been designed for real time pre-processing purposes, and oriented to remove both high frequency and sparkle-like noise [Sun 2011].

2.d.2. Displacement reconstruction

In this section we will review three of the most used signal processing methods for displacement reconstruction described in the literature. The first one is the fringe-counting technique (FCM), which leads to a resolution of $\lambda/2$. The second method uses the existing relationship between OOP variations and displacement. It is quite accurate but needs previous calibration (in particular, C and LEF should be known prior to the measurement). The third technique is the phase-unwrapping method (PUM) which is a robust and reliable method leading stably to a resolution of $\lambda/16$. An important and interesting advantage of this method is the joint estimation of C, LEF, and the displacement, which has made of it the standard in displacement reconstruction algorithms for high resolution approaches.

2.d.2.1. FCM

The most simple, and still the fastest method used to retrieve displacement out of the OOP signal is the FCM method. It is thus the default option whenever real-time approaches are required. As described in section 2.a.1, the number of saw-tooth like fringes in the OOP is proportional to the target displacement, where each fringe may be interpreted as a displacement of the target equivalent to half the wavelength of the laser. Thereby, having N fringes for the amplitude of vibration of the target means we can estimate a displacement of $N\lambda/2$ with half-wavelength resolution. Counting these periodical fluctuations in OOP directly recovers target displacement. In addition, if the system is working under weak feedback conditions, the asymmetric shape of the fringes will enable to distinguish the sense of the displacement. Therefore, considering the proper sign of the half-wavelength steps in displacement (adding or subtracting) will result in displacement reconstruction without directional ambiguity [Donati 1995]. This method is simple and fast, and can be easily implemented for real time processing.

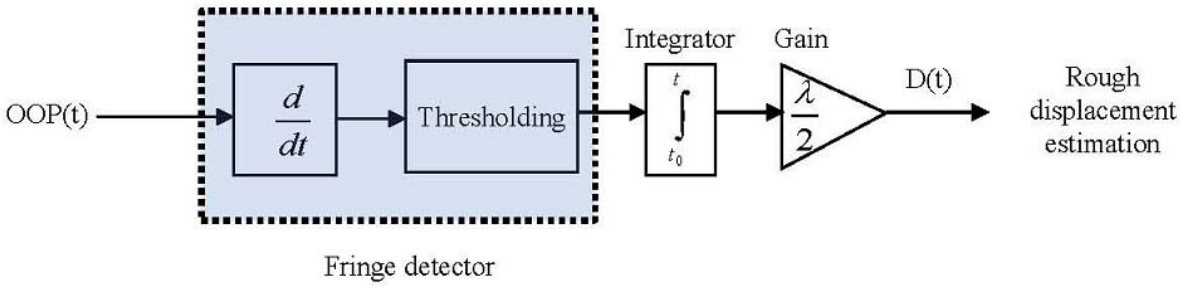

Figure 2.11. Signal processing scheme for FCM.

The processing scheme of the pre-processed OOP has been depicted in Fig. 2.11. It is obvious that the accuracy of FCM depends strongly on the fringe detection procedure. This is usually dealt with using time derivation of the OOP signal. The derivative procedure turns the OOP fringes into sharp peaks in the derivative signal, where positive peaks are related to downward fringes and negative peaks to upward ones, as shown in Fig. 2.12. Using an appropriate threshold value, the peaks can be detected with high

reliability. A normalization of the derivative signal may also be used to maximize the peaks and improve the result of the thresholding procedure value. Afterwards, an integrator algorithm adds up the associated fringe displacements taking into account the sense of the diaplacement, and once scaled by *λ/2*, a complete reconstruction of the displacement can be obtained.

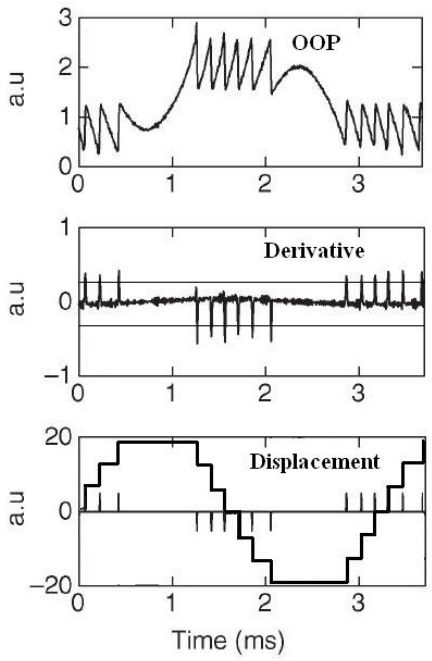

Figure 2.12. Displacement reconstruction steps in FCM.

2.d.2.2. Pre-calibration method

This method has been proposed by Merlo and Donati in 1997 [Merlo 1997] as an exact solution which directly reconstructs the displacement from the achieved OOP. The phase equation (equation (2.14)) and the power equation (equation (2.22)) are used to directly estimate the final displacement. *C* and LEF values, however, should be known prior to the measurements. After eliminating the DC component of the OOP and then normalizing to 1, an *F(t)* value may be obtained from equation (2.22) as

$$F(t) = \cos(2\pi\nu_c\tau_D) = \cos\left(2\pi\nu_c\frac{2D(t)}{c}\right) \tag{2.26}$$

By obtaining ν_c from equation (2.26) and replacing it in equation (2.14), two solutions for target displacement ($\Delta D(t)$) can be determined:

For $\left(\frac{dF(t)}{dt}\right)\left(\frac{dD(t)}{dt}\right) < 0$ we may find

$$\Delta D(t) = \frac{1}{2k}\left[\frac{C}{\sqrt{1+\alpha^2}}\left(\alpha F(t) + \sqrt{1-F^2(t)}\right) + \arccos(F(t)) + 2n\pi\right] \tag{2.27a}$$

While for $\left(\frac{dF(t)}{dt}\right)\left(\frac{dD(t)}{dt}\right) > 0$ we get

$$\Delta D(t) = \frac{1}{2k}\left[\frac{C}{\sqrt{1+\alpha^2}}\left(\alpha F(t) - \sqrt{1-F^2(t)}\right) - \arccos(F(t)) + 2(n+1)\pi\right] \qquad (2.27b)$$

where n is an integer. This technique is quite accurate but limited to $C < 1$, because the phase equation should have only one solution out of the assumption on OOP made in equation 2.26. A displacement resolution in the range of a few tens of nanometres for displacements of some microns has been reported [Merlo 1997].

2.d.2.3. PUM

PUM is now the reference method for displacement reconstruction when the LD is under moderate feedback and high resolution is required, without demanding real-time conditions. The most important advantage of the method is the joint estimation of displacement, C and LEF of the laser. However, it is neither a simple nor a fast algorithm to be implemented for displacement reconstruction. The complete flow diagram showing the signal processing operations involved in the method are illustrated in Fig. 2.13. The method is divided in two principal steps, the rough phase estimation and the joint estimation of displacement, C parameter and LEF value [Bes 2006].

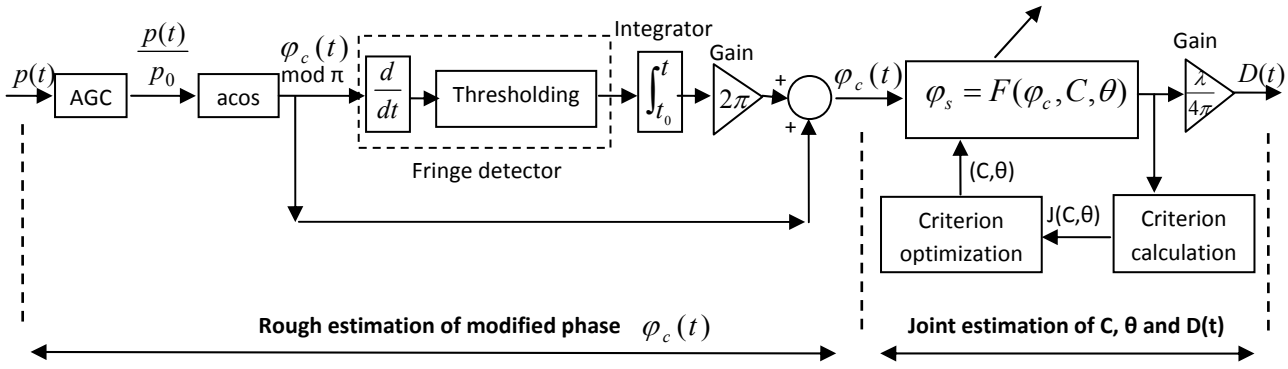

Figure 2.13. PUM signal processing scheme.

As already mentioned, the phase of the OOP signal may be expressed as

$$\varphi_c = 2\pi\nu_c\tau_D = 2\pi\nu_c\frac{2D}{c} = 4\pi\frac{D}{\lambda_c} \qquad (2.28)$$

$$\varphi_s = 2\pi\nu_s\tau_D = 2\pi\nu_s\frac{2D}{c} = 4\pi\frac{D}{\lambda_s} \qquad (2.29)$$

Where φ_c is the phase of the OOP of the LD under feedback, φ_s is the phase of the OOP of the LD in the free running state, and λ_c and λ_s are the associated wavelengths of the LD with and without feedback,

respectively. Combining equations (2.28) and (2.29) and the OOP equation (equation (2.22)), the phase value in the free running state (equation (2.14)) may be rewritten as

$$P = P_s\left(1 + m \cdot \cos(\varphi_c)\right) \tag{2.30}$$

$$\varphi_s = \varphi_c + C \cdot \sin(\varphi_c + \arctan(\alpha)) \tag{2.31}$$

Equation (2.31) indicates that the phase in the free running state (φ_s) can be found provided a correct estimation of φ_c, C and α is available. According to equation (2.29) this will lead to a displacement estimation of

$$D = \varphi_s \frac{\lambda_s}{4\pi} \tag{2.32}$$

Therefore, displacement reconstruction depends on the accurate estimation of the three mentioned parameters.

According to [Yu 2004] and [Petermann 1995], for $C > 1$, impulses or discontinuities in φ_c related to fringes in the OOP signal are due to phase jumps of 2π. Therefore, adding or subtracting 2π to the φ_c value obtained when a discontinuity is detected leads to rough reconstruction of the phase φ_c.

The process of rough reconstruction of the phase has been presented step by step in Fig. 2.14. This process starts with the elimination of the DC component of the OOP, which then is normalised to 1 (Fig. 2.14 (a)). This operation has been designated as automatic gain control (AGC) in the block diagram of Fig.2.13. After this processing, we should get the $F = \cos(\varphi_c)$ value, so recovery of φ_c modulus π (Φ_c) (Fig. 2.14 (b)) is obtained through

$$\Phi_c = \arccos(F) \tag{2.33}$$

To unwrap the obtained phase and get φ_c, a transition detector is used to find the positions of the transitions in the signal. As in FCM, the transition detector is based on the derivative of Φ_c (Fig. 2.14 (c)) followed by thresholding, in order to find the transition positions. Later, transitions are normalised to 1 (Fig. 2.14 (d)) and an integrator adds or subtracts 2π to the phase, depending on the sign of the discontinuity. At this step, we can roughly estimate the phase, and subsequently the displacement by multiplying the obtained phase by $\lambda_s/4\pi$.

This rough estimation is better than the one obtained using FCM, but it still may be improved using a second step [Zabit 2010b]. Figure 2.15 shows a comparison of typical results obtained using conventional FCM and the rough estimation method described here.

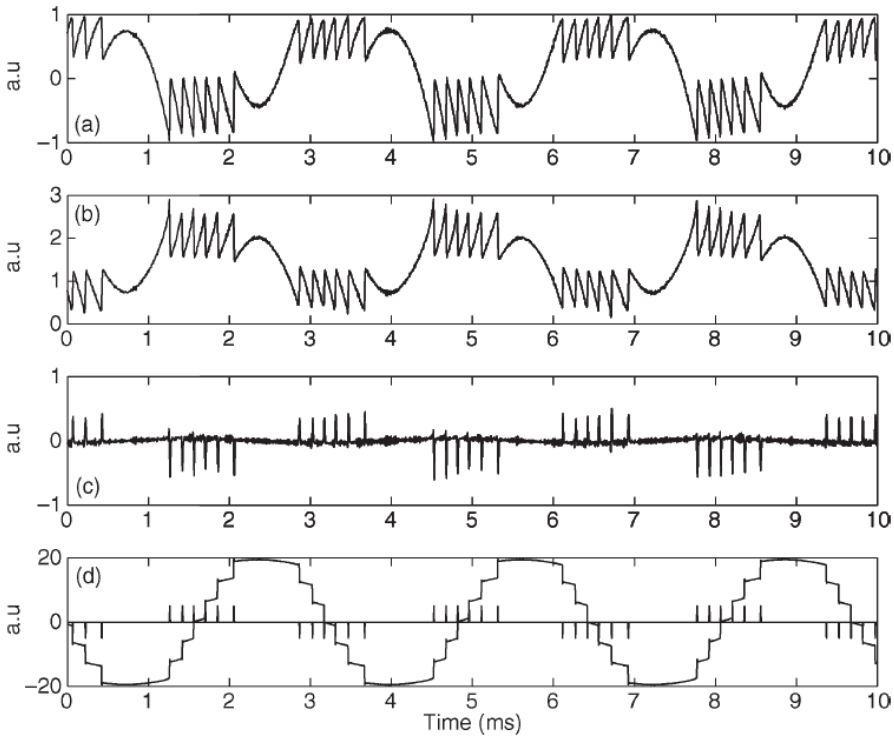

Figure 2.14. First step of PUM signal processing: rough reconstruction of the phase [Bes 2006]. (a) Normalised OOP (F(t)), (b) arccos(F(t)), (c) derivative of arcos(F(t)), (d) transitions and rough reconstruction of φ_c .

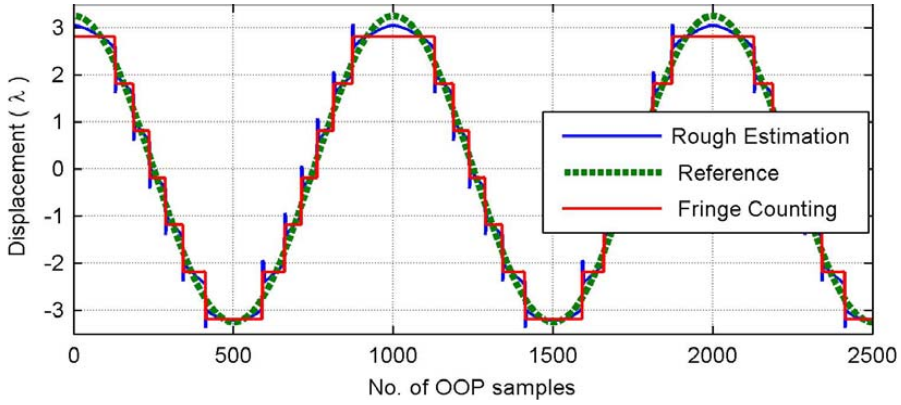

Figure 2.15. Simulations results comparing the FCM reconstruction and the rough PUM reconstruction [Zabit 2010b].

In the second step of the PUM technique the displacement, *C* and LEF are jointly estimated. The concept in the algorithm is assuming that discontinuities in displacement are far less frequent than discontinuities in the OOP or the phase. Considering the value of $\theta = \varphi_c(t=0) + arctan(\alpha)$ is constant, then equation (2.31) becomes

$$\varphi_s = \varphi_c + C \cdot \sin(\varphi_c + \theta) \qquad \text{(For t > 0)} \qquad (2.34)$$

Choosing a right set of (C,θ) values will result in minimized discontinuities of the phase φ_s. Thus, the procedure in the second step is to find the right set of (C,θ) values which leads to minimization of the discontinuities of phase φ_s.

Thereby, we could consider a criterion for the optimization process described as

$$J(C,\theta)=\sum_{n=1}^{N}\left[\left(\varphi_s(n)-\varphi_s(n-1)\right)\right]^2 \tag{2.35}$$

Where $\varphi_s(n)$ is the discrete form of the phase φ_s. In fact, the criterion $J(C,\theta)$ is evaluated in a temporal window containing N points for square of time derivation of phase φ_s. Thus, the optimal set of (C,θ) values minimizes $J(C,\theta)$, leading to the unwrapped phase φ_s and consequently to displacement estimation using equation (2.32). Figure 2.16 presents criterion $J(C,\theta)$ for experimental OOP data for different sets of (C,θ) values. The minimum point in the graph corresponds to the optimum set of (C,θ) for this experimental OOP.

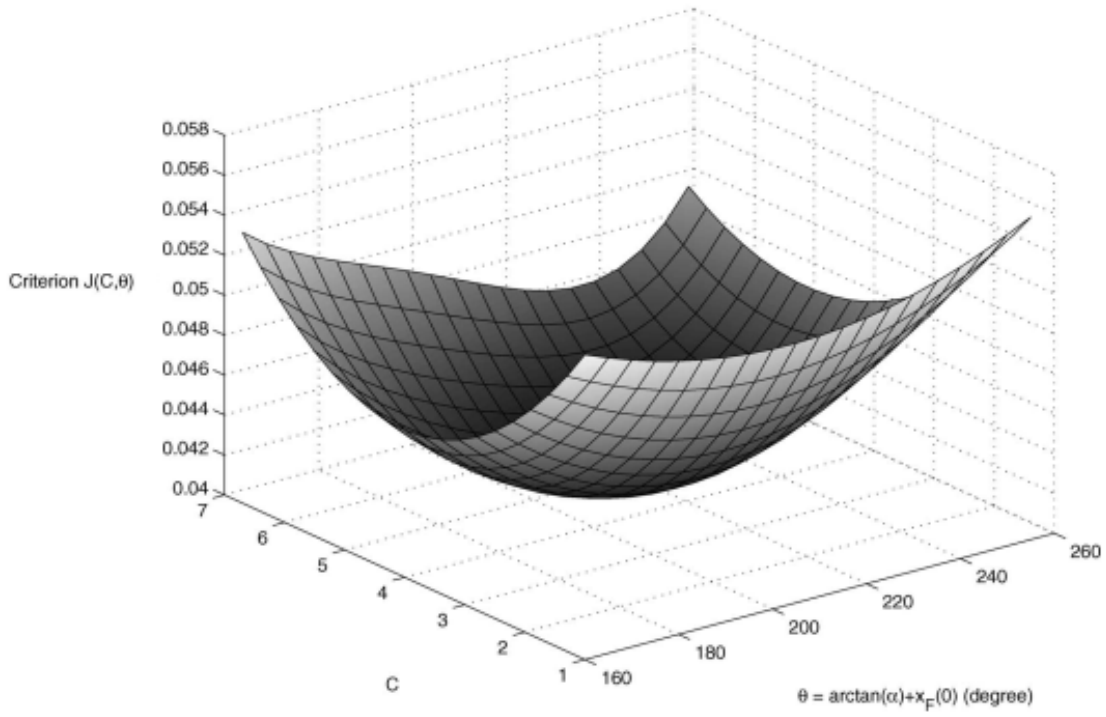

Figure 2.16. Criterion J(C,θ) for experimental OOP for different sets of (C,θ) [Bes 2006].

2.e. Speckle effects in OFI

Speckle is a very well-studied effect which occurs when coherent light is backreflected from, or transmitted through, a rough surface. The name comes from the speckled appearance which appears when

light is scattered forming a granular interference pattern (Fig. 2.17) due to the random phase superposition of the beams on the illuminated area at the observer's position. In fact, when the average roughness of the surface is comparable to the wavelength of the laser, the spatial coherence of the laser disappears and the speckle pattern can be understood as a random interference of beams resulting in a spotted texture.

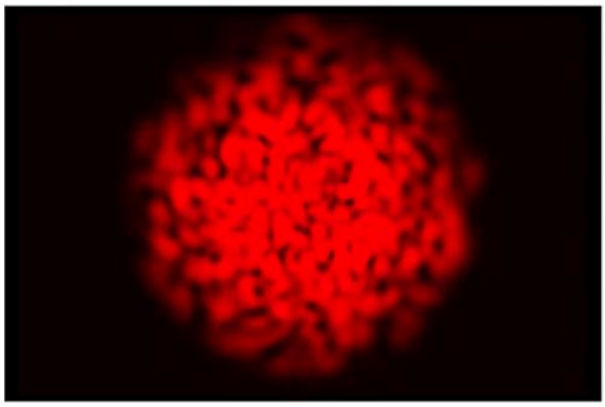

Figure 2.17. Granular interference pattern formed by speckle phenomenon.

In the case of OFI, the backreflected beams from the target re-enter the laser cavity and are mixed with the standing waves in the active laser medium. Diffusive surfaces are usually used as targets, as retro reflective targets usually yield too high feedback levels, so speckle effect may appear and affect the optical feedback interference pattern. For small displacements of the target (e.g. with amplitudes from a few microns to 0.1mm) there is no apparent speckle effect in the OOP of the LD, as the displacement is much smaller than typical speckle size [Donati 2004].

However, for larger displacements, going from a few millimeters to some centimeters or over, speckle effects are easily observed as an amplitude modulation of the OOP signal, where amplitude fading occurs frequently (due to dark "speckle grains"), and where in addition a speckle phase error of random origin is added to the signal. Figure 2.18 shows a typical experimental OOP obtained for a large target displacement, where amplitude modulation due to the speckle effect leads to OOP fading in some regions of the signal. Regions of the signal where the signal amplitude faded due to the speckle are usually referred to as blackout regions.

This amplitude effects make extremely complex, if not totally impossible, to properly detect the transitions in the OOP in the blackout regions due to the severe reduction of the SNR of the signal. This brings on important inaccuracies in displacement and velocity measurements. For instance, a velocity measurement error in the range of 3% over a wide velocity range (5.2mm/s – 479mm/s) due to speckle effect has been reported recently [Lu 2010], while speckle-related displacement measurement errors are in the range of 10% for large displacements [Donati 2004] prior to using any of the available speckle compensation techniques.

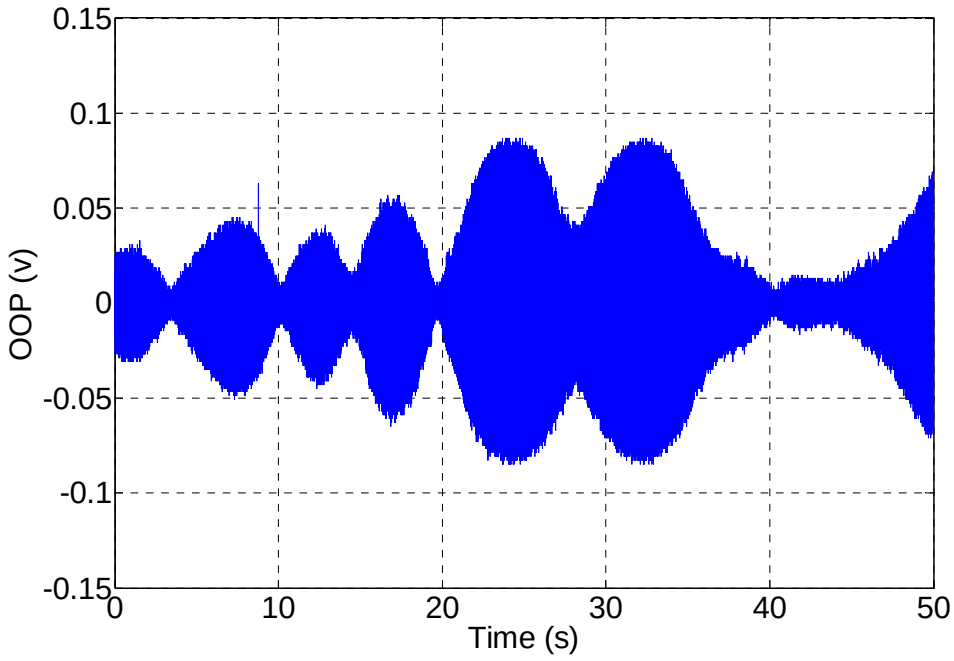

Figure 2.18. Experimental OOP achieved along a large target displacement.

The relationship which exists between the intensity distribution of the backscattered laser light and the target surface roughness has been extensively studied in the past decades [Fujii 1976]. Furthermore, relationship between the speckle-modulation in OFI and the surface profile of the target has been investigated as well [Huang 2008]. The practical problem posed is relevant as the OFI measurement principle inherently forms speckle patterns on rough targets.

Further than the average roughness of the target surface at the incidence point, some other parameters related to the geometry of the experimental setup such as beam spot size, laser distance to the target, and wavelength of the laser are known to affect the size of the speckle "grains" in OFI. The mean value of speckle sizes for the objective speckles which appear in free propagation of a diffused coherent light field can be obtained from [Dainty 1975]

$$OS_l = \lambda\left(\frac{d}{D}\right)^2 \quad , \quad OS_t = \lambda\left(\frac{d}{D}\right) \tag{2.36}$$

Where OS_l and OS_t are longitudinal and transversal objective speckle sizes, respectively, D is the laser spot diameter on the target, and d is the target distance from the laser.

In the case of subjective speckles, an optical element is located between the observer and the target as seen in Fig. 2.19. The speckles appearing on the LD side (which performs as the observer in OFI setups) are projected by the lens as virtual speckles on the target. The mean value of longitudinal and transversal sizes of these virtual speckles are given by [Donati 2004]

$$SS_l = \lambda(\frac{2l}{D_L})^2 \quad , \quad SS_t = \lambda(\frac{l}{D_L}) \tag{2.37}$$

Where SS_t and SS_l are transversal and longitudinal subjective speckle sizes respectively, l is the target distance from the lens and D_L is the lens diameter.

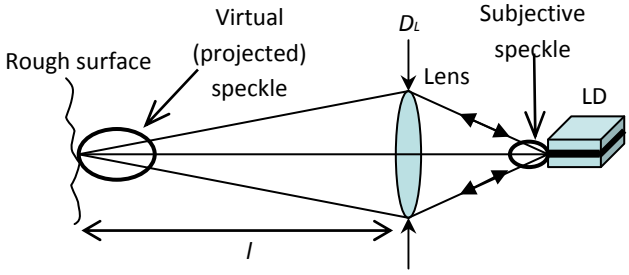

Figure 2.19. Schematic diagram for description of subjective speckle in OFI.

In a typical OFI setup usually a collimating lens is used to focus the laser beam on the moving target to monitor the longitudinal displacement of the target. Therefore, the generated speckles are subjective speckles apparent to the LD due to imaging of the coherent superposition of reflected beams from the target. Obviously, the OOP modulation frequency is related to the longitudinal sizes of the virtual speckles projected on the target side (SS_l).

Larger speckle sizes lead to lower modulation frequencies in the OOP amplitude, resulting in general in less severe amplitude fading effects. Thus, the combination of target distance, lens aperture and wavelength needs be optimized to obtain speckle sizes as large as possible within given experimental conditions. However, usually there are substantial limitations on the range of variation of such parameters. Just as an example, when the target surface is diffusive and the target distance becomes very large, not enough backscattered light returns to the laser cavity, leading to poor SNR in the OOP signal and to difficulties in the correct reconstruction of the displacement, complicated even more by the presence of speckle. If wavelength and distance are fixed, aperture is still a compromise, as lens diameter should be large enough to focus the entire laser beam coming out of the laser cavity, which is normally divergent, and to recover enough backscattered light from the target in order to produce relevant optical feedback interference. In fact, by optimization of the mentioned parameters, the modulation frequency due to speckle may be somehow reduced but almost never eliminated.

Further than amplitude modulation, random speckle phase error is also introduced in the signal. However, its effects are typically much less noticeable than those of amplitude fading, as speckle phase error corresponds to displacement inaccuracies in the order of λ for a travelling range of 50cm [Donati 2004]. When we cross longitudinally a speckle "grain" we may assume we have a phase error σ in the signal which equals to $\sigma = \lambda$ [Donati 2004] [Norgia 2001]. For a total target displacement of Z we have $N = Z/SS_l$ subjective speckles, whence introducing a phase error of

$$\sigma_Z = \lambda \frac{Z}{SS_l} = \frac{D_L{}^2 Z}{4l^2} \tag{2.38}$$

As an example, with a lens diameter of D_L = 4mm, a target displacement of 10cm at a distance of 1m from the lens, a phase error of 0.4μm is induced. It is a minor effect in displacement measurements but it may need to be taken into account in given high resolution situations.

To the best of our knowledge, only one technique has been implemented to overcome the problem of amplitude fading by speckle prior to this Thesis. It uses an in-plane piezoelectric positioning system to keep the amplitude of the signal at the maximum level by scanning the target [Norgia 2001]. In this bright speckle tracking technique (BST), the laser is moved transversally to look for the highest amplitude OOP available, avoiding signal fading. Figure 2.20 shows the experimental configuration for the BST solution. An accuracy of a few parts in 10^6 in a displacement range of 50cm has been reported using this approach.

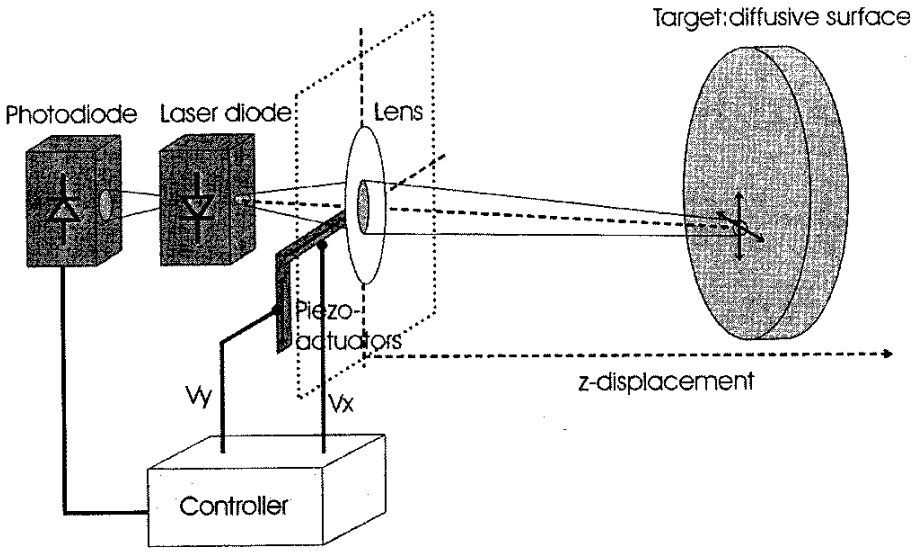

Figure 2.20. Experimental configuration for BST technique [Norgia 2001].

2.f. Conclusion

The theory of OFI, including the general overview of the physical phenomenon and a review of the typical applications presented in the literature has been presented in order to present the general overview of the technique. The two models used to describe the laser under feedback (the equivalent cavity model and the Lang-Kobayashi equations) have been introduced, and the effects of the different feedback level on the OOP and its measurement capabilities discussed. Furthermore, general review of the most used signal processing algorithms for displacement reconstruction, including the preprocessing stage, has been

presented. Finally, an overview of the effect of the speckle phenomena in OFI signals has been presented in this chapter.

This complete review has shown the advantages and basics of OFI-based sensors and sets the basic concept and tools used in the rest of this PhD work. However, it has shown the limitation of present setups regarding the effects of the feedback level and speckle noise in the signal. In the following chapters we will propose robust solutions for the general management of both problems.

3. Feedback Control in OFI

In this thesis it is proposed to improve the performance of the conventional OFI configuration by using a simple adaptive optical technique allowing automated control of the laser focusing. A variable-focus optical system will allow adjustable focusing of the beam, but also the optimization of the operating conditions to obtain the best possible OOP signal for ulterior processing. The adaptive element, inserted in front of the laser, needs to be small and robust, in accordance with the characteristics of all OFI setups, so conventional optical solutions such as zoom lenses are not an option due to its volume and cost. Thereby, in this chapter we will first study in section 3.a the possible solutions for a variable focus optical system and we will then propose a novel optical head for this purpose, including the design considerations and the fabrication of the final prototype.

In section 3.b, we will investigate the performance of the new optical head in a typical OFI configuration for the measurement of displacement, and its capability to control the feedback level of the laser diode. This part will cover a complete description of the available solutions for feedback control, the experimental configuration for the new approach, a simple measurement algorithm for controlling the feedback level without the need of operator, and the experimental results showing the effectiveness of the new optical head for feedback control.

Finally, in section 3.c, we will propose a novel measurement technique (which we named the Differential Optical Feedback Interferometry (DOFI) technique) for high precision demands in which the potential application of feedback control in the technique is presented. A last section will sum up the conclusions of this chapter.

The contents of this chapter have given rise to a number of contributions. We would specially mention a high-impact journal paper two conference papers [Atashkhooei 2011a] [Atashkhooei 2011b] related to the optical head design and the adaptive control of the feedback level in OFI. The work regarding the DOFI solution succeeded to be published as a PCT patent [Royo 2010], a conference paper [Azcona 2013a] and a journal paper currently under review [Azcona 2013b], partly within a specific PhD dedicated to DOFI currently under development.

3.a. Adaptive optical head (AOH)

To develop adaptive OFI solutions we need an adaptive optical element. This adaptive element will be used to actively control the focal length of the system, so the spot size of the laser beam on the target may be modified at will to find the best performance for the considered setup. In addition, we intend to preserve as much as possible the compactness and robustness characteristic of OFI setups, which stand out as one of their more relevant features. Among the different types of variable-focus lenses which have

been recently proposed for auto-focus and zoom applications, miniature lenses which have been used for cell phones and webcams are especially convenient to the setup due to their small diameter and physical characteristics.

Both lenses using nematic liquid crystals and liquid lenses based on the electrowetting effect have been proposed for a number of applications in industrial and commercial areas, such as in mobile phone cameras, eyeglasses, machine vision applications, and auto beam steering. Other liquid lens approaches, based on different physical property changes (i.e. pressure or elasticity) [Ren 2007] had not succeeded in getting to the market at the moment when this work was done. However, at present, pressure-controlled liquid lenses changing focus using a piezoelectric actuator start to be commercially available [Optotune].

Different approaches for liquid crystal lenses have been proposed such as polymer stabilized [Fan 2003], modal controlled [Naumov 1998] and surface relief profile [Ren 2006] lenses. Among these approaches, the surface relief one is the most attractive as it is free from light scattering and has a uniform response time in the order of 1s. The response time of the liquid crystal molecules is, in general, their main drawback and prevents from their use in high frequency applications, but they are commercially available since a few years ago [OkoTech].

Alternatively, electrically tunable focus lenses based on the electrowetting effect have comparable diameters, are more robust, and are particularly attractive for our application because of their faster response time (80ms), wider focal length interval with both negative and positive powers (-12 to +18 Dioptres), and independence of the polarization of the incoming light [Berge 2000]. They are commercially available from at least two providers, to the best of our knowledge, including Varioptic [Varioptic] and Phillips [Philips] [Hendriks 2005]. They are currently mass-produced for mobile phone camera applications, so they are widely available and relatively cheap. Their small diameter does not pose a problem in our application, as the beam diameter we need to use is also much reduced.

In the next subsection we will briefly deal with the working principle and the typical features of electrowetting-based lenses, which will be used as adaptive elements in our OFI setup. Later, subsection 3.a.2 will describe the design of the optical head taking into account the laser beam characteristics and the desired optical focus range. In the last subsection 3.a.3, the final prototype which was constructed and which is going to be used in this Thesis will be presented.

3.a.1. Electrowetting-based liquid lenses

Electrowetting-based liquid lenses are formed by a mixture of two immiscible liquids with different refractive indices, like oil and water, which form a clear interface layer. By changing the curvature of the intermediate layer the optical power of the lens can be modified and controlled. Different technologies have been proposed for changing the curvature of the surface of the lens or the interface, such as using electromagnetic [Lee 2007] or piezoelectric stack actuators [Oku 2006], to apply some pressure on the

liquid volume for changing the curvature of the surface, electrochemical activation [Lopez 2005], other mechanical means such as changing the aperture size of the lens by rotation of impellers using a lever actuator [Ren 2005] and, finally, the electrowetting effect [Berge 2000]. Among them, electrowetting has proven to be the most successful at the time of doing the experiments, because of higher image quality, speed and reversibility, but also because of the capability of fabricating cheap and electrically controllable lenses and, thus, because of its commercial availability [Varioptic].

As a simple description of the electrowetting phenomenon, when a voltage is applied between a metallic electrode covered by a dielectric layer and a droplet of conductive electrolyte, an observable reduction of the contact angle of the liquid and the solid surface occurs [Mugele 2005]. First works on electrowetting were reported long time ago by Lippmann [Lippmann 1875] and later by Froumkin [Froumkin 1936]. Lippmann showed that adding electrostatic charges on an electrode can modify the capillary forces present at the interface and thus can be used to change the curvature of the liquid droplet sitting on the electrode.

As shown in Fig. 3.1, electrostatic charges induced by an applied voltage between the electrode and the electrolyte are not uniformly distributed. In fact, charges tend to accumulate at the edge of the electrolyte due to the electrostatic edge effect. So, the field at the corners tends to pull the electrolyte droplet down onto the electrode, to increase the contact area of electrolyte-electrode interface and so to decrease the contact angle (θ) [Quilliet 2001].

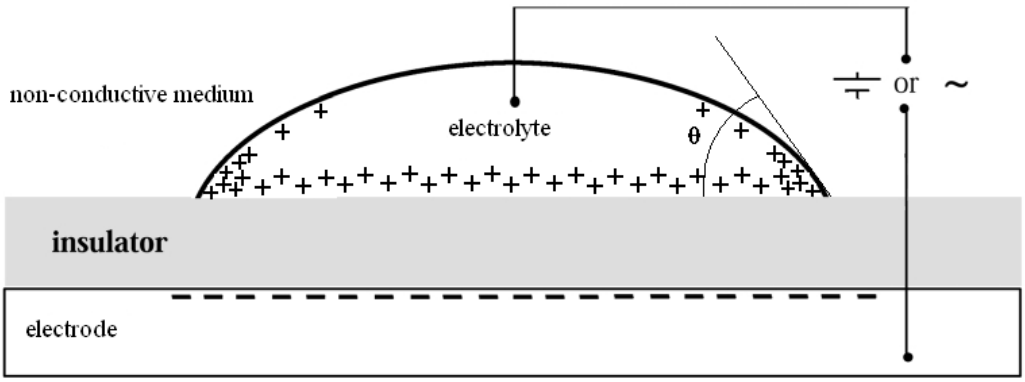

Figure 3.1. Schematic representation of the principle of electrowetting [Quilliet 2001]

The Lippmann equation describes the contact angle and is given by

$$\cos(\theta) = \cos(\theta_0) + \left(\frac{\varepsilon\varepsilon_0}{2\gamma d}\right)V^2 \qquad (3.1)$$

Where θ_0 is the contact angle at zero voltage, ε is the relative dielectric constant of the insulator, γ is the surface energy between the electrolyte and the surrounding medium (which in the case of the liquid

medium is the liquid-liquid interfacial tension), d is the insulator layer thickness and V is the applied voltage. Therefore, equation (3.1) quantifies how the contact angle, and subsequently the radius of curvature of the droplet, is modified when the voltage changes.

In commercial liquid lenses, two immiscible liquids with different refractive indices (a water solution as an electrolyte and an oil-like solution as a non-conductive liquid) are enclosed within a closed cell with two transparent windows. To avoid any orientation to gravity, the same density for both liquids is chosen. To stabilize the optical axis, a particular geometrical design for the closed cell has been performed as shown in Fig. 3.2 [Berge 2005].

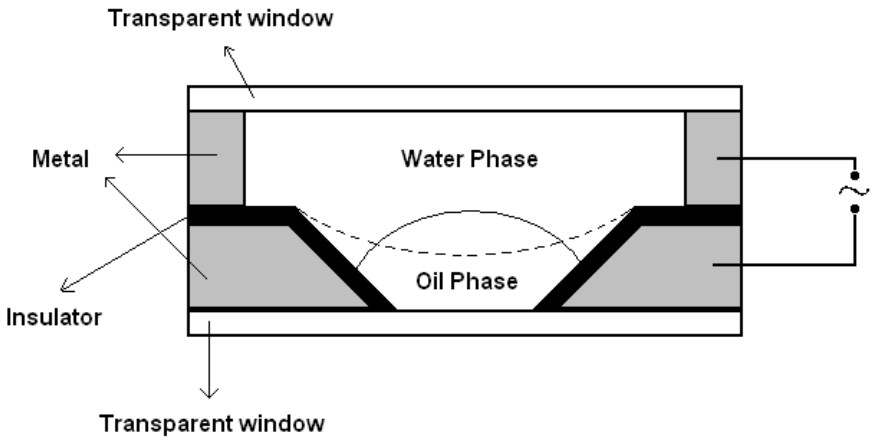

Figure 3.2. Schematic diagram of a commercial electrowetting-based liquid lens [Berge 2005]

Figure 3.3 shows typical commercial liquid lens designs from Varioptic, with an external diameter of 7.8mm. The change of focal length and aberrations of the lens by modifying the voltage have been characterized extensively.

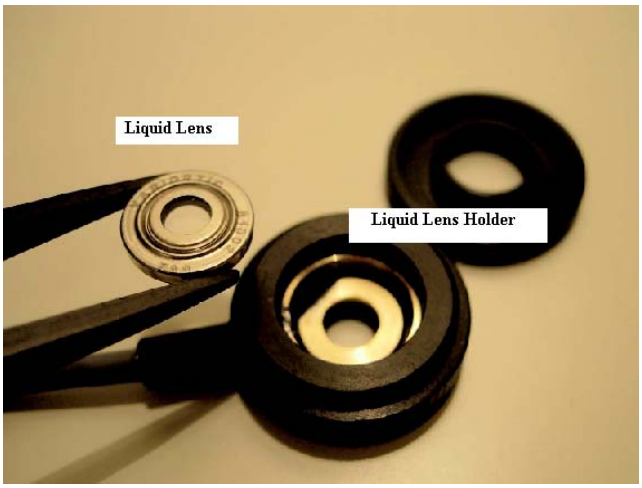

Figure 3.3. A commercial Varioptic Liquid Lens and its holder [Varioptic]

Figure 3.4 shows typical optical power and root mean square wavefront error in terms of applied voltage out of extensive wavefront error analysis using a Shack-Hartmann wavefront sensor on electrowetting-based lenses [Berge 2006]. In our approach area imaging is not involved, and aberrations will play a very minor role. Their dynamic response, however, will be very relevant in our system, and has also been analysed in depth [Gabay 2002]. Figure 3.5 shows the radius of curvature of the wavefront against time when applying a step voltage of about 110V. The change in radius of curvature corresponds to a change of 26 dioptres.

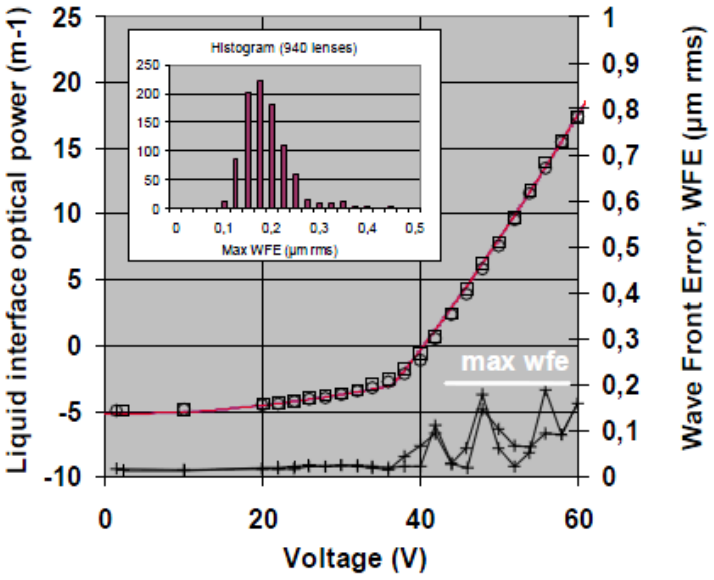

Figure 3.4. Optical power and RMS of wave front error for a Varioptic lens as a function of voltage [Berge 2006]. The insert shows the frequency of the maximum wave front error (WFE) of 940 lenses in µm.

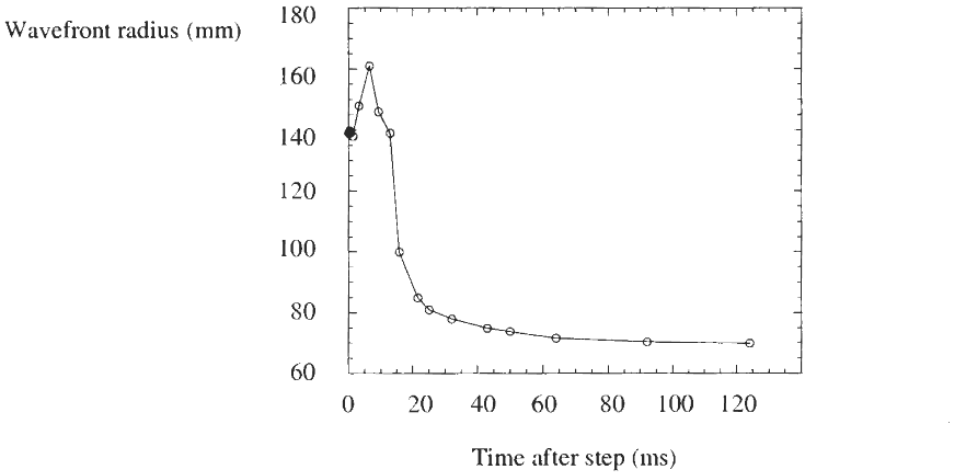

Figure 3.5. Wavefront radius as a function of time for a 26 dioptre change corresponding to 110V step [Gabay 2002]

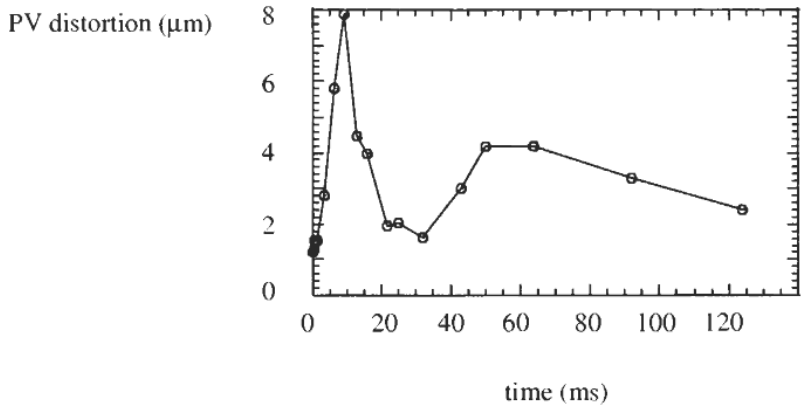

Figure 3.6. Peak to Valley (PV) of the distortion of the wavefront after the lens as a function of time for 26 dioptre changes corresponding to 110v [Gabay 2002]

Figure 3.6 depicts wavefront distortion for the same voltage as a function of time, showing relaxation time after applying a step voltage was in the order of 10ms and the time required for full wavefront quality recovery was between 40 and 50ms. Electrowetting-based liquid lenses have been recently proposed for a wide range of technological applications such as display technology [Hayes 2003] [Beni 1982], adjustable lens and micro-lens systems [Krogmann 2005] [Hendrinks 2005], or MEMS devices [Krogmann 2006]. They are fast, compact, robust and cheap in mass production, so they make a very interesting approach for an adaptive OFI configuration. They are the best option among the existent liquid lens technologies. Their main drawback in general-purpose applications, which is their limitation regarding effective diameter which cannot go beyond a few mm, is not relevant in our application where only focusing a laser beam is required.

3.a.2. Design of the adaptive optical head

The conventional optical system used in OFI setups consists of a single biconvex lens, sometimes with an aspherical surface, with a manual mechanical adjustment. This lens is displaced in a threaded mount at the proper distance from the front facet of the laser so focusing the beam at the target distance is attained and the adequate level of backscattered radiation is fed into the laser cavity. As mentioned before, our intention is to use an adaptive voltage programmable liquid lens (LL) in the optical path of the laser to modify the focal length of the system electrically, and implement adaptive adjustment capabilities. The adaptive LL used in the rest of this thesis is an electrowetting-based ARCTIC 416SL-V3 LL [Varioptic].

The optical power behaviour and the wavefront error characteristics of this lens have been introduced in the previous Subsection. As seen in Fig. 3.7 [Varioptic] by changing the applied voltage from a few volts to 60V, the optical power can be modified from -12 Dioptres to +18.75 Dioptres, while the root mean square (RMS) of the wavefront error is nominally kept below 0.05µm. Interestingly, the focal length variation is quite linear between a threshold and a saturation voltage.

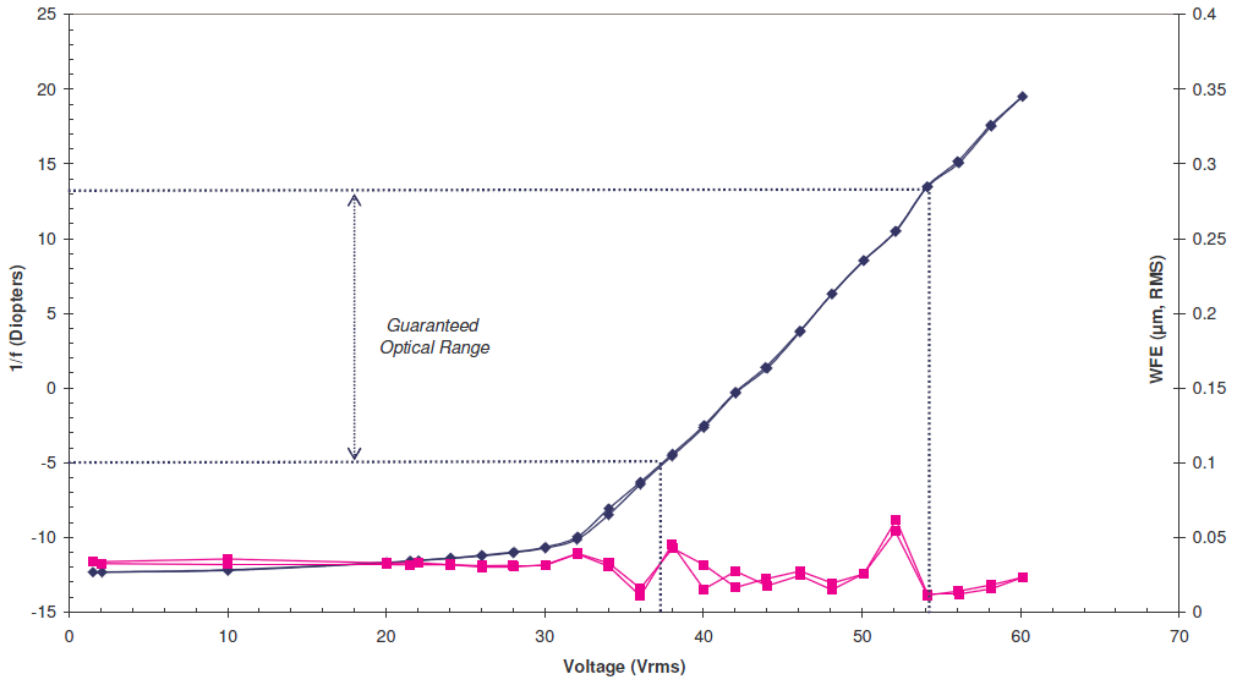

Figure 3.7. Measured characteristics of the electrowetting-based ARCTIC 416SL V3 LL [Varioptic].

Unfortunately, direct replacement of the conventional fixed focal lens by the LL does not work. A FPLD, like the one we are using in all experiments is highly divergent (with typical beam divergence being 23º the full width at half maximum (FWHM) for Hitachi HL7851G LD). In fact, divergence depending on the direction of emission may be observed, being larger in the direction of the active medium layer, identified as "perpendicular" in Fig. 3.8.

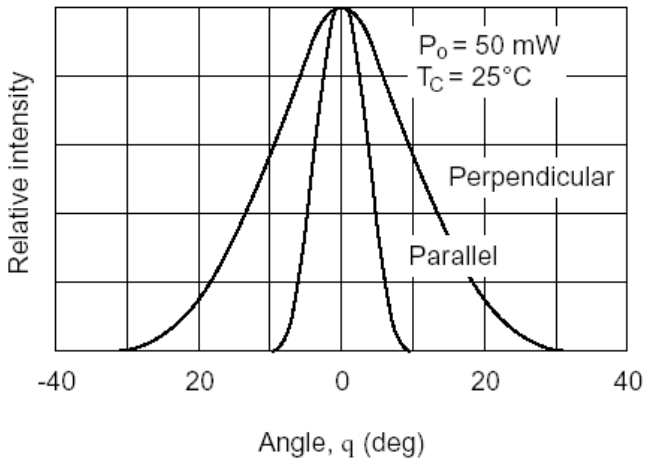

Figure 3.8. Beam characteristics (at far field) of a typical Hitachi HL7851G LD [Thorlabs].

Fig. 3.9 shows the schematic geometrical diagram of the laser and a lens oriented to collimate the whole power of the laser within the lens pupil, with angle θ considered as the maximum beam divergence of the

laser. Therefore, the maximum distance of the lens to the laser without power loss due to vignetting is given by

$$a_{\max} = \frac{D}{2\tan\theta} \tag{3.2}$$

Where D is the lens aperture and θ is the half angle of the laser beam.

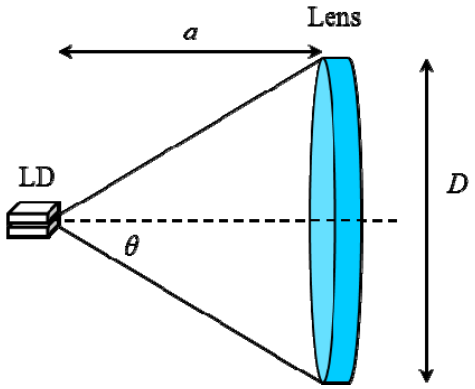

Figure 3.9. Geometrical diagram of the laser diode and lens for the collimation of the whole laser power.

To avoid virtual image formation and beam divergence after the lens, then, the focal length of the lens should be equal or smaller than a_{max} value. Considering that the laser diode used is a Hitachi HL7851G LD, with maximum beam divergence of 23º in FWHM, and considering that the commercial LL aperture is limited to around 2.7mm, for collimating the whole laser beam within the LL pupil the LL should be placed, as a maximum, 3.18mm away from the laser front facet. However, the minimum focal length available for the LL is just 5.3cm, so using just a LL for focusing is unfeasible. On the other hand, if a LL with an aperture of 2.7mm is placed at 5cm from the laser, a large amount of light will miss the aperture due to beam divergence. Therefore, direct replacement of the fixed focal length lens with a LL is not a correct approach for large range focusing.

Instead, the solution will be to use a combination of two lenses. The first one will be a fixed focal lens, which will have essentially a collimating role, while the second one (the LL) will be used for focusing.

The goal of the design stage is thus to design a combination of two lenses, one of them being the LL, which enables focusing the image of the laser diode aperture on the longest possible range of distances.

Let's consider the general set up shown in Fig. 3.10 for the proposed optical system. Under paraxial optics conditions (our case due to the small aperture involved), the position of the image formed by the first lens is given by [Hecht 2002]

$$\frac{1}{p_1} + \frac{1}{q_1} = \frac{1}{f_1} \Rightarrow q_1 = \frac{p_1 f_1}{p_1 - f_1} \tag{3.3}$$

Where p_1 is the position of the object, q_1 is the position of the image from the first lens and f_1 is the focal length of the collimating lens.

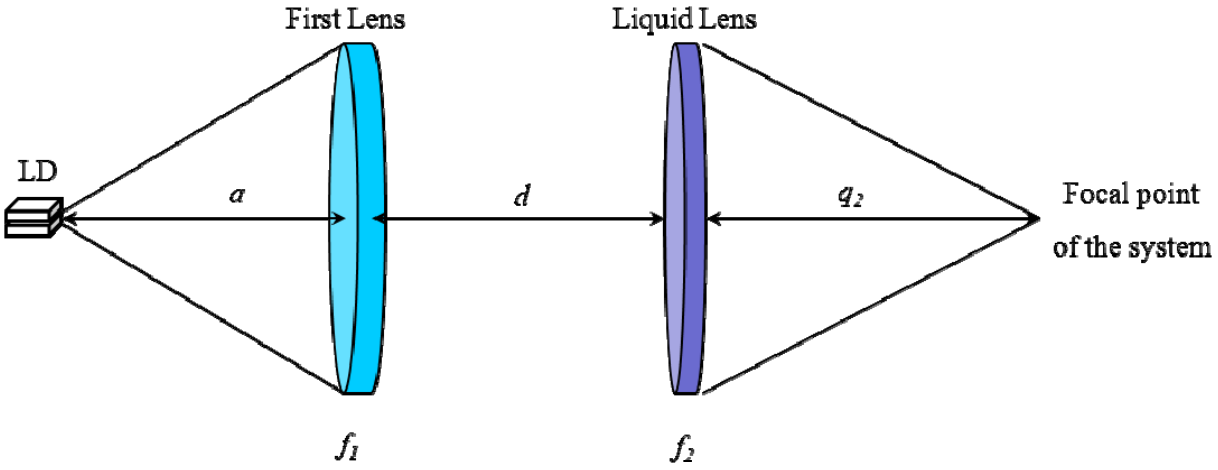

Figure 3.10. General setup for the combination of two lenses.

The image formed by the first lens becomes then an object for the second lens. The position of the object for the second lens is $p_2 = d - q_1$, where d is the distance between the two lenses. Thus, the final image distance is given by

$$\frac{1}{p_2}+\frac{1}{q_2}=\frac{1}{f_2}\Rightarrow q_2=\frac{p_2 f_2}{p_2-f_2}\Rightarrow q_2=\frac{(d-q_1)f_2}{d-q_1-f_2} \tag{3.4}$$

Where q_2 is the image distance from the second lens and f_2 is the focal length of the second lens (LL), which is variable. Obviously, from equations (3.3) and (3.4), the final position of the image depends on parameters d, f_1, p_1 and f_2. Hence, the idea is to select a proper combination of the values of d, f_1 and p_1 to cover the largest possible range of final image distances using the available range of LL focal lengths (f_2).

As a first step, the diameter of the first lens should be considered. We need to fix an aperture for the first lens that avoids light losses in the second lens aperture, where the aperture is fixed. Since the distance d should be short enough to have a compact and robust optical setup, the distance must be of a few millimetres. As an example, a simulation result using ZEMAX (a common optical design software) (Fig.3.11) shows that for the LL aperture of 2.7mm and d=5mm, the minimum aperture of the first lens has to be 5mm to avoid laser power losses in the entrance pupil of the LL.

Simulations performed in ZEMAX showed that d was not a critical parameter, in difference to a, the distance from the front facet of the diode to the first lens. By fixing the lens aperture at a reasonable value of 5mm from equation (3.2), we recall that the value of focal length should be smaller than 5.89mm. Moreover, it is preferred not to use large numerical aperture lenses because of the aperture aberrations involved.

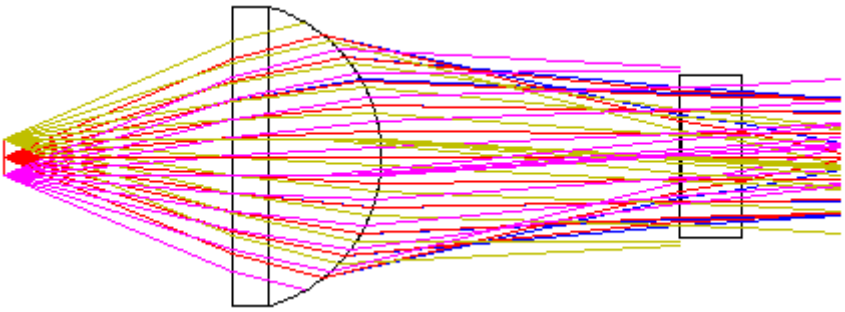

Figure 3.11. Simulation result by ZEMAX. for f_1 = 5mm, p_1 =5.1mm, D = 5mm, d = 5mm, LL diameter = 2.7mm.

As a reasonable value available commercially the focal length is set equal to the lens aperture (f_1 = 5mm). The optical power of the available LL ranges between -12 to +18.75 dioptres [Varioptic], so its focal length can be greater than 53mm (f_2 > 53mm) or smaller than -83mm (f_2 < -83mm).

By using the focal length values obtained and equations (3.3) and (3.4), the image distance can be achieved in terms of the object position (p_1) and the distance between the lenses (d).

Figure 3.12 shows the 3D graph of image distance in terms of focal length of the LL and the distance d between the lenses.

In this simulation, f_1 = 5mm, p_1 = 5.1mm and the negative optical powers of the LL is used. For positive values of focal length in the LL, the changes in image distance present a small range of variation which is not desirable, so the range of variation will be concentrated in negative values of the focal length of the liquid lens for our purposes.

As an example, Fig. 3.13 shows the range of possible positions of the final image for a fixed distance of the lenses (d = 5mm). The graph shows desirable image distance variations at negative focal length values of the LL. The image can be moved from a few millimetres to couple of meters for the available range of focal length values.

It is obvious that the number of attainable image positions depends directly on the number of possible values accepted for the focal length of the LL.

Table 3.1 shows measured typical values of radius of curvature (R) and optical power of the LL ($1/f$), versus the applied voltage. This table does not present the minimum possible steps of the LL power change. However, in digital control of the LL the minimum voltage step available to modify the focal length of the LL is set to 0.1V, so for a voltage range from 30V to 44V, which corresponds to the negative power of the LL, we have 140 individual values for setting the image position.

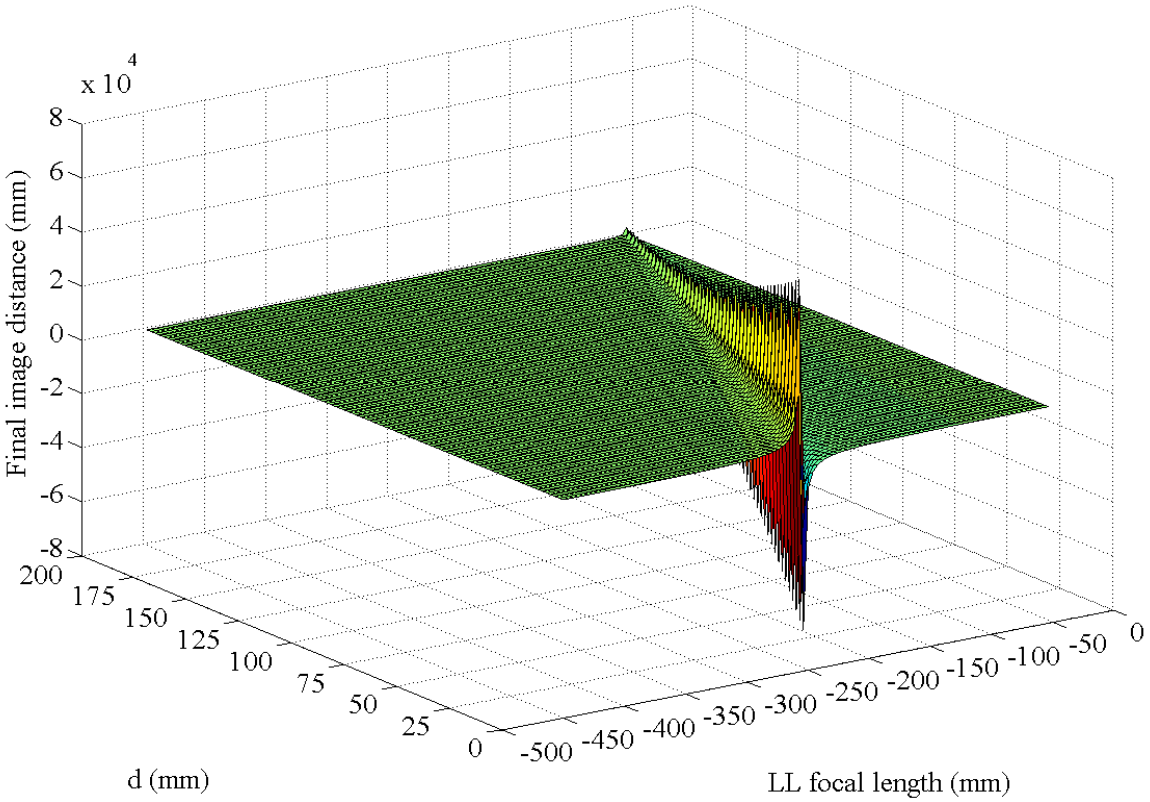

Figure 3.12. Variation of image distance versus focal length of LL and *d*, the distance between the LL and the first lens. First lens set at p_1=5.1mm, f_1=5mm.

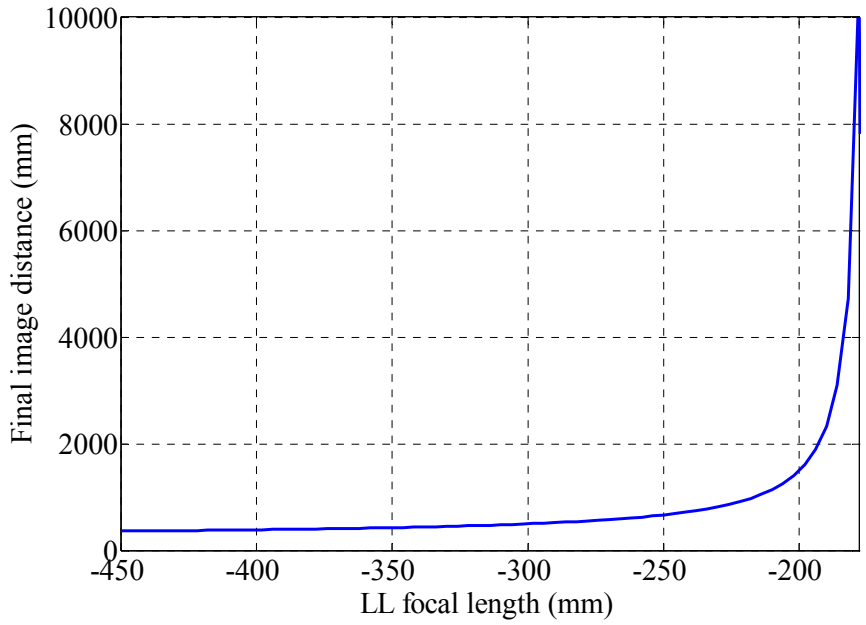

Figure 3.13.Variation of image distance versus the LL focal length at fixed *d value* (f_1=5mm, p_1=5.1mm, *d*=5mm), which is the configuration used in the experimental setup.

Table 3.1. Typical values of the optical interface versus voltage for the ARCTIC 416SL-V3 LL [Varioptic] .

Voltage (V)	R (mm)	1/f (Dioptries)
0 to 30	-7.23	-12.00
31	-7.33	-11.84
32	-7.89	-11.00
33	-8.56	-10.15
34	-9.36	-9.27
35	-10.36	-8.38
36	-11.62	-7.47
37	-13.26	-6.55
38	-15.48	-5.61
39	-18.67	-4.65
40	-23.62	-3.68
41	-32.32	-2.69
42	-51.63	-1.68
43	-131.25	-0.66
44	232.47	0.37
45	61.01	1.42
46	34.91	2.49
47	24.35	3.57
48	18.64	4.66
49	15.07	5.76
50	12.62	6.88
51	10.84	8.01
52	9.48	9.16
53	8.42	10.32
54	7.56	11.49
55	6.85	12.67
56	6.26	13.86
57	5.76	15.07
58	5.33	16.28
59	4.96	17.51
60	4.63	18.75

3.a.3. Final prototype

The schematic diagram of the final prototype of the adaptive optical head (AOH) designed is presented in Fig. 3.14. The collimating lens and the LL have been mounted in a movable tube which is connected to a fixed tube holding the laser diode, which is threaded onto the metallic heat sink used for cooling the laser. This way, the position of the collimating lens can be adjusted relative to the laser bringing it to the predetermined position if required.

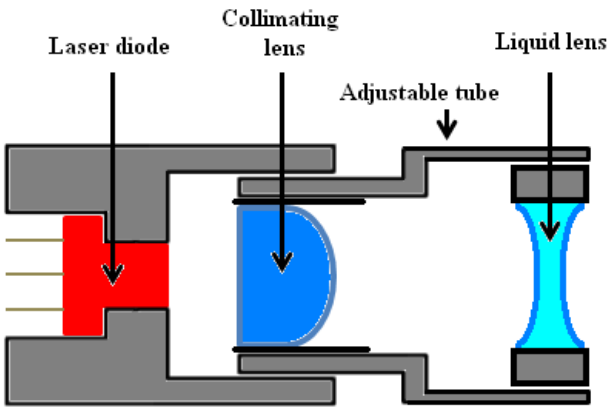

Figure 3.14. Schematic diagram of the designed AOH including the fixed tube holding the laser diode and the adjustable tube containing collimating lens and the liquid lens.

The p_1=5.1mm distance in the design condition is identified by a mark on the adjustable tube. The adjustment was left as an option to optimize the experimental performance of the system as p_1 was a critical value. Thereby, after properly fixing the position of the collimating lens, a large focusing range of the AOH from a few millimetres to a couple of meters is available using the focus range of the LL.

As mentioned, in the final prototype, the distance between the collimating lens and the LL was set to d=5cm. The collimating lens selected was finally an aspheric lens commercially available from Thorlabs with a focal length of 5mm, diameter of 6.48mm and clear aperture D=5mm, designed for a wavelength of 780nm, to help to remove the small spherical aberration present and enable the beam image to be diffraction limited. The LL is the mentioned ARCTIC 416SL V3 LL from Varioptic.

Figure 3.15 illustrates the final experimental prototype of the AOH mounted on the laser tube holding the laser diode and connected to the laser feeding circuit. As seen in the figure, the LL is connected to its driver so manual control of the LL voltage is enabled to modify the focal length of the LL. However, the LL controller can also be connected and controlled using a computer via a USB connection, a configuration which will be used later on when considering real-time speckle compensation using VC++ software.

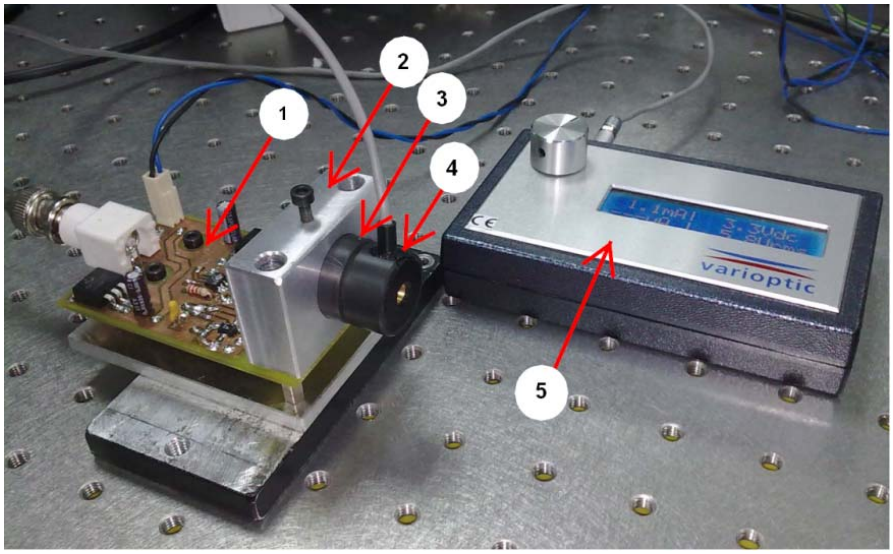

Figure 3.15. Experimental configuration of the AOH; (1) Electronic signal acquisition board, (2) Metallic heat sink containing LD package, (3) tube holding the fixed focal length lens and the LL, (4) liquid lens, (5) liquid lens manual controller.

3.b. Adaptive control of the feedback level

In this section, the AOH will be used in order to control the feedback level and to improve the SNR of the OOP signal. To our knowledge, the only solution covered in the literature to change the feedback level involves a variable optical attenuator (e.g. a liquid crystal attenuator) in the external cavity [Donati 1996]

[Norgia 2003], as shown in Fig. 3.16. The variable attenuator operates as an automatic gain control system to adjust the feedback power preventing the signal from becoming chaotic. This means it is only suitable for reducing the feedback level, not for increasing it. In addition, the effectiveness of using an attenuator for feedback control has not been characterized quantitatively. It is only useful to avoid excessive power feedback in the cavity and thus avoiding potential fringe loss due to hysteresis, by reducing the coupling coefficient.

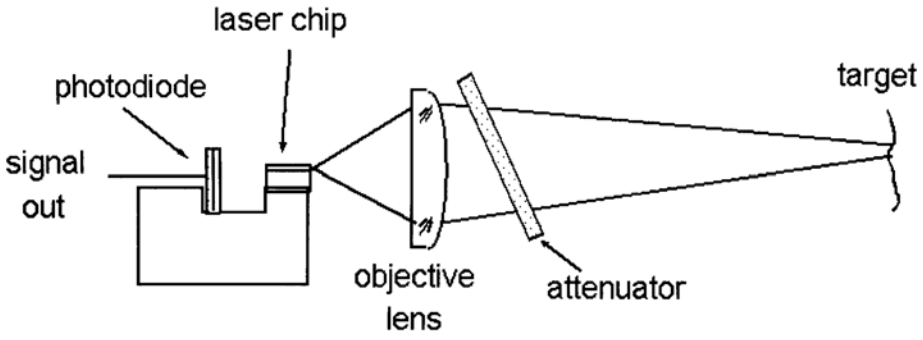

Figure 3.16. Basic configuration of OFI with an attenuator [Norgia 2003]

Our approach is using the new AOH designed for changing and controlling the feedback level of the laser, by focusing or defocusing the beam on the target, modifying the size of the spot of the beam on the target. In our approach, both excessive feedback and poor feedback conditions can be managed by simply modifying the spot size on the target, which changes the amount of light which gets back in the laser cavity. We will first present the experimental configuration for feedback control using the new optical head. Then, a simple control algorithm will be introduced for controlling the feedback level and keeping it in a given regime. At the end of this section, experimental results for feedback control will be demonstrated. Results will validate feedback control using the AOH and show the capability of the new head for keeping the laser in a desired regime for a long range of target distances.

3.b.1. Experimental configuration

Figure 3.17 presents the experimental setup diagram of OFI with the AOH configuration embedded. As presented in subsection 3.a.3, the AOH enables to focus the beam in a long distance range going from a few millimeters to some meters.

The equipment arrangement for the experimental setup has been illustrated in Fig. 3.18. In the setup the LD is a Hitachi HL7851G single mode LD with 50mW maximum output power and a wavelength of 793nm. The target used is a P-753.2CD piezoelectric transducer (PZT) from Physik Instrumente (PI), equipped with an integrated capacitive sensor which allows monitoring the motion of the transducer with an accuracy of 2nm, which will be used as a reference sensor in all experiments. The PZT is controlled by the LVPZT controller (E-665), driven by a function generator to generate harmonic or arbitrary displacements of the PZT.

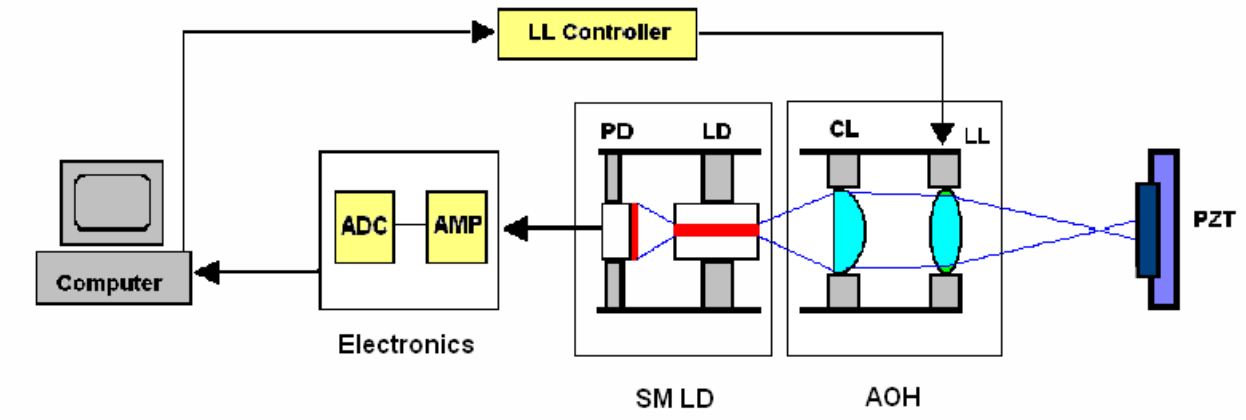

Figure 3.17. Schematic diagram of the experimental setup for OFI with AOH.

The OOP of the LD is monitored using the integrated monitor photodiode, whose signal after amplification is monitored using the oscilloscope. The oscilloscope uses an analog to digital converter (ADC) to turn the signal to digital, which is then acquired by the computer (PC) through a USB connection.

All experiments are performed on an optical table, which limits the maximum possible distance of the target from the LD to 280cm. The minimum possible distance of the target from the LD is about 25mm, limited by the size of the AOH assembly.

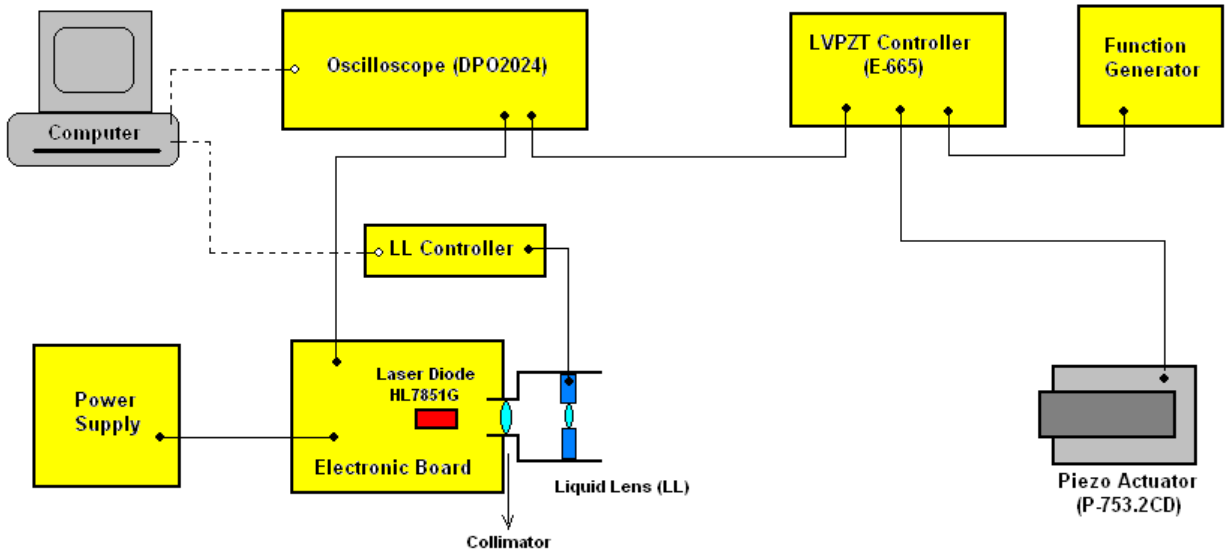

Figure 3.18. Arrangement of the laboratory equipment of the experimental setup.

3.b.2. Algorithm for adaptive feedback control

As commented in the introduction, one of the potential applications of adaptive feedback control is removing the need for a skilled technician to manually adjust the feedback level of the laser, automating

the arrangement and performance of OFI setups. This requires an automated feedback control algorithm, which is proposed next, although has not been implemented in practice within this Thesis. The algorithm for feedback control we propose for OFI is based on monitoring the SNR value and the coupling factor (C) of the acquired OOP signal, and then changing the focal point of the optical system when needed. Fig. 3.19 presents the block diagram of the algorithm. SNR and the C value of the OOP signal are the parameters used as gauges of the control algorithm.

As discussed in section 2.c, to perform reliable measurements and correct fringe detection, the coupling factor should be kept close to 1, so giving a 20% tolerance to account for potential errors in the algorithms for estimation of C, acceptable values for the coupling factor are kept between 0.8 and 1.2 as C_{min} and C_{max}. Applying some fringe-loss compensation algorithm [Zabit 2010], the desired regime for processing could be in the moderate regime with C values from 1 to 4.6.

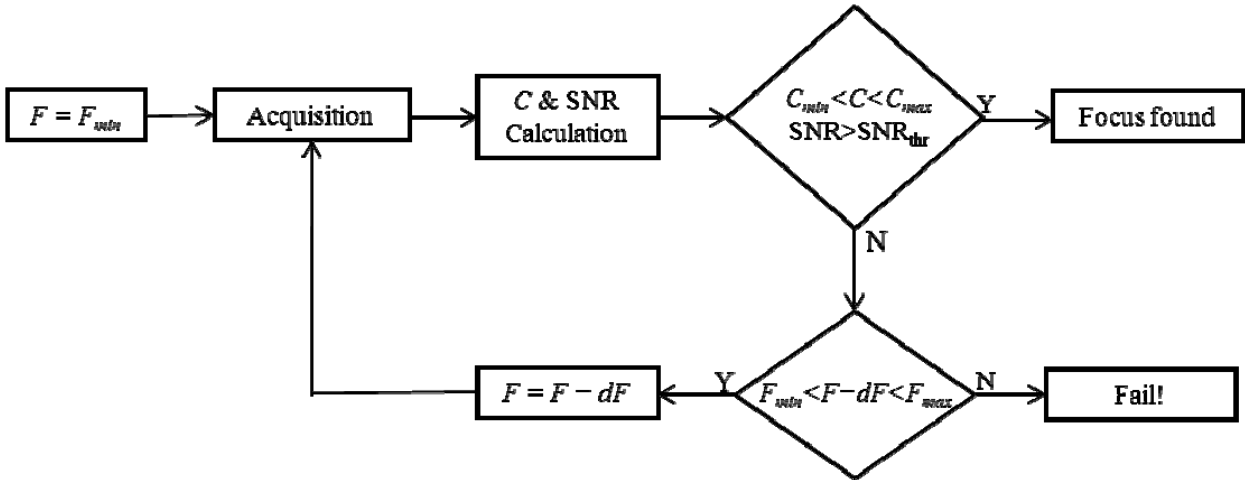

Figure 3.19. Block diagram of the adaptive feedback control algorithm.

Besides, it should be considered that the OOP signal can become noisy, introducing fringe losses due to problems in its detection, rather than due to hysteresis. Therefore, an additional metric of quality for avoiding too noisy signals is introduced through the use of the SNR of the signal, which is kept above a given threshold value SNR_{thr}, which defines the minimum SNR value where the signal is reconstructed reliably.

In the control algorithm, the focal length is started at F_{min}, where F_{min} is the closest focus position which can be achieved using the AOH. Then the OOP signal is acquired, and the SNR and C values are recovered. Given that the C value obtained is between C_{min} and C_{max}, and that the SNR is higher than SNR_{thr}, the focal length applied is considered adequate for its measurement. If C or the SNR values are not in the desired range, then the focal length is changed to $F + dF$ (taking about 80ms) where dF is the minimum focus step enabled by the AOH, corresponding to a 0.1V change of the LL voltage. The process is iterated until the desired regime is obtained.

As the OOP signal of the LD under feedback is comparable to that in an electrocardiogram (ECG), the method of SNR calculation used for ECG signals [Gautam 2008] is applied to the OOP signal to obtain the SNR of the signal, which is an original proposal of this PhD Thesis. To calculate C, the PUM method described in subsection 2.d.2.3 has been used.

In this thesis, this algorithm has not been implemented in closed loop for feedback control and it is left as potential future work. However, its feasibility is experimentally checked in the following section where the experimental results validate the feedback adjustments by the AOH.

3.b.3. Experimental results

The results for feedback control will have two separate steps. First, we will demonstrate the capability of the AOH for changing the optical feedback of the laser and keeping it in a certain regime for a vibrating target at a certain distance. Next, we will show the ability of the AOH to keep the feedback level in moderate regime without fringe loss for target distances ranging from a few centimeters to some meters.

Figure 3.20 shows the OOP signals of the LD obtained at four different focus conditions achieved by the AOH for a vibrating target at a fixed distance of D = 60cm. In this measurement, the PZT excitation was a sinusoidal harmonic signal with peak to peak amplitude of ΔD = 4.50μm and a frequency of 100Hz. The target surface in all measurements was a metallic diffusive surface.

As far as the appearance of each fringe is due to a target displacement of $\lambda/2$, the expected number of fringes N (N = round ($2\Delta D/\lambda$)) in each half period of the oscillation is 11. The fringe loss condition resulting in a wrong number of fringes presented in Fig. 3.20 (a) to (c) is due to the large hysteresis caused by the large feedback strength achieved, with an important amount of the energy emitted re-entering the cavity, as described in section 2.c.

A well-focused status of the beam on the target results in 8 fringes in each half period of target oscillation (Fig. 3.20a). Then, by increasing the spot size on the target by changing the LL focal length, one lost fringe reappears (Fig. 3.20b), reducing the hysteresis in the OOP signal by reducing the amount of laser light re-injected in the cavity. Further increases in spot size bring on the recovery of another lost fringe (Fig. 3.20c), and finally achieve the desired signals in moderate regime with low hysteresis and no fringe-loss (Fig. 3.20d), adequate for accurate measurements. Therefore, by using the LL focus variation capacities, lost fringes were recovered leading to keep the signal in moderate regime, enabling accurate measurement of displacement. Furthermore, the feedback level was shown to be directly controlled using the change in voltage at the LL.

Obviously, in the described FCM method presented in subsection 2.d.2.1, losing a fringe increases the measurement inaccuracy in half wavelength. More accurate signal reconstruction methods like PUM also can have important accuracy losses in the presence of lost fringe(s) [Zabit 2010]. Table 3.2 shows the C and Φ values estimated by PUM for each of OOP signals presented in Fig. 3.20. As it can be seen, a

better focusing of the spot results in a heavier fringe-loss condition, and in a higher *C* value leading to larger hysteresis. By increasing the spot size the feedback level is consistently changed, modifying the value of C, and the OOP signal can be kept in a regime having a proper set of (*C, Φ*) values, avoiding fringe-loss. No relevant changes in the feedback phase *Φ* are observed due to the modifications in spot size.

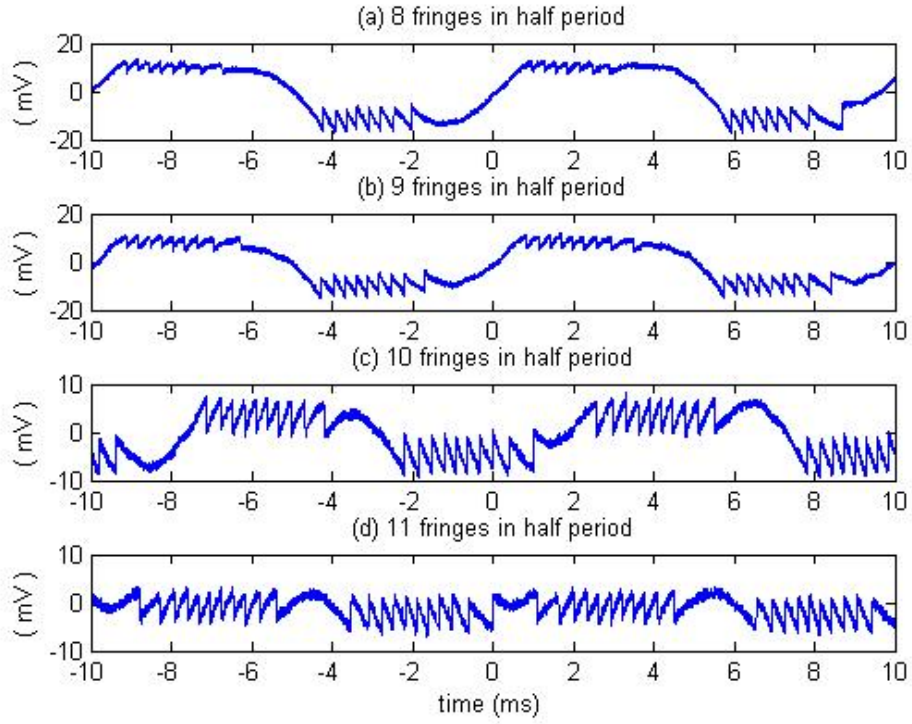

Figure 3.20. Experimental OOP signals for a 785nm LD for a target distance of *D* = 60cm, a vibration amplitude of Δ*D* = 4.50μm and vibration frequency of 100Hz for various focus of the laser beam generated using the AOH. [Atashkhooei 2011a]

Table 3.2. Influence of fringe-loss in the value of the coupling factor *C* and the feedback phase *Φ*(rad) for the signals obtained in Fig. 3.20.

Focus Condition	(a)	(b)	(c)	(d)
No. of fringes (N)	8	9	10	11
Coupling factor (C)	7.8	6.7	5.6	4.1
Feedback phase (Φ(rad))	4.1	4.0	4.1	3.9

Another interesting feature of the AOH is its capability to overcome the limits in the OOP signal imposed by the distance to the target. According to equation (2.15), the modification of the laser-target distance *D* directly modifies *C* value. However, changes in *D* affect also other parameters relevant to *C*, like the total

attenuation of the beam, so the total amount of back-reflected light re-entering the cavity can be modified. Usually, for a cooperative target at far distances (>1m), the moderate regime signal with large hysteresis is achieved. Decreasing D down to a few centimeters may change the moderate feedback regime to the weak regime implying directional ambiguities. Reversely, increasing D value can result in a large increase in C and in fringe-loss behavior. Thus, a direct application of our AOH is to keep the LD under moderate regime feedback with no fringe-loss conditions keeping the set of (C, Φ) at the proper values for a large amount of D values, allowing accurate measurement of the amplitude of vibration in the full distance range.

Figures 3.21(a) to 3.21(d) show the acquired signal using the conventional OFI optical setup, which uses a mechanically adjustable fixed focal lens with the beam focused to infinity to be able to recover a proper OOP signal in a large distance range from the target. In our setup, we used the collimating lens without LL in that role. Under this measurement conditions, D is varied from 6.5cm to 280cm, while the amplitude of target vibration is kept constant at 4.50μm. Thus, 11 fringes should be recovered in each half period of oscillation of the target.

As may be seen, in Figs. 3.21(a) and 3.21(b), the expected 11 fringes at each half period are obtained. However, when the distance to the target D increases the coupling coefficient C also increases (equation (2.15)), and hysteresis effects start to appear. At D = 150cm two of the fringes are lost, with the subsequent inaccuracy in the measurement. When D was raised to 280cm, the maximum distance attainable on the optical table, it was found that just one fringe was lost, because of the significant increase in total attenuation which appears at such distance.

Figures 3.21(e) to 3.21(h) show the OOP signals obtained using the AOH under the same measurement conditions described in Figures 3.21(a) to (d). Notice how the use of the AOH can keep the OOP signal in the low hysteresis moderate regime condition at all distances, recovering the expected 11 fringes for the complete distance range. Attenuation is now observed only in the reduced amplitude of the OOP signal.

Table 3.3 presents the C, Φ and N estimated values for the measurements performed by the two optical systems at different distances. Values of C and Φ were again calculated using the PUM method described in subsection 2.d.2.3. For the signals obtained using fixed focal optics, the C value consistently increases when the distance is increased from 6.5cm to 150cm, while at D = 280cm the C value slightly decreases due to larger power attenuation at large distances, following the expected trend in equation (2.15). C values obtained using the AOH may be seen to be in the moderate regime at all times. Again, no significant effect on the feedback phase is detected.

The coupling coefficients obtained are consistent with the corresponding OOP signals. At D = 6.5 cm, the fixed focal optics gets the signal in weak regime (C = 0.8) while using the AOH we could find the moderate regime signal (C = 1.6) allowing in both cases the desired accurate signal reconstruction. At D=75cm, both systems still present OOP signals in the moderate regime.

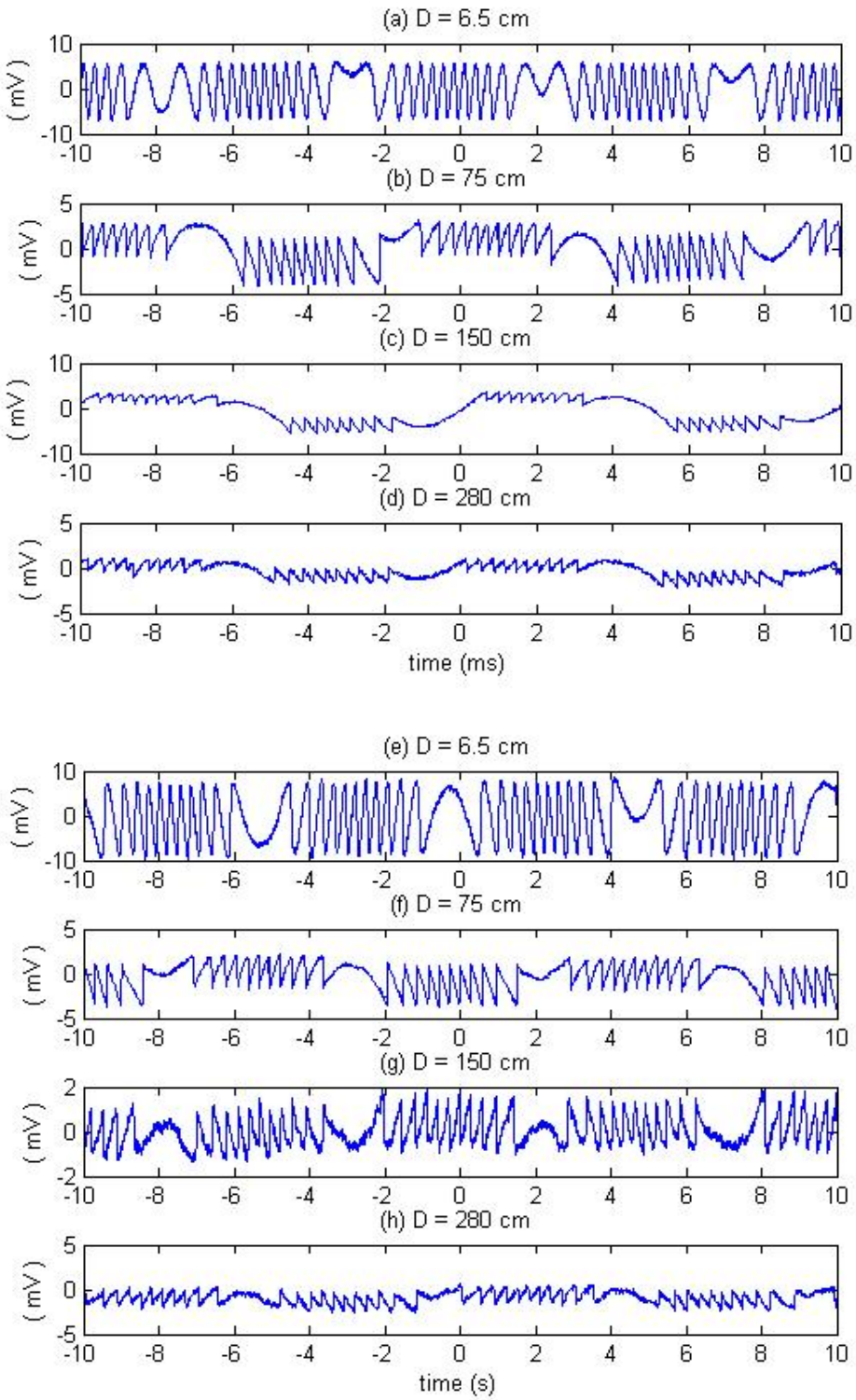

Figure 3.21. Experimental OOP signals for a 785nm LD for distances increasing from 6.5cm to 280cm with a vibration amplitude of ΔD = 4.50μm and a vibration frequency of 100Hz. (a) to (d) correspond to signals acquired using a fixed focal lens; signals in (c) and (d) present hysteresis and fringe-loss; (e) to (h) correspond to acquired signals using the AOH, where no fringe-loss appears in the whole distance range. [Atashkhooei 2011a]

Table 3.3. Influence of changes in distance on the coupling factor *C*, feedback phase *Φ* and number of fringes detected, with ΔD = 4.50μm for both optical systems. The performance of a collimating lens focused at infinity (CL) and the AOH are compared.

D(cm)	Obtained by CL			Obtained by AOH		
	C	Φ(rad)	N	C	Φ(rad)	N
6.5	0.8	3.7	11	1.6	4.6	11
75	4.2	4.6	11	3.8	4.0	11
150	6.1	4.2	9	3.2	4.2	11
280	5.8	4.5	10	4.2	4.4	11

At D =150cm and 280cm, the fixed focal optics can't keep the LD in a regime without hysteresis and fringe-loss occurs, while the AOH can control the feedback level keeping the signal in moderate regime, avoiding fringe-loss. Results demonstrate how the proposed AOH can be used to keep the C value between 1 and 4.6 at all distances, keeping the signal in the desired moderate feedback regime in all cases. PUM has been used as reconstruction technique for all measurements of vibration. The error obtained when compared with the reference capacitive sensor for the OOP signals using AOH was less than $\lambda/16$ at all distances, in agreement with the typical resolution of the method. Figure 3.22 presents the displacement reconstruction of the OOP signal obtained using AOH at D = 150cm shown in Fig. 3.21(g) compared to the reference signal from the capacitive sensor, showing very good agreement.

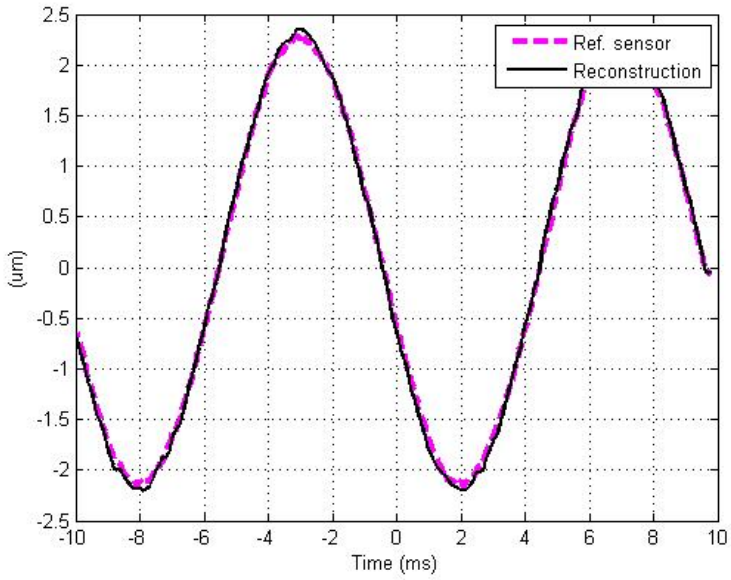

Figure 3.22. Displacement reconstruction of the OOP signal (shown in Fig. 3.21(g)) obtained using AOH configuration at D = 150cm, compared to the signal of the capacitive sensor used as reference. [Atashkhooei 2011a]

3.c. Differential optical feedback interferometry: a proposal for high resolution measurements

3.c.1. Introduction

Laser interferometry has long been used as a powerful metrology tool, where its use as a precise sensor from aerospace applications to research labs is now widespread. There is a considerable demand for robust and high precision sensors in several applications, like for instance in cantilever positioning in atomic force microscopy (AFM), for material characterization and for high accuracy positioning. Thus, a robust, compact, cost effective, and easy to use solution would for sure pave the way for a number of novel applications and opportunities. Thereby, in the past decade, a big effort has been made in the enhancement of performance of the OFI sensor regarding accuracy and resolution. However, it has typically been approached from the signal processing side, in particular using the PUM method, where the resolution of the technique was reduced to $\lambda/16$ (49 nm for λ = 784 nm) while with an additional pre-processing a resolution of $\lambda/25$ (~31.3 nm for λ = 784 nm) for weak feedback was reported [Wei 2007]. Other methods based on previous calibration also report resolution in the range of tens of nanometers.

In this section we are going to introduce and validate a concept which enables resolutions below the nanometer range in setups based on OFI sensors. Furthermore, it enables measurements of very small magnitude, well beyond the $\lambda/2$ limit imposed by the existence of the first fringe.

The proposal involves a setup with two LDs arranged in a such a way that one is oscillating and pointing to the target as measurement LD, while the other one is stationary and points towards the vibrating LD stage, which is used as reference sensor.

Figure 3.23 shows the schematic diagram of the proposed solution. According to the configuration, for a stationary target both LDs will have the same OOP signal, considering the same feedback regime has been adjusted using the AOH just described, and assuming both lasers have the same wavelength. When an unknown displacement is applied to the target, the measurement LD will present differences in its OOP which can be detected using the other LD as reference signal. The aim is to explore the feasibility of measuring accurately the unknown displacement out of the comparison of the two OOP signals. We have called the solution as Differential Optical Feedback Interferometry (DOFI).

Thus, what will be compared is the difference in the fringe positions of the two lasers involved. If the target is stationary, the fringes in both lasers should occur exactly at the same time in the signals. Any slight target displacement will introduce a slight difference in time on the fringes. The target displacement can be extracted out of the difference in fringe positions in the acquired sequence of both signals.

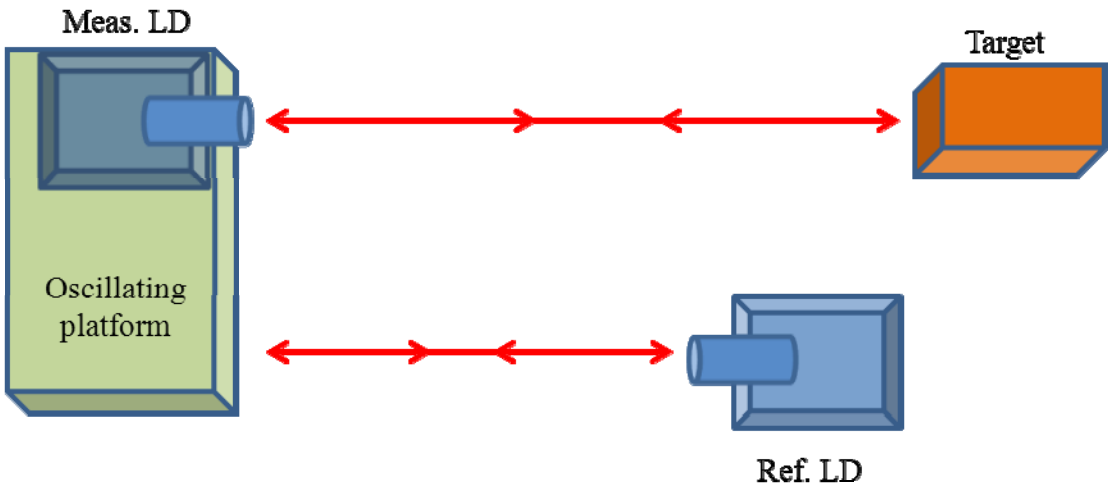

Figure 3.23. Schematic diagram of the configuration of DOFI.

Figure 3.24 depicts a typical case in which the target has undergone a small displacement. The position of the fringes in the measurement LD generated by the (sinusoidal) vibration of the LD mounted onto a piezoelectric actuator changes visibly when compared to the fringe positions obtained in the reference LD. This difference in the positions of the fringes enables us to measure the target displacement by comparing the OOPs. What really is appearing is a time delay in the appearance of a given fringe introduced by the change in optical path in one of the beams due to the movement of the target.

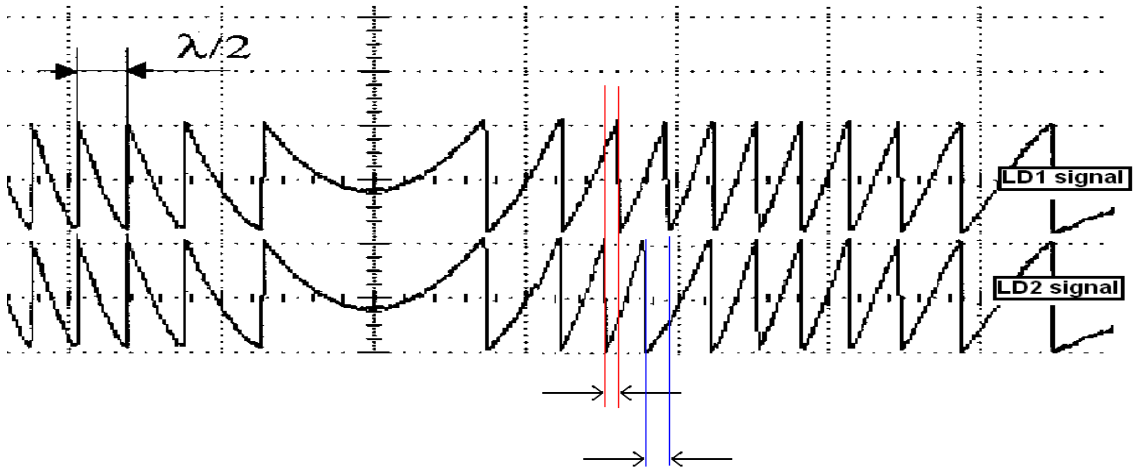

Figure 3.24. Fringes in the acquired sequence of the OOP signal for both LDs when the measurement LD is vibrating and there is a small target displacement. Differences in the positions of the fringes cary on the information on displacement of the target.

Ideally when the target is stationary both LDs should present the same fringe positions, but in practice it is not easy to get to that point as plenty of parameters introduce different types of noise and inaccuracies. Let us mention the most relevant. In order to have the same fringe positions for the two LDs, for instance, both LDs should have the same wavelength (which is not obvious at the nm level). Typically manufacturers specify a tolerance in the wavelength of the lasers which has a dispersion of a few nm.

Besides, it is well known that changes in the temperature of the laser junction may change the wavelength, meaning that a specific circuit for temperature control should be included in the modulation and amplification circuit to stabilize wavelength with temperature changes, and transient times need be considered when setting on the setup. Another very important parameter is the feedback regime, as far as both lasers should be in the same regime, preferably in the region in the frontier of the weak and moderate (C~1) feedback regimes to avoid fringe loss, achieving reliable fringe detection and having the same phase jumps in all the fringes. The SNR of the OOPs has also its usual and very relevant role in the accuracy of the fringe detection. To control both the feedback level and the desired SNR in both lasers, the use of the adaptive feedback control technique presented in the previous section of this Thesis is a perfect tool.

In the approach we are proposing, the resolution of the technique is fully related to the signal acquisition rate (the number of points per second acquired in the oscilloscope) and to the number of fringes per second, which we will define as the sampling rate (SR) of the technique. The SR is the number of fringes which appear in half a period of the displacement of the measurement diode, which can be obtained as

$$SR = \frac{\frac{a}{\lambda/2}}{T/2} = \frac{4a}{\lambda T} = \frac{4af}{\lambda} \tag{3.5}$$

Where a is the peak to peak amplitude of the vibration of the measurement LD, T is the period of the vibration and f is the frequency of the oscillation. Notice that several frequencies (lasers, displacement of the linear stage moving the measurement laser, sampling, signal acquisition) and amplitudes are involved in the description, so language can be quite tricky. An effort regarding this has been made but still attention is needed in order to understand what is being addressed in each moment.

Obviously, the larger the sampling rate, the better the resolution in displacement reconstruction which can be achieved. Besides, the displacement of each fringe carries on a certain amount of information about the displacement of the target, so having more fringes in the OOP signal due to a large displacement of the measurement diode increases the information we recover from the movement of the target. In order to have a uniform sampling in the fringes, the vibration of the measurement LD is selected to follow a triangular wave pattern. This means that fringes appear regularly spaced in time along the continuous slope of the displacement, until a slope change is introduced. A simple simulation experiment will be performed to clarify the details of the technique proposed.

This technique has been presented as first time in this thesis, so the contents of this section have been published as a PCT patent [Royo 2010]. Due to the complexities in the detailed implementation and analysis of the technique it has given rise to a new PhD work currently under development, which for the moment has given rise to the presentation of a paper [Azcona 2013b] and a publication in an international

conference [Azcona 2013a]. The work presented here corresponds only to the first results of the setup, performed in this PhD thesis.

In the following subsection, some details of the signal processing methods and the algorithms used for the complete reconstruction of displacement out of the differential management of the OOPs of the LDs will be presented. Later, in subsection 3.c.3, the simulation of the technique under different vibration conditions for the measurement LD, including signal shape and target amplitude, and the implementation of a linear approximation method in the reconstruction process to improve the accuracy will be described. Finally, in subsection 3.c.4, experimental results of a preliminary setup showing the validity of the approach will be shown.

3.c.2. Signal processing

The technique is based on the comparison of the fringe positions in the OOPs of the lasers, so the first step will be fringe detection using the classical FCM algorithm. The OOP of both lasers is first filtered, and then the derivative of the signal is calculated leading to the appearance of sharp peaks in the positions of the fringes. A threshold value detects the fringes in the conventional way, so the position of the fringes in the OOP signal is obtained and saved in an array as *FPOS(i)* where *i* is the fringe number in the OOP.

Hence the amplitude of the relative displacement of the target at the fringe position (displacement between two fringes) can be achieved by comparing the fringe positions in both OOPs as

$$\Delta D(i) = \left(\frac{\lambda}{2}\right).\left(\frac{FPOS_m(i) - FPOS_r(i)}{FPOS_r(i) - FPOS_r(i-1)}\right) \tag{3.6}$$

Where $FPOS_m(i)$ is the position of the *i*th fringe in the OOP of the measurement LD, $FPOS_r(i)$ is the position of the *i*th fringe in the OOP of the reference LD, and $\Delta D(i)$ is the relative displacement of the target at the *i*th fringe position.

After calculating the relative displacement at each fringe position, an integrator algorithm adds or subtracts the relative displacement to obtain the relative target displacement in terms of time. The complete signal processing procedure to obtain the target displacement is schematically depicted in Fig. 3.25.

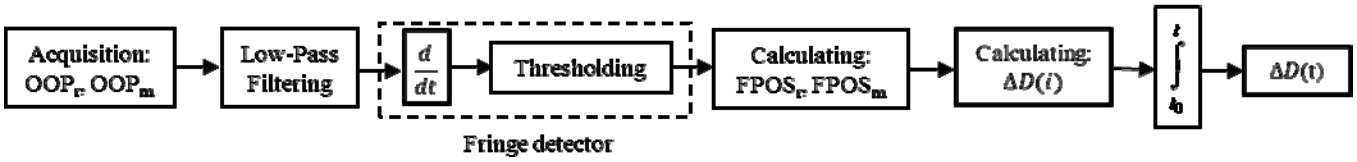

Figure 3.25. Block diagram of the signal processing procedure for DOFI solution.

An interesting feature of the technique is that the positive and negative values of the relative fringe displacement between the reference and measurement OOP signals contain the information on the direction of the displacement, so there is no directional ambiguity in the measurement of displacement.

In this Thesis we have only considered the two most simple methods for target displacement reconstruction, consisting in direct $\Delta D(t)$ estimation and in linear approximation. Direct $\Delta D(t)$ estimation simply returns the amplitude of the displacement at each fringe position, without any information in the regions without fringes. This leads to the typical staircase shape of the displacement signal. In the linear approximation case, the displacement in amplitude between the fringes is linearly approximated from the values at the previous and next fringes. The performance of both methods will be investigated in the next subsection by simulation.

3.c.3. Simulation

Once the proposed setup and its characteristics have been discussed, the feasibility and accuracy of the DOFI technique for high resolution measurement of displacement will be investigated by simulation. The OOP of a LD under feedback is simulated according to equations (2.14) and (2.21). The frequency of the laser under feedback is obtained from equation (2.14) using the mid-point method (also known as modified Euler method) [Griffiths 1991] and the value is used in equation (2.21) to determine the associated OOP value. The values of the parameters used in the simulation are shown in table 3.4 [Coldren 1995], which are typical values of the parameters used in the literature.

Table 3.4. Values of the parameters used in the simulation.

Parameter	Symbol	Value
Wavelength	λ (nm)	784
Light speed	c (m/S)	299792458
LEF	α	5
LD cavity length	L (μm)	500
Group refractive index	μ	4.5
LD front facet ref. coeff.	r_2	0.9
Target reflectivity	r_3	4.4×10^{-3}
Mode mismatch factor	ε	0.5
Target distance	d (m)	1
Frequency of vibration of the measurement LD	f (Hz)	100
Sampling in simulation	Points/S	21×10^{6}

In all simulations, parameters are set to obtain a coupling factor C close to 1 (C = 1.0), to avoid fringe loss and get reliable fringe detection. Feedback is thus in the frontier between weak and moderate feedback levels.

Thereby, based on the configuration of this technique, the simulated OOPs of both LDs for a small target movement (defined as the half-period of a sine-wave with a maximum amplitude of 100nm and a period of 6.6ms), considering a triangular oscillation of the measurement LD (with peak to peak amplitude of 20λ and frequency of 100Hz) are shown in Fig. 3.26. The sampling rate selected is 8kHz.

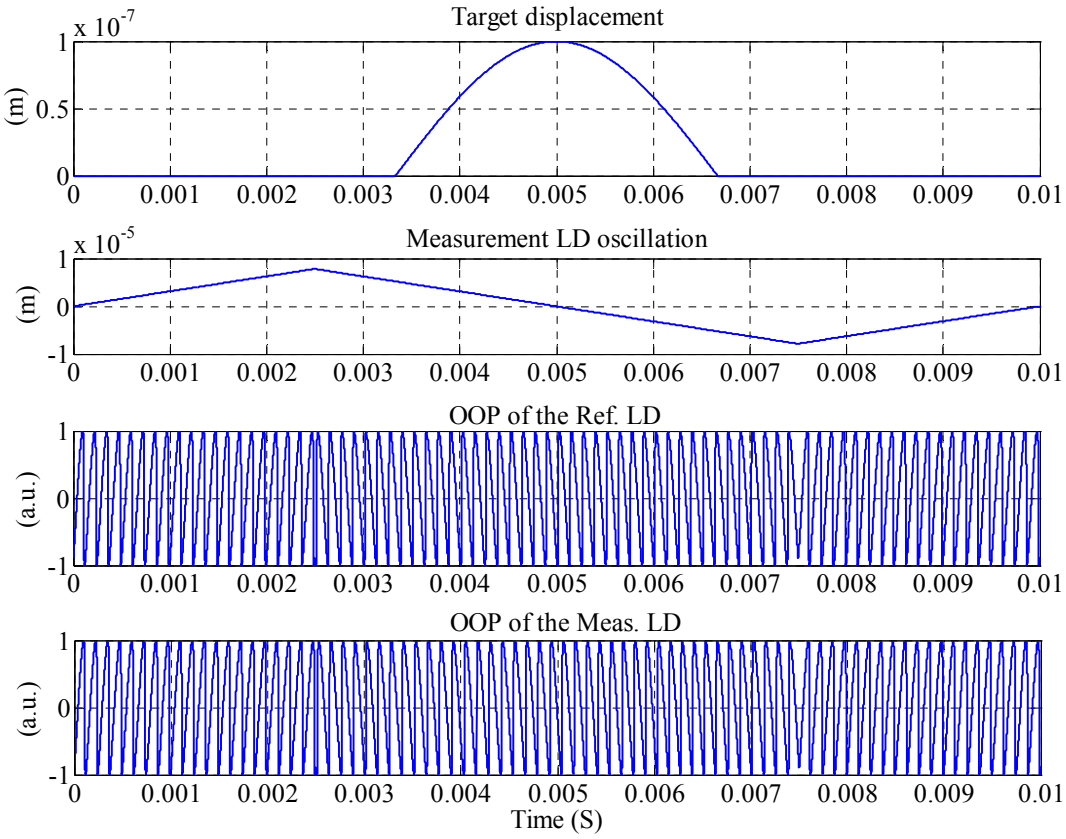

Figure 3.26. Simulation results for DOFI. Peak to peak amplitude of the oscillation of the measurement LD was 20λ with a frequency of 100Hz, sampling rate was 8kHz, target actuation of 3.3ms, and the simulation sampling of 210000 points per period.

The position of the detected fringes, the reconstructed displacement, and the error which appears in the target reconstruction (from the comparison of the reconstructed displacement and the original one) are presented in Fig. 3.27. According to the configuration of the proposed technique, the reference LD sees the optical path length difference (relative laser-target displacement) of the triangular waveform oscillation while the measurement LD senses the triangular waveform oscillation with the superimposed target displacement. In this simulation, the maximum error obtained was 11.37nm and the average error was 3.65nm. As seen in the figure, the reconstructed signal does not reach to exactly zero after the target vibration because of the relative nature of the technique, and due to the small quantization errors introduced in the determination of each fringe position.

To peek into the effect of changing the sampling rate in the accuracy of the measurement, the same simulation is now repeated with a higher sampling rate by applying a larger amplitude of displacement (5 times) of the triangular waveform oscillation of the measurement LD.

Figure 3.28 shows the results of the simulation for a measurement LD oscillation with peak to peak amplitude of 100λ. The sampling rate has thus been increased from 8kHz to 40kHz in the simulation. The maximum error has now decreased to only 2.65nm and the average error has reduced to 0.77nm.

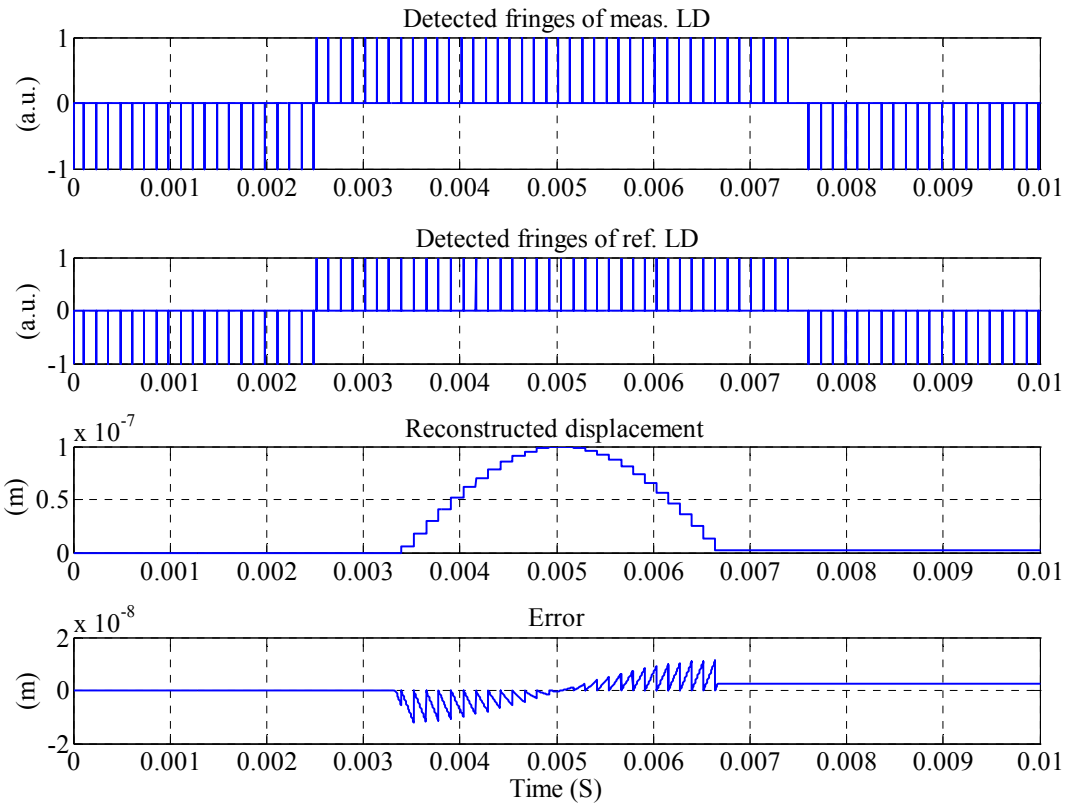

Figure 3.27. Simulation results for the DOFI. Detected fringes, reconstruction, and error obtained for the OOPs simulated in Fig. 3.26. The maximum error in amplitude obtained is 11.37nm and the average error reached to 3.65nm.

The value is roughly 5-fold smaller than the error achieved with the 5-fold lower sampling rate. Sampling rate, in the shape of large amplitude displacements of the measurement LD, has thus the expected direct effect on the accuracy of the results which can be achieved.

As suggested in the previous subsection, a linear approximation can be used to yield a more accurate reconstruction. Results using the linear approximation method are presented next. Figure 3.29 demonstrates the results of the simulation for a triangular oscillation of the measurement LD with a peak to peak amplitude of 20λ, using the linear approximation reconstruction.

The maximum error has been reduced to 2.38nm and to an average error of 0.07nm (which corresponds to 0.7% of the total amplitude in target displacement). The error values are significantly lower than the ones achieved by direct fringe counting. Thus, the use of the linear approximation method for reconstruction of the displacement of the target combined with a large sampling rate leads to improved accuracy in this DOFI technique.

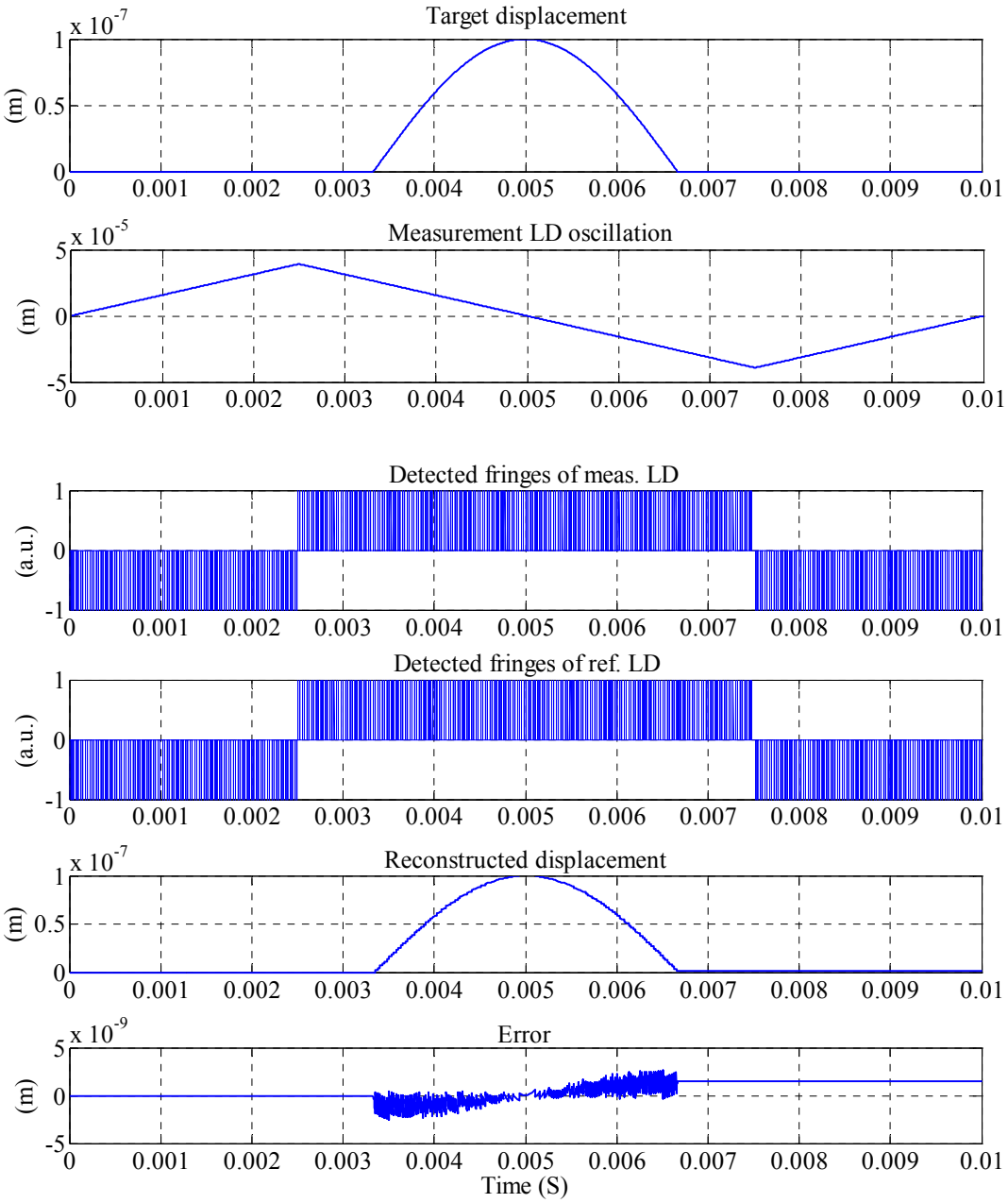

Figure 3.28. Simulation results for DOFI solution. Peak to peak amplitude of measurement LD oscillation was 100λ with frequency of 100Hz, sampling rate of 40kHz, target actuation length of 3.3ms, and the simulation sampling of 210000 points per period. The maximum error obtained is 2.65nm and the average error reached to 0.77nm.

3.c.4. Experimental results

In the real experimental setup some parameters appear which add noise in the measurements and further affect its accuracy. For a stationary target, both LDs should sense exactly the same displacement and present the same fringe positions. However, even neglecting the dissimilarities of the LDs, factors like ambient mechanical noise or couplings, lack of the mechanical robustness of the system, and electrical or electronic noise degrade the performance of the setup in the real measurement.

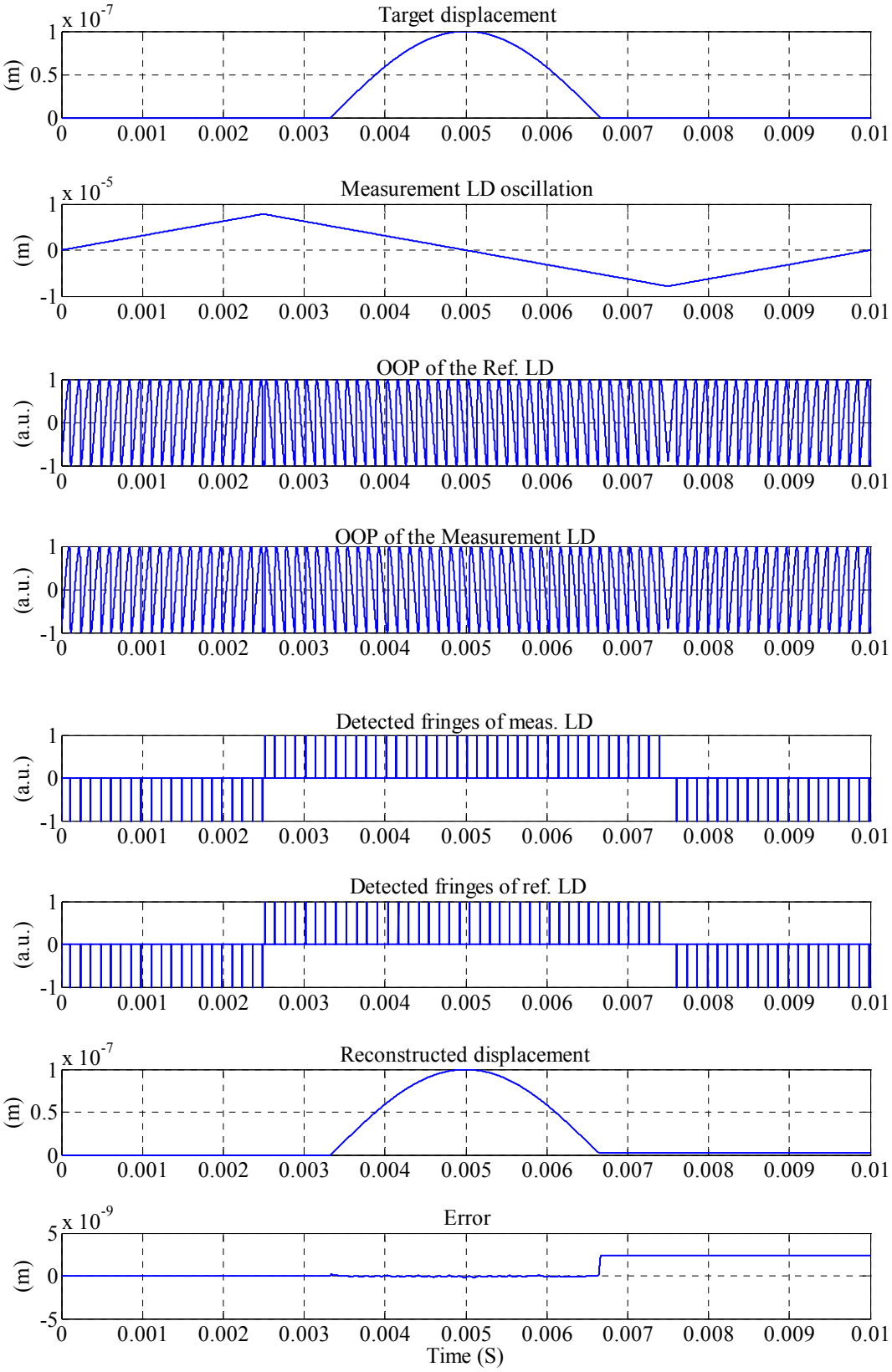

Figure 3.29. Simulation results for DOFI with linear approximation for reconstruction. Peak to peak amplitude of measurement LD oscillation was 20λ with frequency of 100Hz, sampling rate of 8kHz, target actuation length of 3.3ms, and the simulation sampling of 210000 points per period. The maximum error obtained is 2.38nm and the average error reached to 0.07nm.

Besides, having the coupling factor out of the desired range (C~1), especially when the regime is under high hysteresis implicating fringe loss, makes impossible for the technique to work properly. Therefore, we have used spot size adjustment in all experiments to be able to have the desired range of coupling factors for both lasers. This feedback control by spot size adjustment was done manually by moving the focusing lens mechanically until getting the proper focus condition, which resulted in the desired feedback regime. This feedback adjustment may be done precisely with the AOH presented in the section 3.a using the closed loop algorithm proposed in subsection 3.b.2.

Figure 3.30 depicts the measurement configuration we set for DOFI. Both LDs were Hitachi HL7851G LD emitting at a nominal wavelength of 784nm with a maximum output power of 50mW. The measurement LD was mounted on a P-753.2CD piezoelectric transducer (PZT) from Physik Instrumente (PI) oscillating with a frequency of 1Hz under a triangular-shaped signal of amplitude 40λ. To reduce possible mechanical coupling and noise, a very low frequency (1Hz) has been used as at higher frequencies the noise of the LD package may get higher. The target in this setup was a P-244 HVPZT piezoelectric translator, also from PI.

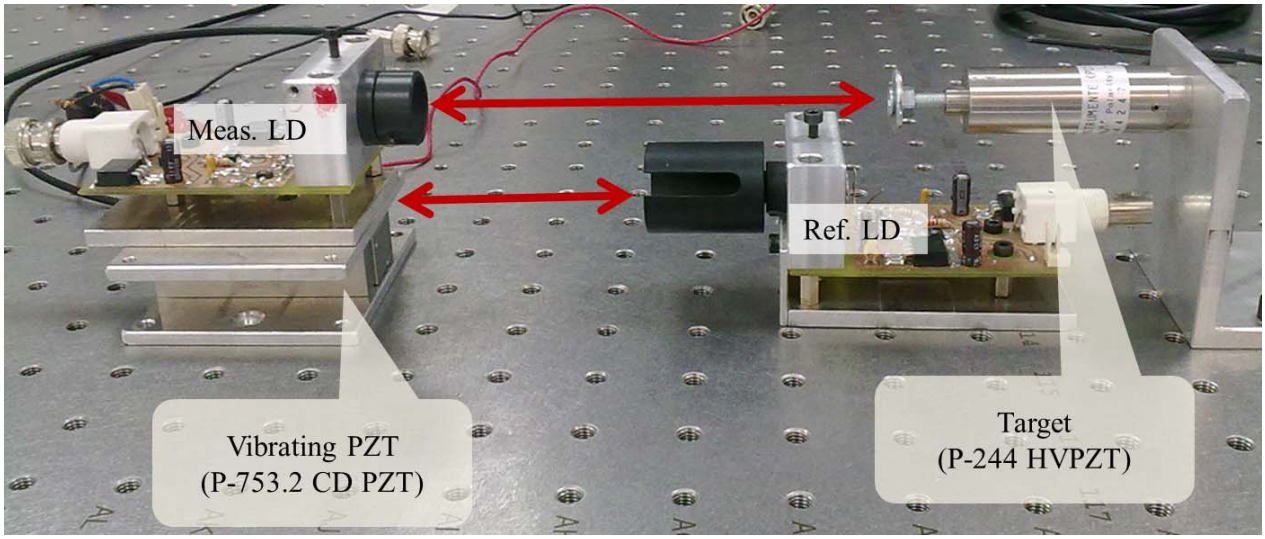

Figure 3.30. Experimental configuration for DOFI.

Figure 3.31 shows the measurement results and the reconstructed displacement using the linear approximation for the stationary target. Although it is expected to be zero, noise of different origin is added to the signal, so a virtual displacement with maximum amplitude of 7.2nm and an average of 0.35nm is present in the results when the target is at rest, setting a lower limit to the accuracy of the measurements under this setup. In this experiment, the sampling rate was 160Hz.

Figure 3.32 demonstrates the measurement results for a sinusoidal periodic perturbation of the target. The reconstructed displacement has been achieved using the linear approximation method. A sinusoidal target displacement with amplitude of 265nm at a frequency of 7.41Hz is applied to the P-244 HVPZT translator.

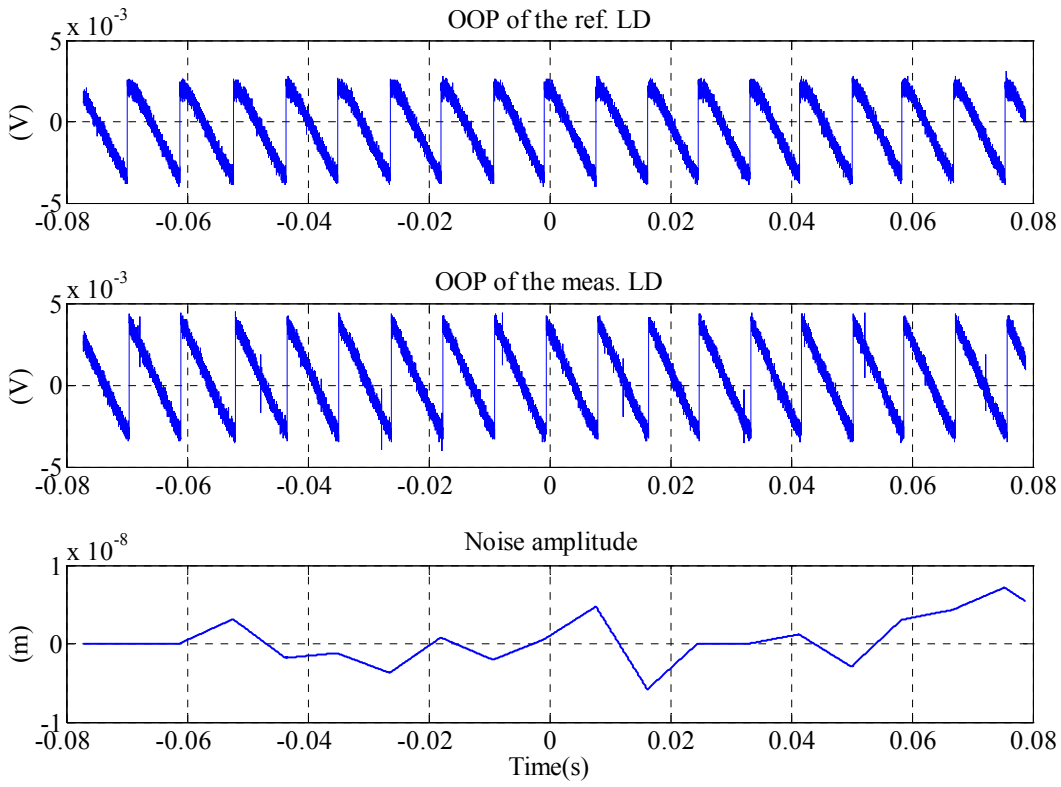

Figure 3.31. Experimental results for stationary target using DOFI solution. The measurement LD oscillation frequency was 1Hz and the sampling rate of the measurement was 160Hz. The Maximum noise achieved was 7.2nm and the noise average was 0.35nm.

A triangular-shaped waveform is applied to the P-753.2 CD PZT to vibrate the measurement LD with a frequency of 1Hz and a peak to peak amplitude of 40λ. The sampling rate was thus again 160Hz in the experiment.

The target displacement shown in the figure is the signal applied to the target PZT and has a high frequency noise which was eliminated using a low-pass filter. Comparing the reconstructed displacement with the target displacement signal results a maximum error of 20nm and an average error of 3.6nm. This is an average error close to λ/200 which, to our knowledge, is the largest accuracy ever claimed using OFI.

Several enhancements may be considered here yielding to further enhancements. The exact wavelength value of the LDs can be measured and differences taken into account in the algorithms. A mechanically more robust configuration and which takes better care of all coupling effects can be found. Stabilization of the temperature of the LDs is just a matter of improving the circuit. A reference capacitive signal in the target would provide a better evaluation of the error. All of these simple enhancements are expected to reduce the error values in the technique.

Besides, as explained in the introduction, to reduce the error, the coupling factor (*C*) for both lasers should be the same and close to one, so the use of adaptive optical head for feedback adjustment before

the measurements start will be required. Hence, the adaptive head may also be used to improve the performance of DOFI solution and reduce the errors.

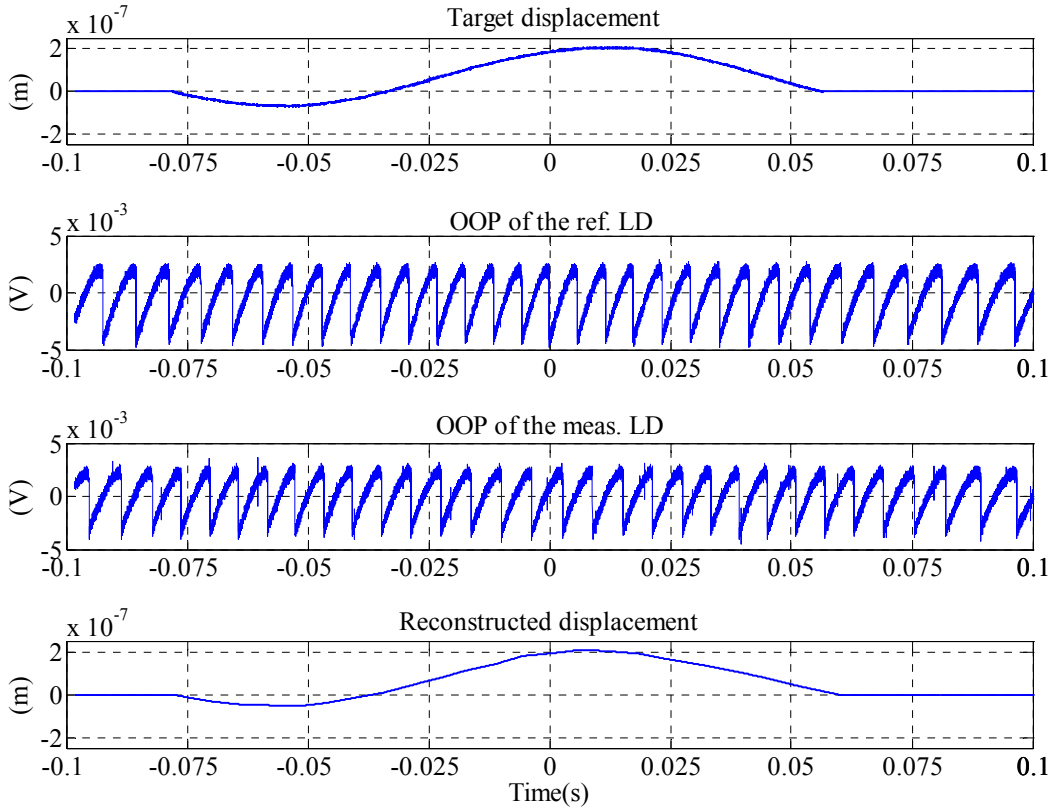

Figure 3.32. Experimental results for a sine perturbation of the target using DOFI and the linear approximation method. The measurement LD oscillation frequency was 1Hz and the sampling rate of the measurement was 160Hz. The target frequency was 7.41Hz with a peak to peak amplitude of 265nm.

Another very relevant contribution of the proposed technique is, for the first time, to enable OFI measurements to detect small displacements below $\lambda/2$. That is, measurements are done even considering that no fringe would be appearing in the OOP of a single, static LD pointing to the target. Prior to this proposal, the target displacement should be larger than $\lambda/2$ in order to be detectable.

3.d. Conclusion

In this chapter, we have studied the possible solutions for a variable-focus optical system for spot size adjustment by electrical modification of the focal length of a liquid lens, enabling to get the desired feedback level for accurate measurements.

Among the available solutions, voltage programmable electrowetting-based liquid lenses were found to be the best option for adaptive focusing in OFI. Thus, an adaptive optical head consisting of a LL and an

aspheric lens has been designed for large range focusing purposes, leading to the construction of a final prototype.

The performance of the presented AOH was tested for feedback adjustments. Experimental results showed its ability to modify the feedback level of the laser from weak to high hysteresis moderate regime, keeping the coupling factor in a desired range, and avoiding the fringe loss for a large range of target distances. Thereby, the feedback adjustments by the presented AOH has been proved experimentally and showed how the AOH may be considered as a reliable solution for feedback adjustment prior to the measurements, suitable for operator free conditions.

Also, we have presented the DOFI technique as a novel solution for high resolution measurements in which the AOH could be used for controlling the coupling factor. In this solution, two lasers (one vibrating, one stationary) having the same feedback level with $C\sim1$, are used so the positions of the fringes which appear in both OOPs are compared. Experimental results have shown an average error close to $\lambda/200$ which, to our knowledge, is the largest accuracy ever claimed using OFI. DOFI should be thus be considered a solution with very large potential due to its accuracy, combined with its compacity, robustness and low cost.

4. Speckle control in OFI

As described in section 2.e, the speckle effect is essentially due to the superposition of the coherent beams randomly scattered from a diffusive surface and appears as a granular interference pattern. In OFI there is no significant speckle effect when small displacements of the target (below 100μm) are involved, as far as the feedback and SNR levels may be normally adjusted, prior to the experiment, using a fixed focal lens to have the right feedback level and SNR of the OOP. When large displacements (from a few millimeters to some centimeters) are involved, the amplitude of the OOP is randomly modulated by the speckle effect, leading to frequent signal fading and subsequent signal loss, apart from the introduction of an undesired speckle phase error. In absence of the speckle effect, the basic resolution in OFI is $\lambda/2$ of the laser, which may be improved numerically to $\lambda/16$ using PUM. Speckle effect may introduce a considerable error in the measurement (estimated to be in the order of 10% for displacement measurements [Donati 2004]) which is hindering OFI to be used in a range of applications where large displacements with speckled signals are present.

As explained in section 2.e, the only practical solution to speckle presented in the literature is the BST technique, which uses an in-plane piezoelectric positioning system which moves the laser beam transversally (perpendicular to the laser beam) and scans the target surface during its displacement looking for a bright speckle spot. This solution is neither simple nor cost effective. Besides, during a large displacement of the target, the laser beam can become out of focus, leading to very weak backreflection and subsequent poor SNR in the OOP. A diffusive target undertaking large displacements in presence of the speckle effect makes complete detection of the signal extremely complex, even if BST is running.

As mentioned in section 2.e [Donati 2004], displacements below 0.1mm are usually considered as small displacements (essentially free of speckle effect in the OOP), while displacements over 0.1mm are considered as large displacements with noticeable speckle effects. However, this should be considered essentially as a rule of thumb, as (according to equation (2.37)), depending on wavelength, distance to the target, and the diameter of the lens used for focusing, displacements around or below 0.1mm may present one or a small number of amplitude fading zones in the OOP signal. For larger displacements the number of amplitude fading zones increases.

In this chapter, we will first analyze experimentally the speckle effect in OFI and the most relevant parameters affecting speckle modulation in the experiments, including the characterization of the speckled OOP signal, the effect of the average roughness of the target, and the effect of spot size. Then, two efficient solutions to deal with speckle effect adapted to slow motion and fast motion applications will be proposed, and experimental results will be presented.

The two methods which will be proposed in this chapter for compensation of speckle effects are thus specially suited for such large displacements, although they can also be adequate under given conditions

to experiments with smaller displacements, where the manual refocusing of the imaging lens to find a proper SNR of the signal is conventionally used to manage the speckle. This conventional refocusing procedure enables to modify the size and position of the bright speckle region to reduce the frequency of appearance of the fading zones in the signal. This can be used to deal with one or two fading zone(s) along the displacement, although typically not for complete elimination of speckle. Two experimental examples in industrial environment of this speckle management approach will be developed in depth in chapter 5.

However, when larger displacements are to be managed we propose to use an adaptive control of speckle. The AOH described in last chapter may be used to enable real time control of the speckle effect. During target displacement, an active tracking technique is applied so whenever the signal gets into the fading zone, meaning that low SNR is observed, the spot size is adjusted by changing the focal of the liquid lens, modifying the speckle pattern and the feedback level if required, in order to get the signal out of the fading zone. The details of this approach, including the implemented algorithm and experimental results, are presented in section 4.b.

The second solution we propose is a sensor diversity technique, based on two lasers of different characteristics pointing to the same target at neighboring points. The goal is to combine for a single measurement the OOP of two lasers with different features, creating different speckle patterns which may be combined to yield an accurate signal reconstruction. This technique significantly reduces the probability of errors due to reduction of SNR in a single OOP signal, although does not completely eliminate the possibility of an error due to signal fading. However, it has the advantage of not being limited by the response time of the feedback loop, as the real-time algorithm presented in section 4.b. This diversity approach, especially suitable for fast-moving targets, is presented in section 4.c. Finally, we will close this chapter with a brief conclusion.

The solutions and applications presented in this section are novel approaches to a general problem in OFI. Out of the results of this chapter we have published a journal paper [Atashkhooei 2013a] and a conference paper [Atashkhooei 2011c] related to the analysis of speckle effect in OFI, and the solutions to deal with it presented in this chapter. Another paper is currently submitted [Atashkhooei 2013c] based on the active control of speckle effect in large displacements.

4.a. Analysis of speckle effect in OFI

4.a.1. Characterization of the speckle affected OOP signal

As a starting point in speckle management we will be interested in the characterization of the speckle affected OOP signal. We will calculate the coupling factor C at different regions of the acquired OOP

signal to better understand its relationship with the appearance of speckle. Equation 2.15 describes the coupling factor, and can also be written as [Giuliani 2002]

$$C = \frac{D}{\sqrt{A}} \frac{\varepsilon\sqrt{1+\alpha^2}}{l_{las} n_{las}} \frac{1-R_2}{\sqrt{R_2}} \tag{4.1}$$

Where D is the laser-to-target distance, A is the total power attenuation in the external cavity composed by the front facet of the laser and the target, α is the linewidth enhancement factor, ε is the mismatch between the reflected and lasing modes, l_{las} is the laser cavity length, n_{las} is the refractive index of the cavity and R_2 represents the power reflectivity of the front facet of the LD.

Figure 4.1 shows a typical speckle affected OOP signal obtained for a large target displacement of 20mm. The target used is a ground metallic surface [Edmund] with average roughness value (R_a) of 0.2µm, initially placed at 17cm from the LD and moved towards the laser until it was at 15cm from the LD.

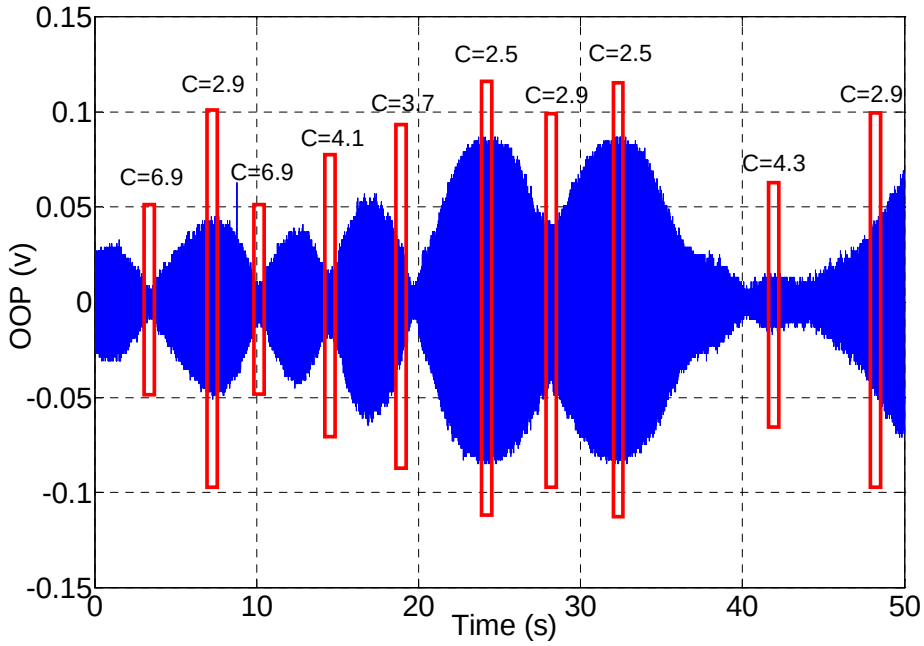

Figure 4.1. A typical measurement result of speckle modulated OOP. Shown C values are the values of coupling factor calculated by PUM method for the selected area of the signal.

The C values presented have been calculated using the PUM method for a number of selected regions of the signal, shown in the figure. As shown in Fig. 4.1, very relevant changes in the amplitude of the OOP appear during the longitudinal target displacement because of speckle modulation of the signal, leading to strong SNR variations in the OOP.

A more interesting feature, however, is how consistently the value of C varies in a given pattern for these SNR changes. The C value found in fading regions can increase up to 6.9, while in larger amplitude zones it stays in smaller values. Such a large feedback level in the fading regions suggests that fringe loss

condition probably will appear in these regions. In addition, the OOP amplitude in a fading zone may be decreased down to the noise level, making very complex to properly recognize the interference fringes. Both effects bring on relevant inaccuracies in displacement reconstruction procedures which need be addressed using proper experimental approaches.

4.a.2. Effect of the average roughness of the surface

In order to analyze the relationship of the frequency of the speckle modulation of the OOP with the average roughness parameter (R_a) of the target, we have used commercially available surfaces with different standard roughness values [Edmund], including 6 different specimens with calibrated R_a values of 0.05, 0.1, 0.2, 0.4, 0.8 and 1.6μm, which were used as targets. For all surfaces, the target was moved from *D*=17cm to 13cm from the LD (corresponding to a 40mm displacement), and the number of local maxima in the OOP signal was counted. The experimental configuration for the measurements is presented in Fig. 4.2.

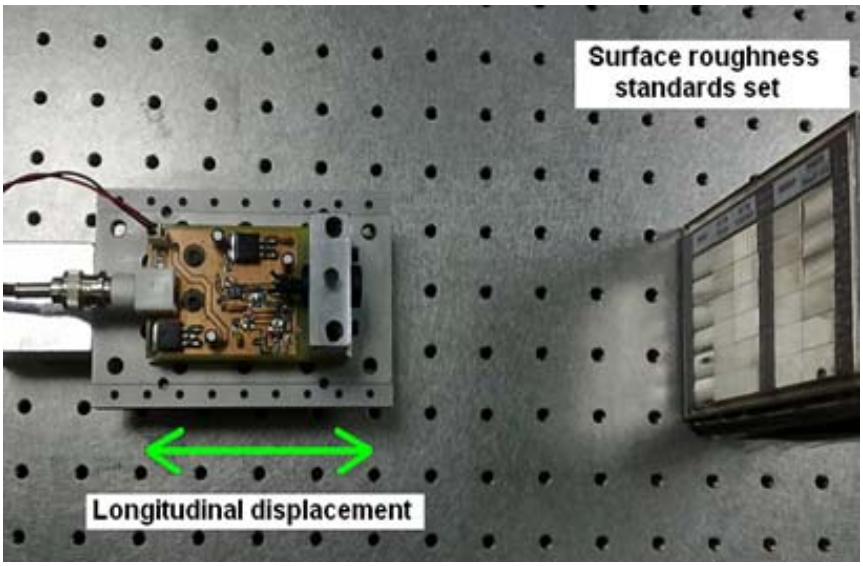

Figure 4.2. Experimental configuration for generating the speckle pattern using standard roughness surfaces with calibrated R_a values of 0.05, 0.1, 0.2, 0.4, 0.8, and 1.6μm for longitudinal relative surface displacement of 40mm.

Figure 4.3 shows how the number of maxima decreases when the R_a value increases from 0.05 to 0.4μm, which is roughly half the wavelength of the laser diode (783nm). For R_a values ranging from 0.4μm to 1.6μm the number of maxima remains constant at a value of 4. This curve is in good agreement with equivalent ones obtained in the literature for transversal speckle pattern appearance [Wang 1998].

Figure 4.4 shows the results obtained by Wang using the configuration depicted in Fig. 4.5. There the surface is moved transversally (perpendicular to the direction of the laser beam, in difference with our setup) and the laser beam (a He-Ne laser with wavelength of 632.8nm) illuminating the surface is backreflected to the CCD camera, which acquires the image of the backscattered beam.

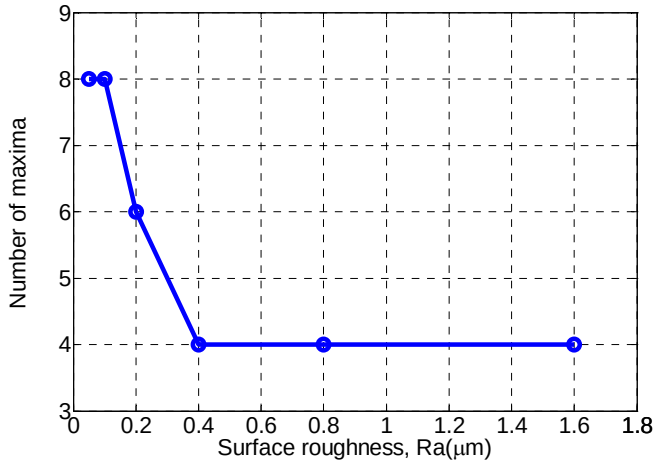

Figure 4.3. Experimental number of local maxima in OOP against surface roughness.

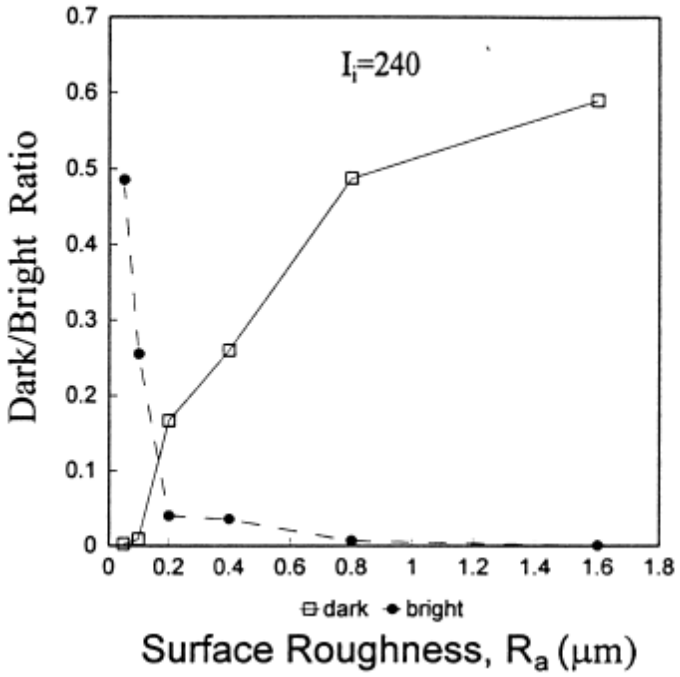

Figure 4.4. Relation of bright ratio (dots) and dark ratio (squares) to surface roughness [Wang 1998].

Using the image card and a micro-computer, bright and dark ratios in the captured image were calculated where the bright/dark ratios are defined as the ratio of the number of pixels with high (bright) and low (dark) grey levels to the total number of pixels of the image pattern analyzed. The threshold value of the grey level for bright/dark classification in the 8-bit card was optimized using a value of 50 for dark and 230 for bright ratio, with 255 as the maximum grey level in the image. These values were optimized in the experiment to find clear changes in the ratios for the surface roughness range of R_a = 0.05 – 0.8μm. As seen, the bright ratio (dots in Figure 4.4) decreases when the R_a value increases from 0.05 to 0.2μm, which is again roughly close to the half wavelength of the laser. For R_a values ranging from 0.2μm to 1.6μm the number of maxima remains almost constant.

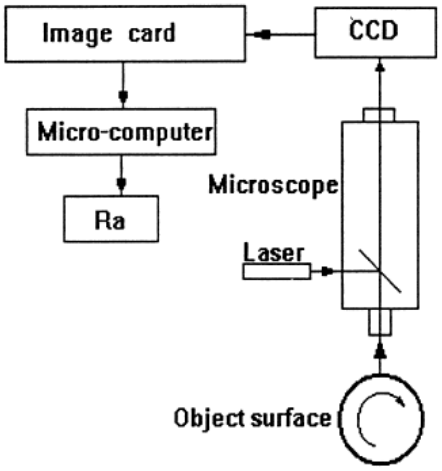

Figure 4.5. System for measuring surface roughness using speckle pattern analysis for transversally moving surfaces [Wang 1998].

The comparison of Fig. 4.3 and Fig. 4.4 shows that the behavior of the number of maxima obtained from the OOP signal analysis in our experiment follows a pattern closely similar to the curve of bright ratio obtained for the surface roughness values from 0.05 to 1.6μm. Thereby, it can be shown how a relationship of the number of fading regions to surface roughness exists. As a rule of thumb, for R_a values below half-wavelength of the laser, the number of fading regions present in the signal increases in large displacements, a fact which should be considered when choosing any speckle control technique.

4.a.3. Effect of spot size

Since speckle modulation appears due to the random nature of surface backscattering, by changing the spot size on the target (through changing the position of the focusing lens) the conditions for the random superposition will change and subsequently the positions of both the maxima and the fading region regions may be modified. As far as we use a focusing lens in OFI, the speckles which appear in the OOP respond to the description of subjective speckles (see section 2.e). Apparently, according to equation (2.37), changes in spot size should not affect the average speckle sizes if laser wavelength, distance from the target and beam diameter on the lens are kept constant. However, as far as we are not interested in the average value but on the position of a given speckle spot which reduces the SNR of the OOP we are considering, changes in spot size modify the speckle pattern and the position of fading regions to our advantage.

We will experimentally show the effect of the modification of spot size in the speckle modulation of the OOP signal, both for large and small amplitude displacements of the target. Figure 4.6 shows two OOP signals obtained using the same setup with different spot sizes, using the same laser diode and target. In this experimental example for large amplitude displacement, the target used had an average roughness of 0.8μm and was displaced along 40mm.

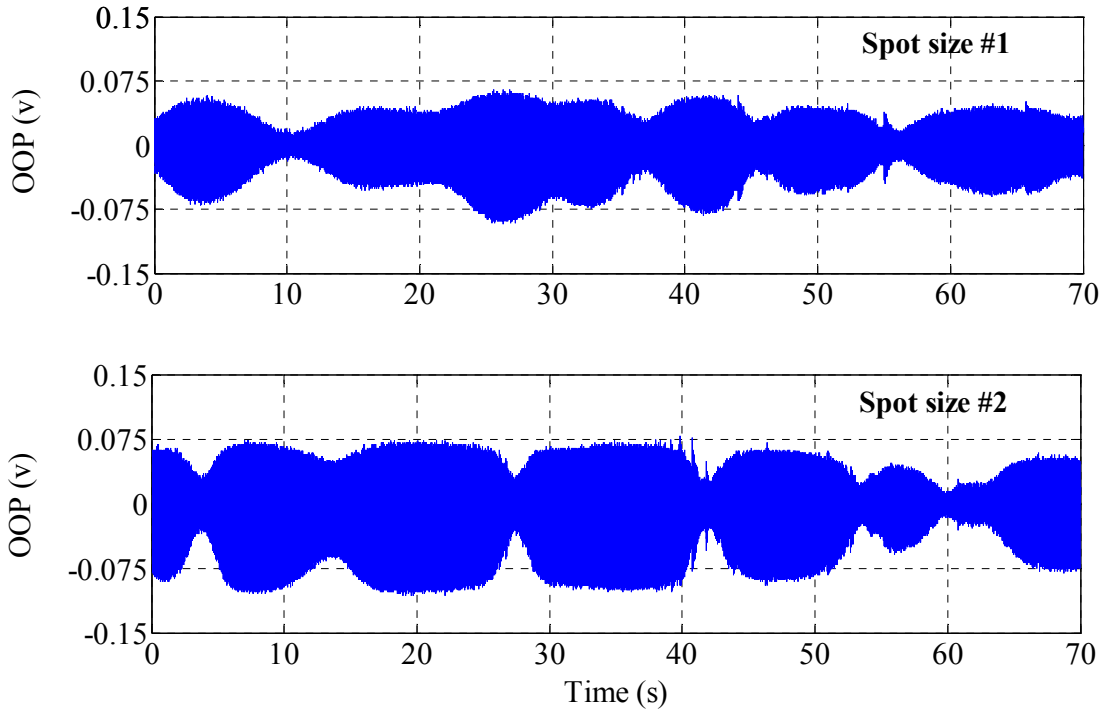

Figure 4.6. Two OOP signals achieved for the target displacement of 40mm in the same setup, changing only the spot size on the target.

The average FWHM of the spot on the target in the first signal was 71µm and in the second signal it was modified to 54µm. The FWHM of the laser spot on the target was measured using a CCD camera placed at the location of the target. The spot image captured by the camera was processed to obtain the average FWHM value. It can be seen how under changes in spot size both the positions of the maxima and the fading regions may be modified.

When small amplitude displacements are considered, however, the system can be totally inside the bright or dark speckle spot, leading to a large amplitude of the OOP with high SNR, or to a low amplitude of the OOP with the subsequent low SNR. In small amplitude situations typically the position of the lens is modified manually to leave operating conditions under a reasonable SNR ratio, which if the displacement is small does not undergo substantial changes. To experimentally investigate the speckle effect on the amplitude of the OOP under changes in spot size, the target was placed at a fixed distance and set to vibrate sinusoidally, with a peak to peak amplitude of 5µm and a frequency of 100Hz. During the measurement, the AOH modified its focal length so the best image of the laser (understood as the point yielding minimum spot size) moved from 35cm to 7.5cm from the laser, in steps of 0.35V of the LL. This 0.35V steps corresponded, approximately, to a change of 0.7cm in the position of the best image of the laser, which subsequently modified the spot size on the target.

Figure 4.7 shows how the mean amplitude of the OOP of the LD under feedback varies by changing the spot size at two different fixed distances of the target (27.5cm and 31cm). Arrows indicate the position

where the target was at the best image of the laser, corresponding to minimum spot size. As seen in the results, changing the position of the image of the laser from a distance which is farther than the target and moving it to the closest possible point modifies the OOP amplitude in a random and quite unpredictable way.

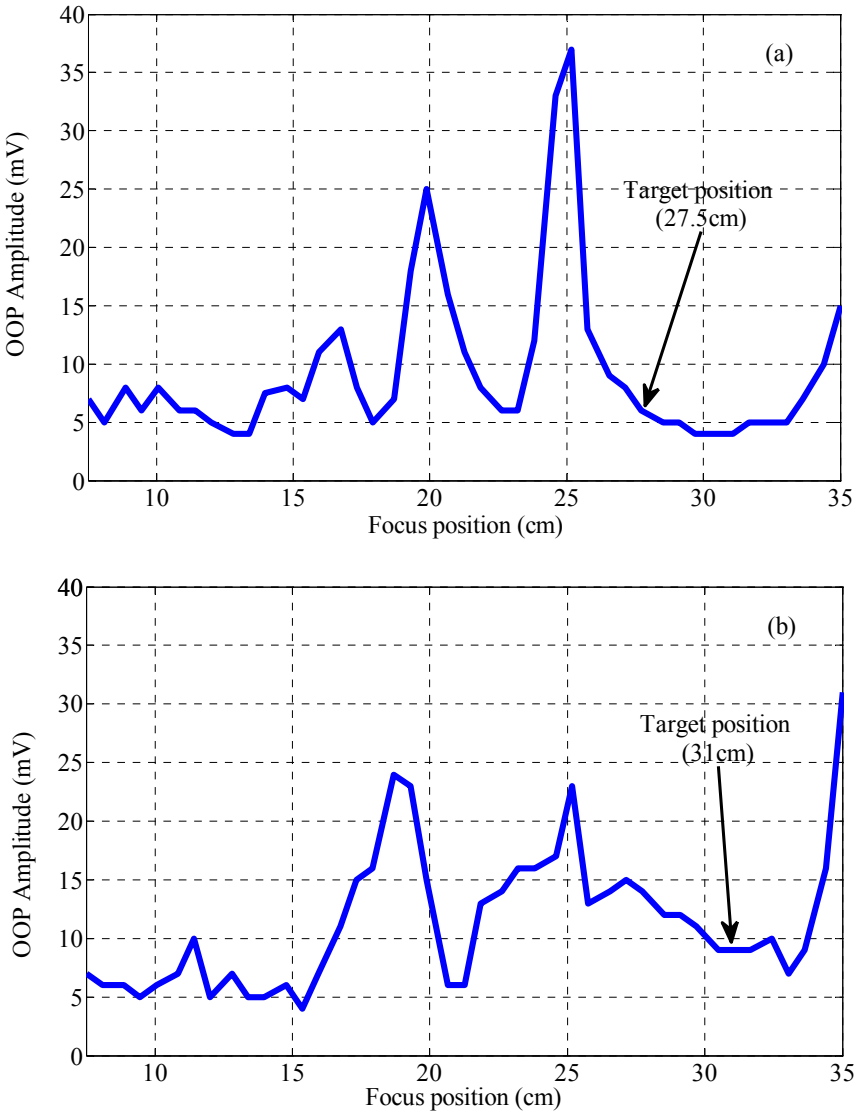

Figure 4.7. OOP amplitude versus position of the best image of the laser for (a) target position of 27.5cm and (b) target position of 31cm from the laser. Target displacement was sinusoidal with peak to peak amplitude of 5μm and the frequency of 100Hz.

When the signal goes below 10mV, it should be considered as severely faded by the noise floor, and thereby to detect the OOP signal becomes extremely difficult. In all experiments in this Section we have selected to keep the signal above 10mV to enable correct signal detection and reliable measurements. Adjusting the spot size on the target via the modification of the focal length of the optical system gives thus a very strong tool to have a signal with the proper SNR even when significant speckle effect is present.

4.b. Adaptive control of speckle effect

In this section, a real time control of the speckle effect using the AOH described in Section is presented. First, the working principle of the method and the experimental configuration will be described. Afterwards, since this solution is based on real time control of the spot size by changing the focal length of the lens, the signal quality during the spot size modification will be experimentally investigated to see if there are possible additional effects due to changes in spot size in the results of the measurements. Next, the adaptive algorithm used for the real time control of speckle effect will be explained in detail. Finally, the experimental results achieved by the proposed technique will be presented.

4.b.1. Working principle

As investigated in subsection 4.a.3, changing the spot size on the target may change the position of the fading region, modifying the speckle pattern imposed to the OOP. Thereby, our proposal is improving the OOP amplitude by changing the spot size to modify the speckle pattern when the OOP amplitude is reaching to the noise level due to speckle modulation.

This imposes the OOP amplitude to be monitored in real time to see if a spot size modification is needed. Since the noise of the signal may not be constant during the acquisition, we propose using the SNR value instead of the OOP amplitude as the gauge to detect signal fading and to control signal quality in a real-time control algorithm. As proposed in subsection 3.b.2, we will apply the method for calculation of SNR used in ECG signals [Gautam 2008].

Whence, we propose an automated adaptive control of the AOH presented in subsection 3.a.3 using real time data acquisition for checking the SNR of the OOP signal and evaluate the need for potential changes in spot size. The experimental configuration and the laboratory equipment arrangement with data acquisition scheme are presented in the following section.

4.b.2. Experimental configuration

The experimental configuration for real-time adaptive control of speckle effect is shown in Fig. 4.8. The LD is a Hitachi HL7851G single mode LD emitting at 793nm with a maximum power of 50mW.

The target is moved by a M-227.50 DC motorized piezo-actuator from Physik Instrumente (PI). The characteristics of the AOH used in the setup are described in section 3.a.3, where the LL is remotely controlled from a PC through a USB connection to the LL driver.

Figure 4.9 shows the arrangement of the laboratory equipment for the complete setup. In this setup, two different analog to digital converters (ADCs) are used. Two ADCs are required as relevant signal data for the measurement reconstruction might be lost while real-time SNR information is transferred to the computer for speckle control. One of the ADCs is a Picoscope 4227 (essentially a PC-connected compact oscilloscope) used to acquire the signal used as input in the control algorithm for real time SNR

calculations. A second ADC (a Tektronix DPO2024 oscilloscope) is used for data acquisition of the complete data series for displacement reconstruction along the target displacement.

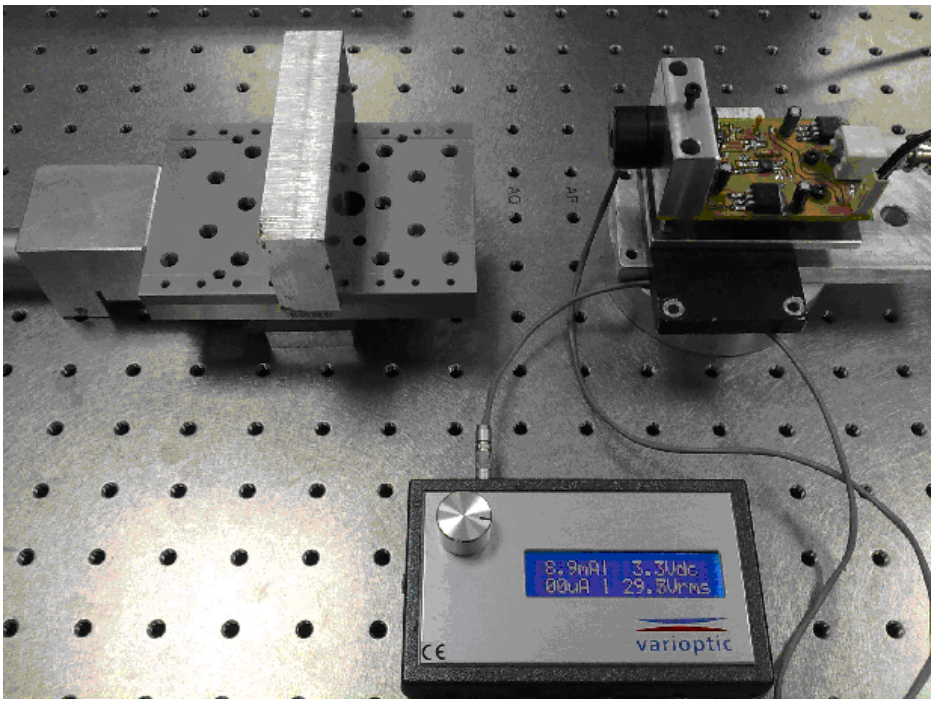

Figure 4.8. Experimental configuration of the adaptive control of speckle effect using AOH for large displacements.

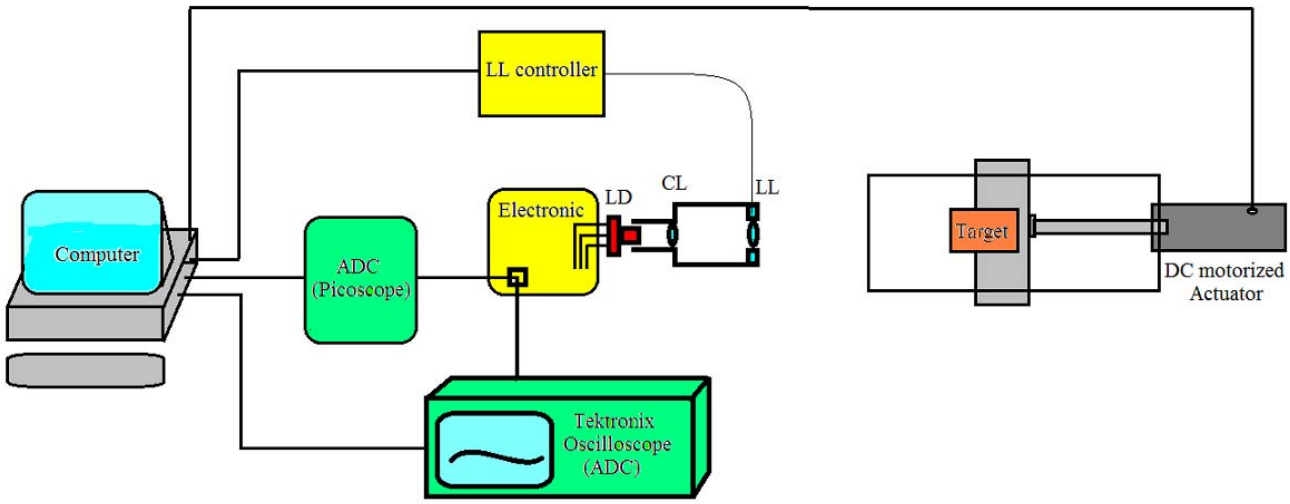

Figure 4.9. Arrangement of the laboratory equipment for the automated adaptive control of speckle.

The schematics for the management of ADC signal acquisition is depicted in Fig. 4.10. In practice the acquisition time (T_{acq}) and the time taken for signal transfer to the computer (T_{Tran}) set limits on the speed of the target, as far as the information on the signal needs to be acquired at such a speed that no relevant information for control is lost. In the presented acquisition scheme, during the unavoidable data transfer step of the Picoscope signal we lose control on it, and in the case of fast displacements we may have

fading regions not detected in the control algorithm while data is being transferred. In subsection 4.b.4, all related parameters to be optimized prior to the measurements to have a desirable control of the signal will be discussed in detail.

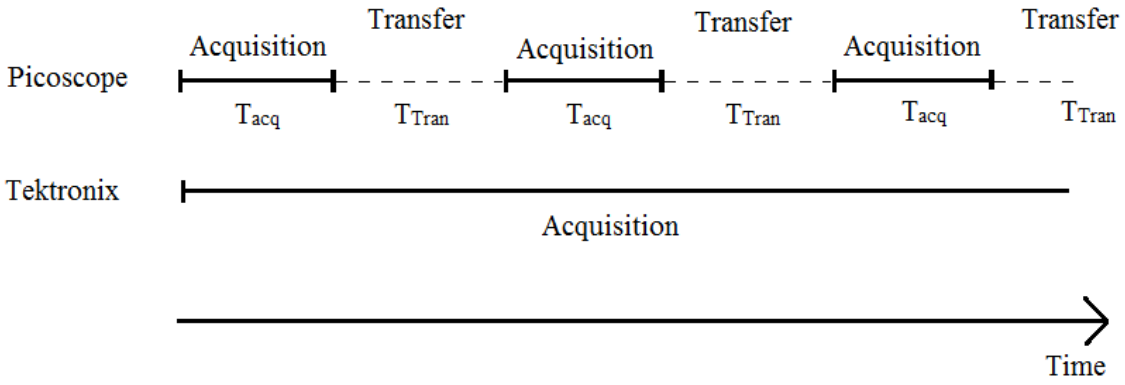

Figure 4.10. Signal acquisition scheme using Picoscope and Tektronix oscilloscope.

4.b.3. Analysis of the quality of the signal along the adjustment of spot size

As described in the working principle, the spot size will be adjusted along the target displacement in order to get the signal out of the fading region. It should be verified that this modification does not add any additional effects on the signal during the measurements.

The response time of the LL is the duration between two steady states of the lens power, when the driving voltage changes into a step function, varying from a V_{min} level to a V_{max} level. Based on this definition, the LL used in all measurements has a response time below 80ms for a voltage change of 0V to 60V.

In experimental data, the effects of the modification of the spot size on the signal can be easily observed in the acquired OOP, as shown in Fig. 4.11. In this example, the OOP amplitude is seen to be modified by a change in spot size in different time scales. A sudden change in spot size using the LL (introduced by a 1V change in the voltage of the LL) at the time of 38.03s in the experiment recovers the OOP amplitude and the SNR instantly, and after an unexpected oscillation which lasts around 200ms reaches the steady state. The fringes in the OOP were almost pure noise before spot size adjustment, while afterwards become again saw-tooth like and sharp enough for the classical detection algorithm. The SNR calculated for this case is shown in Fig. 4.12. The sampling rate used in the ADC was 12500 Samples/s, and 2000 samples were used to calculate the average value of SNR. The SNR value against time may be seen to steadily decrease due to the appearance of the fading zone. The oscillation which appears in the OOP may be seen not to have any significant additional effect on the SNR value and on fringe detection, except for the appearance of a small oscillation in the signal amplitude during the transient time required for the stabilization of the LL.

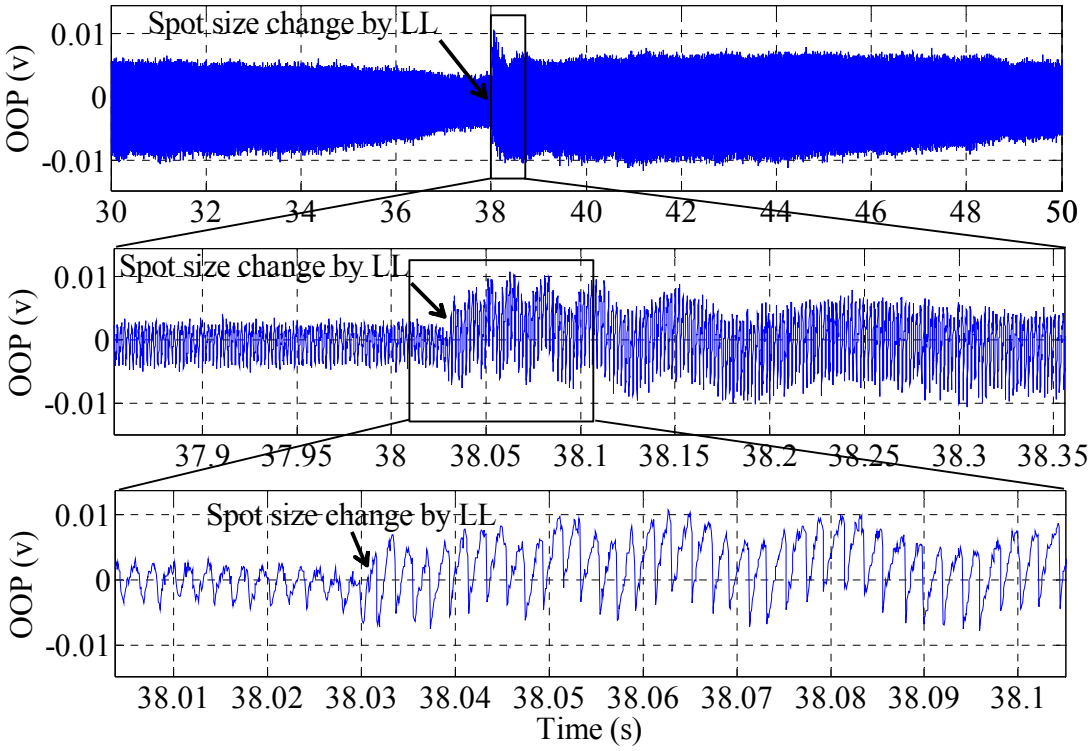

Figure 4.11. Experimental OOP acquired for a target velocity of 0.2mm/s. A sudden change of spot size by changing the focal length of the LL gets the signal out of the fading region. Different magnified time scales show the oscillation in the signal when spot size is adjusted, due to the stabilization of the LL.

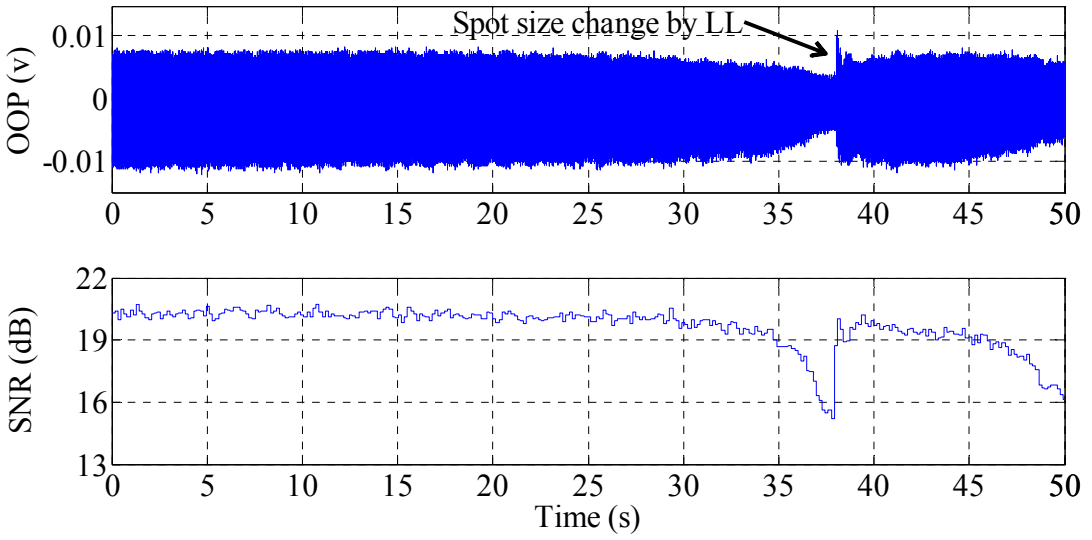

Figure 4.12. Experimental OOP acquired for a target velocity of 0.2mm/s. The sampling rate of the ADC was 12500 Samples/s and the No. of samples used to calculate the average SNR was 2000.

4.b.4. Algorithm for the adaptive control of speckle effect

The block diagram of the control algorithm is shown in Fig. 4.13. First, three parameters are initialized including the focal length of the LL (F_{LL}), the Fail parameter (Fail), defined as the number of times that

the control algorithm fails to get a reasonable SNR after a spot size adjustment, and N_f , defined as the number of focus changes introduced in the LL. The spot size is adjusted when SNR reaches a value below SNR_{thr}, or goes above SNR_{up}. SNR_{thr} is the minimum threshold value of the SNR in which the OOP starts to be faded by the noise, while SNR_{up} is the upper limit of the SNR value which indicates that the laser may start to be in the chaotic state.

Once the target starts to move, a sequence of OOP signals is acquired using the Picoscope, and the SNR of the sequence is calculated. If the SNR is between SNR_{thr} and SNR_{up}, the spot size is not modified. In this case the acquisition and SNR calculation is repeated to monitor the state of the measurement in the following step. As there is neither a spot size change nor a fail occurrence, the Fail and N_f parameters remain at zero.

When the SNR value goes below SNR_{thr} or above SNR_{up}, there are two options depending on the N_f. If N_f is smaller than N_m, defined as the maximum number of focus changes allowed to the system to get out of a fading region in a reasonable time, the focal length is changed to F_{LL} + dF to recover the SNR. N_f is then increased by adding one to its previous value. The value of N_m is fixed depending both on the target velocity and the LL focus range and response time, and needs to be optimized for each experimental condition.

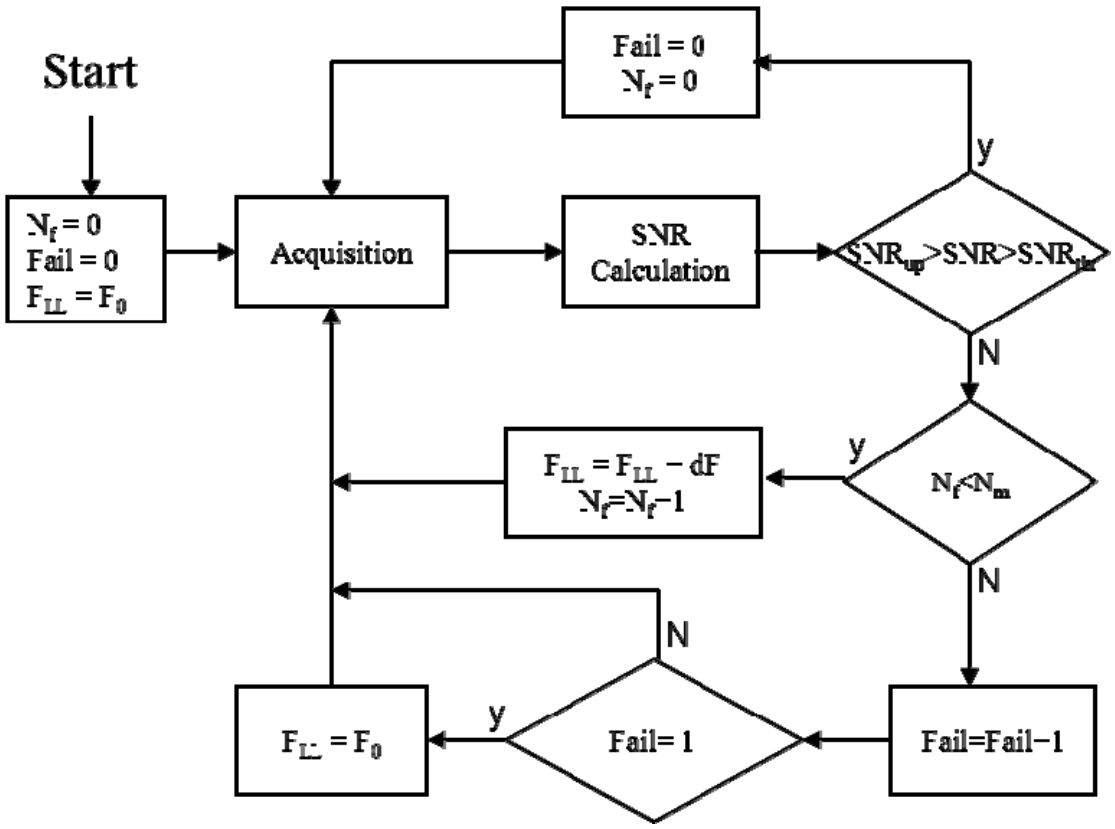

Figure 4.13. Block diagram of the control algorithm.

Afterwards, signal acquisition and SNR calculations continue to see if the spot size change was effective to increase the SNR of the signal or not. If the SNR is still below SNR_{thr} or above SNR_{up} the focus change

is repeated till recovering the OOP or reaching to the maximum number of focus changes allowed. In the event of reaching the maximum number of focus changes without recovering the faded signal, the control algorithm has failed to keep the signal within thresholds, and the Fail parameter is subsequently increased. In this event (which did never appear in our experiments) the focal length is changed to the initial condition ($F_{LL} = F_0$) and the signal acquisition with SNR calculation is continued although there will be data acquired with too low SNR, so a reliable displacement reconstruction cannot be ensured.

Obviously, some parameters in the adaptive speckle control algorithm should be optimized prior to the measurement to have the algorithm in optimal conditions. Those parameters includes SNR_{thr}, SNR_{up}, N_m, dF (LL focal length change), based on the conditions of the experimental setup, and the data acquisition time (T_{acq}), related to the velocity of the target being measured.

4.b.5. Experimental Results

The experimental configuration described in subsection 4.b.2 is implemented together with the control algorithm described in subsection 4.b.3, which has been implemented under a Visual C++ environment. The total target displacement was set to 20mm, T_{acq} was set to 40ms, N_m was 5, dF was adjusted to 1cm, SNR_{up} was 25dB and SNR_{thr} was 14.5dB. These parameters have been optimized for target velocity of 0.2mm/s.

Figure 4.14 shows two OOP signals acquired using the setup. The upper one shows the OOP obtained in a fixed focus condition, while the middle one shows the adaptive speckle control technique we have described. The bottom plot describes the comparison of the SNR of both signals. It may be seen how the SNR of the signal obtained using the adaptive speckle control technique has been kept between the SNR_{thr} and SNR_{up} during the complete measurement, while the SNR of the fixed focal setup went below SNR_{thr} in three different regions. It may be seen how the control algorithm has improved the SNR of the signal by adjusting the spot size before the SNR went under the threshold level.

Reconstructions of displacement out of the obtained signals have been illustrated in Fig. 4.15, showing a successful reconstruction of the signal affected by the speckle when spot size adjustment using the AOH is implemented. To reconstruct the signal, the FCM algorithm described in subsection 2.d.2.1 was applied. Differently, the fixed focal approach is unable to cope with signal losses in the fading regions and incurs in important inaccuracies. In our experiments, the speckle phase error has not been eliminated. Even in the worst case this phase deviation accounts for a displacement error in the order of a few microns in the reconstructed displacement. In the results obtained using the proposed solution, no speckle phase error was larger than the measurement resolution ($\lambda/2$) while the total displacement was over 2.5×10^4 λ. Furthermore, this error could be significantly reduced, if required, by increasing the target distance as described in section 2.e.

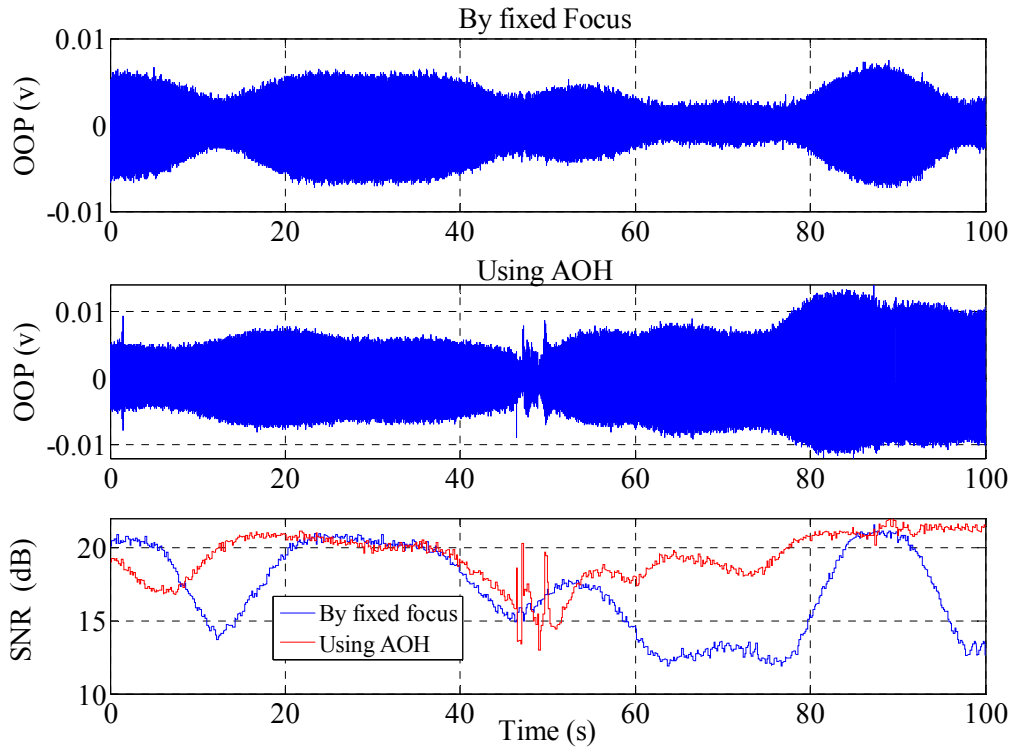

Figure 4.14. Results obtained by fixed focus and by using adaptive control of speckle effect algorithm.

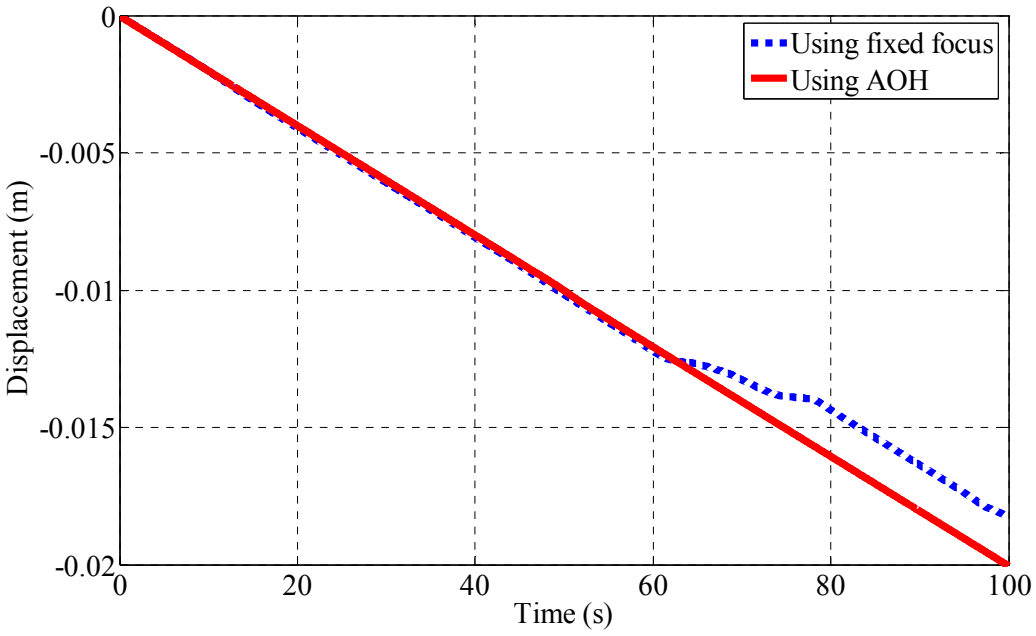

Figure 4.15. Displacement reconstruction of two acquired signals for a metallic target displacement of 20mm using a fixed focus lens and the adaptive speckle control algorithm. The difference is about 1.760mm (%8.8) in a total displacement of 20mm.

The total error in the reconstruction using a fixed focus lens was about 1.760mm, corresponding to 8.8% of the total target displacement. This error is in good agreement with the displacement measurement error due to the speckle effect estimated in the literature (10% of the total displacement range) [Donati 2004].

Results show the feasibility of the adaptive control of speckle effect in the described experiment, where the signal could be satisfactorily measured in the whole displacement range.

In order to further investigate on the effectiveness of the technique, velocity measurements using OFI were carried out in the same experiment. As well as for displacements, the amplitude modulation introduced by the speckle effect in the fading zones decreases the accuracy of the measurement of the velocity of the target [Lu 2010]. Subsequently, the described adaptive speckle control technique should also be effective in improving the accuracy of velocity measurements in the whole displacement range.

Figure 4.16 shows the measured velocity of the target during the complete displacement of 20mm. The measured OOP corresponds to the one presented in Fig. 4.14. The velocity of the piezoelectric motor used in the experiment was set to 0.2mm/s. Velocity is related to Doppler frequency by equation (2.3), which is calculated by applying an FFT algorithm to the OOP, and selecting the Doppler frequency which corresponds to the maximum magnitude [Scalise 2004]. To find the Doppler frequency in the whole acquired signal, the FFT is performed a number of times in the certain number of parts of the acquired signal. For this, a moving window with a certain length and a given movement resolution has been considered. For the results demonstrated in Fig. 4.16, the length of the window for FFT calculation was set to 5000 data points, with a resolution of 1000 points, over a data set of 1.25 10^5 points. After applying the FFT, a band-pass filter was also applied to the signal to remove the noise.

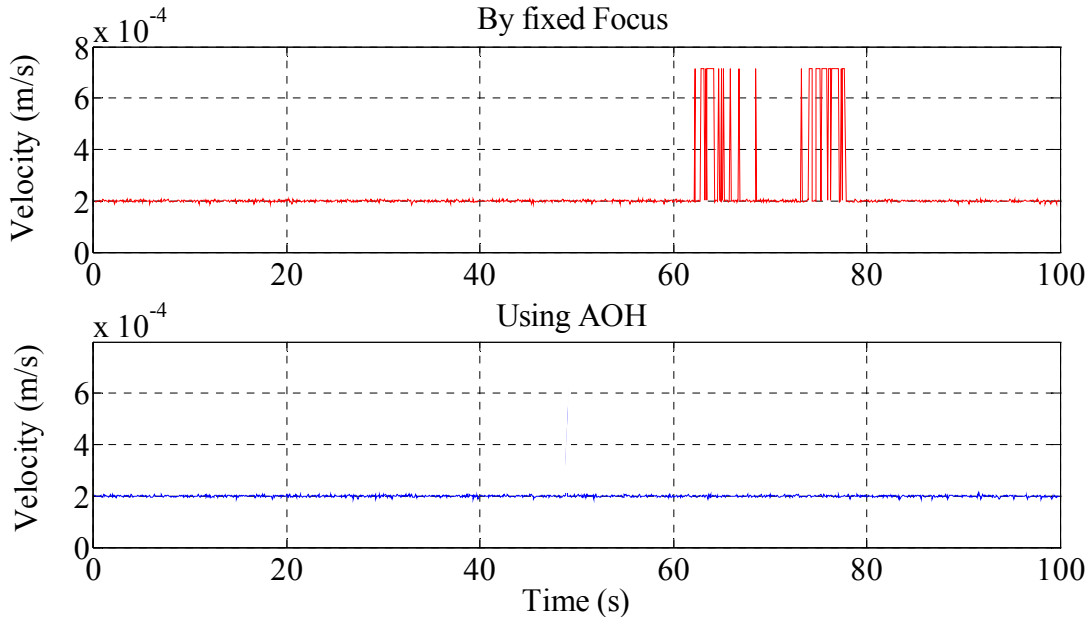

Figure 4.16. Target velocity measured using a fixed focus lens (above) and adaptive speckle control (bottom). Target was moving at a constant speed of 0.2mm/s.

As seen in Fig. 4.16, some errors in the velocity measurements are introduced in the measurements in the fixed focus case, due to wrong determination of the Doppler frequency due to poor SNR. Measurements performed using the AOH obtain the correct velocity value at all distances from the target. Figure 4.17 shows the FFT of the signal at an error point where the SNR of the OOP was below SNR_{thr}, so the

magnitude of the Doppler frequency related to the target velocity is smaller than noise frequencies, leading to a wrong determination of the Doppler frequency value. In difference, Fig. 4.18 shows the FFT of the signal at a point with high SNR, where the magnitude of the Doppler frequency related to the target velocity is much larger than noise, so the Doppler frequency is found without doubts.

Therefore, using adaptive speckle control improves also the accuracy of velocity measurements in OFI for large displacements, whenever speckle effects are relevant.

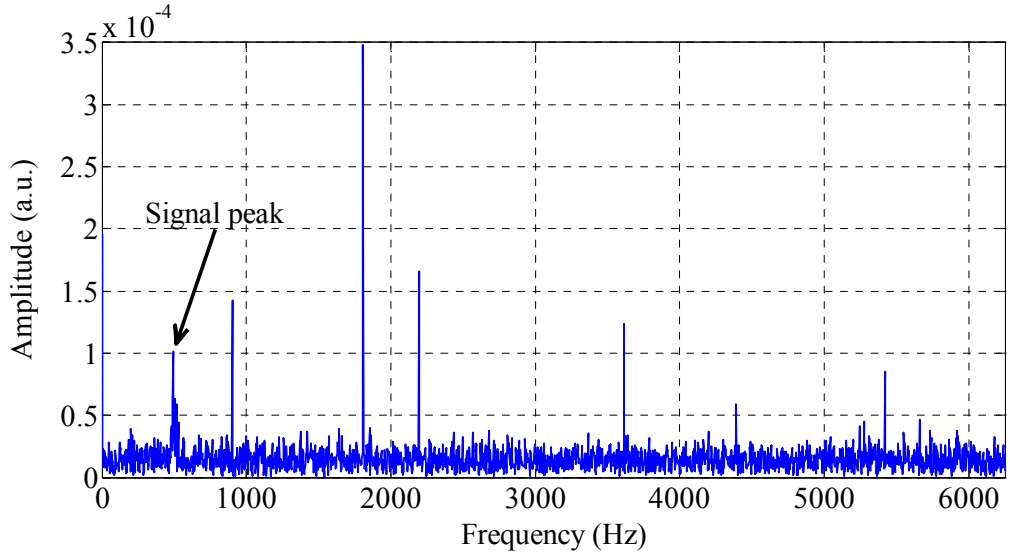

Figure 4.17. FFT of an OOP signal sequence with low SNR where the Doppler frequency peak is smaller than noise-related peaks, leading to errors in the determination of velocity.

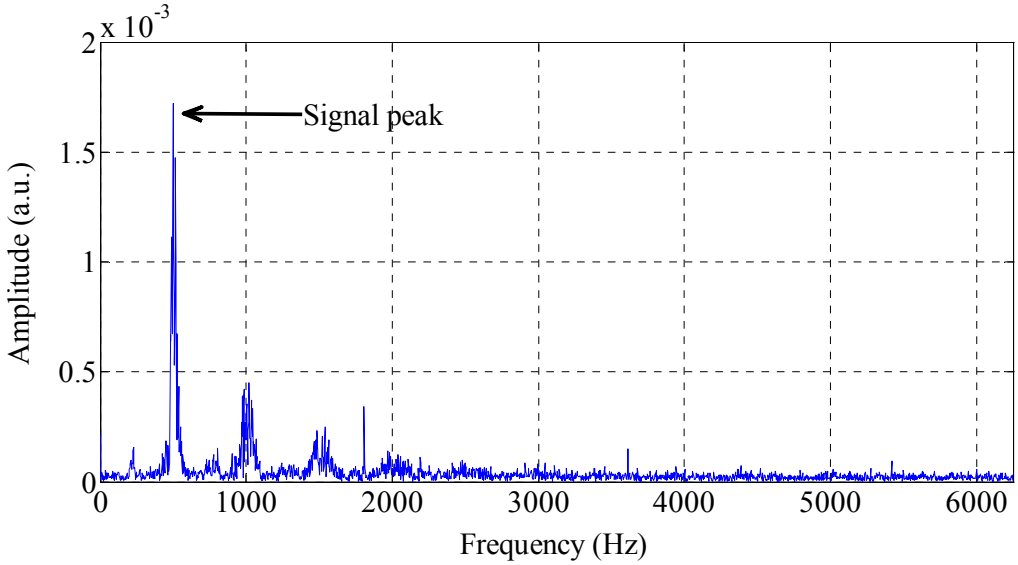

Figure 4.18. FFT of an OOP signal sequence with high SNR where the Doppler frequency peak is larger than the noise peaks, so velocity can be properly determined.

4.c. Non-adaptive speckle control (sensor diversity)

4.c.1. Working principle

Our second proposal for managing speckle effects involves two different LD pointing to the same target. Both LD are chosen so they present different speckle patterns (due to i.e. wavelength, spot size, or coupling coefficient differences, or a mix of them), so the combination of both signals results in a lower probability of signal fading than when using one single LD. This strategy, known as diversity, has been successfully applied in radio communication to deal with the fading effect [Raisanen 2003]. The technique has been developed in the forms of spatial, spectral and temporal diversity. Similar to spatial and spectral diversities in radio engineering, we are proposing spatial diversity in the form of two LD pointing at different points of the target with different spot sizes, together with spectral diversity using two LD with different wavelengths. So we will have spatial and spectral diversities simultaneously. If we consider the probability of fading in the signal as the length in time of the faded signal related to the whole acquired signal sequence, then the probability δ of fading the signals of two LDs is $\delta_1 \times \delta_2$, where δ_1 is the error probability in the signal of the first LD and δ_2 is the error probability in the signal of the second. As far as the error probabilities of fading in both signals are relatively small, the error probability δ is significantly lower than the error probability in each individual LD signal, although not necessarily zero. Thus, what is expected is to avoid simultaneous signal fading in both signals.

Figure 4.19 shows the experimental OOP acquired using two LD pointing at two different positions of the target, for a target displacement of 40mm using two LDs with different spot size. The concept is of course using the other signal as an alternative when signal fading occurs in one of them.

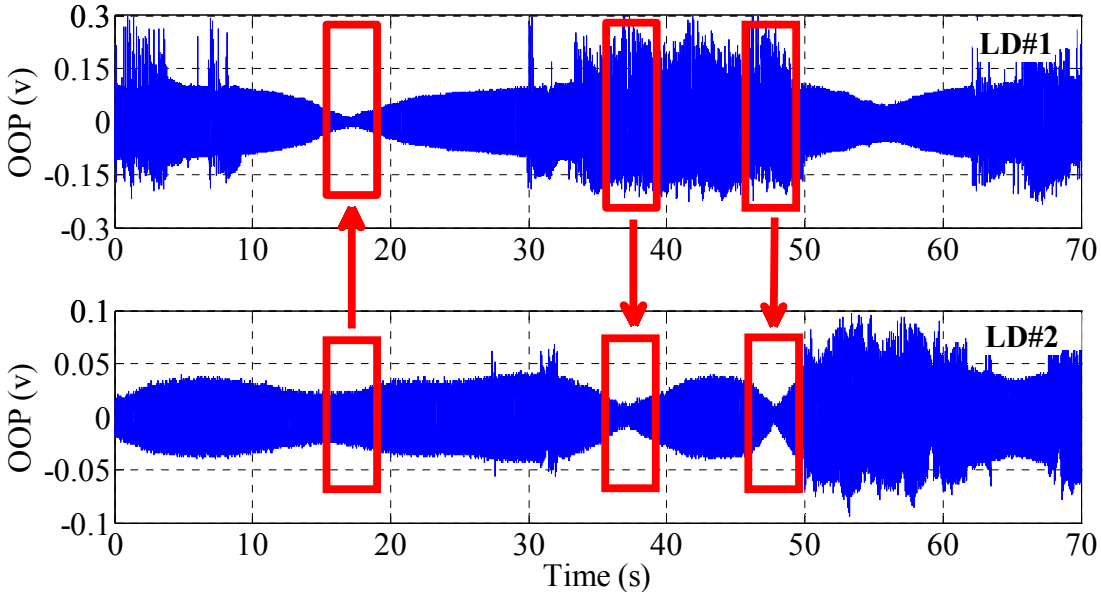

Figure 4.19. OOP signals acquired by two LD with different focus positions (different spot size) pointing to the same target. Target displacement was 40mm.

Thus, the faded signals shown in selected windows in Fig. 4.19 are replaced with data from the alternative signal for displacement reconstruction purposes.

4.c.2. Measurement algorithm

The algorithm proposed for this approach is shown in Fig. 4.20. Since the detection of poor SNR in the OOP signal has been shown to lead to unreliable reconstruction, the SNR value will be used again as control metric.

Afterwards, reconstruction is performed for each channel using the FCM algorithm described in subsection 2.d.2.1. Later, a decision block selects which signal reconstruction is more reliable based on the value of SNR of both signals. The reconstruction of the signal with higher SNR is considered the most accurate. In the offline application of this method, there is no significant limit on the target displacement velocity, setting a difference with the adaptive speckle method presented in Section 4.c.

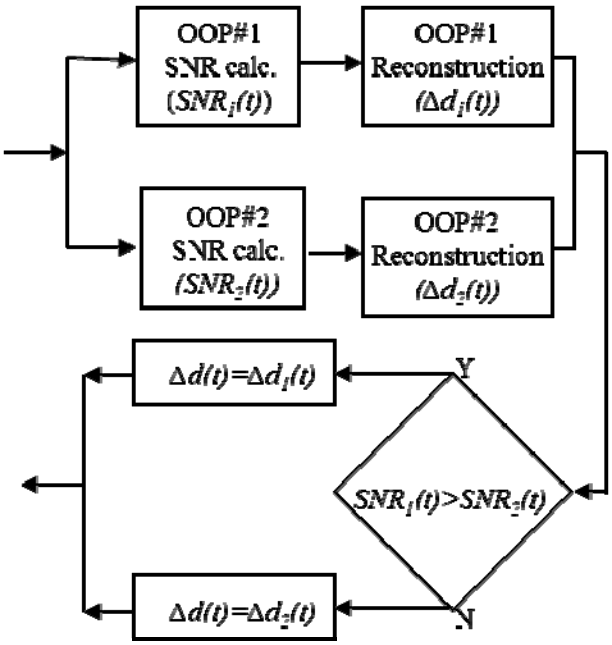

Figure 4.20. Block diagram of the algorithm applied for reconstruction in the sensor diversity technique.

4.c.3. Experimental results

As an experimental demonstration of the technique, two laser sources with different wavelengths pointing to different positions on the target, as shown in Fig. 4.21, are used. One of the lasers is a Hitachi HL7851G single mode LD emitting at 793nm with a maximum output power of 50mW and the other laser source is a VCT-F85A32-IS-V2 VCSEL emitting at 843nm with a maximum output power of 2mW. The target is a metallic surface mounted on a M-227.50 DC motorized piezo-actuator from PI. It was moved along 20mm with a fixed speed of 0.55mm/s. The initial target distance from the lasers was 20cm. The average FWHM of the LD spot on the target was 78µm and the average FWHM of the VCSEL spot was 62µm. Thus, the solution involves both spectral and spatial diversities.

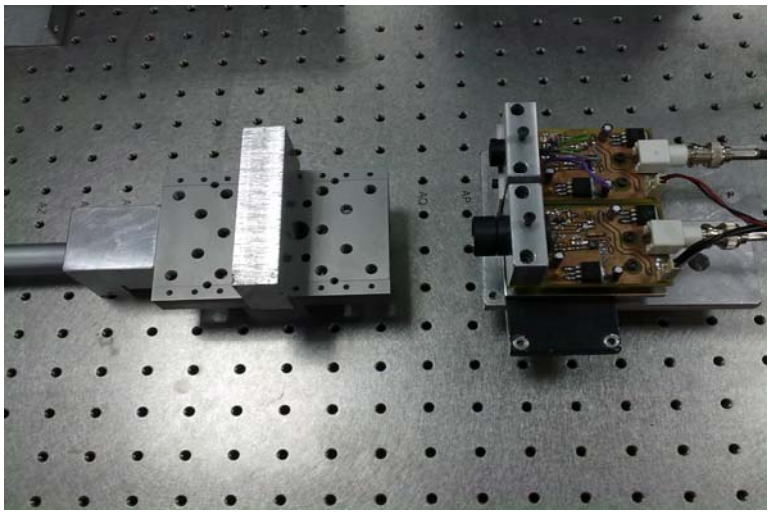

Figure 4.21. Experimental setup for sensor diversity demonstration.

Figure 4.22 shows the experimental OOP acquired from both lasers. By applying the decision algorithm described in Fig. 4.22, the reconstructed displacement is shown in Fig. 4.23. It may be seen how the reconstructed displacement obtained from the OOP of the LD had a 15.5% error, while the reconstructed displacement from the OOP of the VCSEL has a 10.6% total error along the complete displacement range due to problems due to speckle. According to equation (2.37), the expected speckle phase error for both signals was about 3.1μm, considering the lens optical aperture of 5mm, and has not been taken into account. Using the proposed diversity strategy, the displacement was reconstructed with no amplitude fading error in the whole displacement range, within the half-wavelength resolution imposed by the FCM algorithm used.

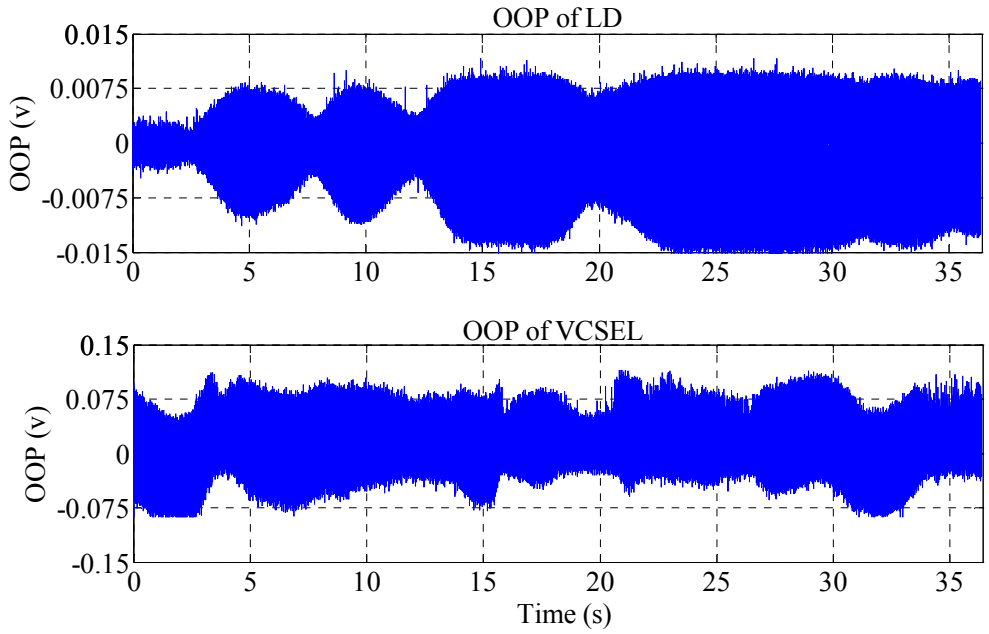

Figure 4.22. OOP acquired from single mode LD and the VCSEL for the same target displacement of 2cm with the speed of 0.55mm/s.

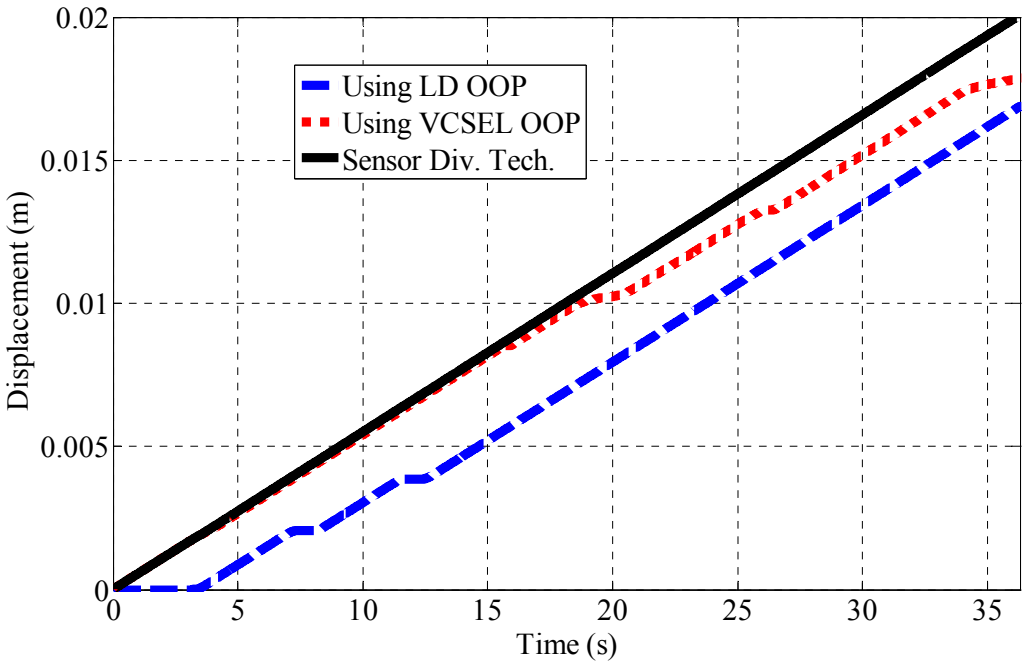

Figure 4.23. Reconstruction results for the signals of LD and the VCSEL and by using the sensor diversity technique.

4.d. Conclusion

In this chapter, a detailed analysis of the amplitude fading effect induced by speckle effect in the OOP signal of OFI interferometers has been presented. We have shown for the first time that the coupling factor coefficient in OOP changes in fading regions due to the presence of speckle, yielding larger *C* values, suggesting large hysteresis and fringe loss situations in the signal in those areas. This adds on to already complex reconstructions due to the small amplitude of the OOP signal. We have also shown how the modulation frequency of the speckle affected OOP signal depends on the average roughness parameter R_a, presenting how the number of local maxima present in a 40mm displacement decreases when increasing R_a from 0.05µm to 0.4µm, while from 0.4µm to 1.6µm the number of maxima remains constant. Moreover, we have shown that changes in the spot size may modify the positions of both the maxima and the fading regions in the speckle affected OOP signal.

Then, two new methods and a classical procedure have been proposed to improve measurements in OOP signals having a speckle affected OOP. One of the methods uses the AOH described in the previous chapter to implement an adaptive speckle control solution, which changes the spot size on the target by changing the focal length of the lens, so modifying the position of the fading region. The proposed method cannot be used at large speeds as there are some experimental conditions (data transfer in the control algorithm, the delay in the feedback loop and the response time of the liquid lens) which cause it to have a slow time response. Experimental results for velocities of 0.2mm/s have however been shown

and successful displacement and velocity measurements shown using the adaptive solution proposed, and compared to conventional approaches.

For larger speeds, we have presented a second approach in the shape of a sensor diversity technique which uses two lasers spatially and spectrally diverse to combine their two different OOP which present different fading zones. An SNR-based algorithm has been used to select the optimal signal of the two available ones to be used for displacement reconstruction. Experimental results in both methods show successful management of OOP fading regions for centimetric displacements of a metallic target. The existent speckle phase error has not been considered, as it introduces a displacement error of only a few microns, and in addition can be significantly reduced by increasing the target distance.

5. Industrial applications

In this chapter, we will present two new industrial applications of OFI where the speckle effect appears in the measurements and significantly decreases the measurement accuracy. The applications will show that OFI sensors can very satisfactorily perform as non-contact proximity probes in industrial environments, although the attainable resolution will be often limited by the environmental limitations of the application. One of the applications is the measurement of the trajectory of motor shaft runout in electric motors, where displacements in the 50-100 micron range are normally produced in faulty motors. The second application is the measurement of the deformation of polymer-reinforced beams under dynamic loading conditions, a case in which the displacements can reach some centimeters.

As commented in Chapter 4, the literature assumes that for displacements around 0.1mm, like those of the motor shaft application, we may start to have speckle-affected signals. This means we could have one or a few amplitude fading zones in the OOP signal, depending on the wavelength, target distance, and the diameter of the lens used for focusing (equation (2.37)). Increasing the displacement of the target increases also the number of amplitude fading regions. Under this limited speckle problem, with a small number of fading regions in the signal, an optimized working condition can be found using the classical procedure of adjusting the spot size by modifying the position of the fixed focus lens while looking at the obtained signal. Alternatively, such adjustment of spot size can be done using the AOH previously described in Chapter 3, and adjusting the focal length of the liquid lens.

Both concepts optimize the position of the speckle fading regions regarding the particular experimental condition found. This procedure can be used to deal with one or two fading zone(s) along the displacement, although not for complete elimination of the speckle effect. We have applied this procedure to deal with speckle effect in the motor shaft runout tracking presented in the following section. Using this procedure resulted in the successful elimination of the speckle effect, and in the measurements described in detail in section 5.a.

The second application, presented in section 5.b, involved the monitoring of beam deformations under dynamic loading, with possible displacements of a few centimeters. Here, the adaptive speckle control solution proposed should be in principle the best solution, as the monitoring involves a slow deformation of the beam. However, due to the reflectivity characteristics of the beam used in the setup only one fading region appeared in the signal across the whole displacement range, so an equivalent focus adjustment technique to that used for the motor shaft runout application was used. It should be noticed, however, that in displacements of this size it is normal to have a larger number of fading regions where simple spot size adjustment would not suffice to manage the speckle effect problem. We will close the chapter with a brief conclusion in section 5.c.

The original developments of this Chapter have enabled a number of publications, including a patent [Royo 2011], two journal papers [Atashkhooei 2013b] [Urresty 2013] related to the motor shaft runout tracking application, and a conference paper [Atashkhooei 2012] related to the measurements of beam deformation under dynamic loading.

5.a. Motor shaft runout tracking

5.a.1. Introduction

Permanent magnet synchronous motors (PMSMs) have been applied in a large number of applications such as servo actuators, robotics, aerospace technology, automobiles, and electric traction systems [Rajagopalan 2007]. Generally, electric motors operate through the interaction between an electric motor's magnetic field and winding currents to generate force within the motor. In a PMSM (Fig. 5.1), which uses sinusoidally distributed stator windings, permanent magnets create the magnetic field.

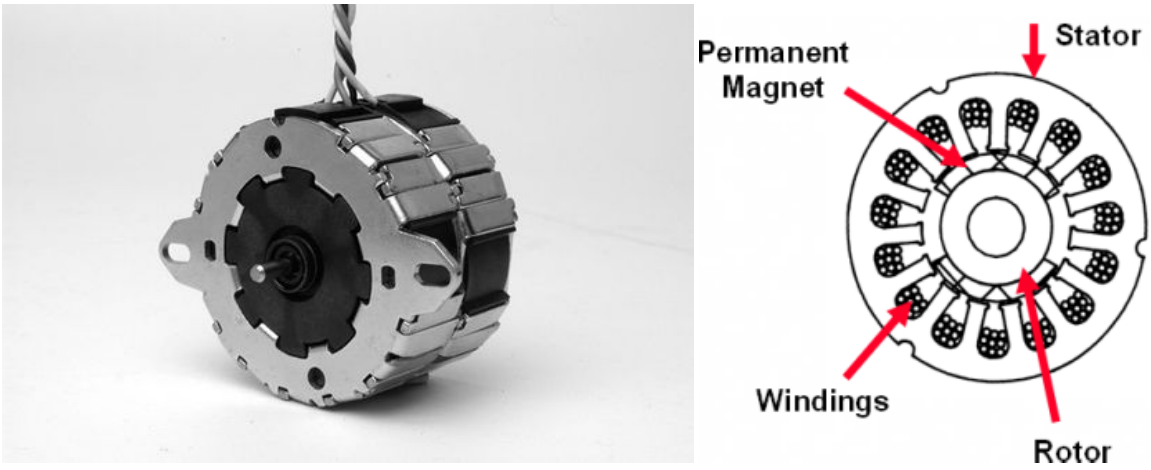

Figure 5.1. A typical PMSM motor (left) and its schematic diagram(right).

PMSMs are becoming increasingly popular in high performance applications, raising attention towards the corresponding condition monitoring and fault detection procedures. The major sources of failures in PMSMs are demagnetization, jointly with bearing and rotor eccentricity faults which may be classified into static, dynamic or mixed eccentricity [Hong 2012]. Static and dynamic misalignment of the motor shaft is a common origin of maintenance problems in PMSMs, in particular mechanical seal failure. These problems become manifested as shaft runout, that is, wobble-like movements inducing lateral displacements of the axis of the motor. Such displacements may measure from a few microns to some millimetres, depending on the type of fault which causes them.

Several types of displacement or vibration sensors may be used as proximity probes to measure the shaft runout. The main families of sensors are eddy current probes [DeBlock 2007], capacitive probes [Lin 1997], LVDT probes [Chass 1970] and LDV sensors [Shieh 2001].

Eddy current methods are practical, but the presence of metallurgical irregularities in the shaft can add high levels of noise in the results of the measurements, with the corresponding loss of accuracy [Lin 1997]. Capacitive sensors are not limited by such an issue, but they need to be placed fairly close to the shaft (typically at distances of a few millimetres), which may not be practical for given in-situ measurements. LVDT probes are contact methods limited in its sensing speed by the inertia of the moving tip, which in addition is subject to wear and warm up, and to damage by surface irregularities. As a non-contact technique operative at a distance from the shaft, LDV avoids all these inconveniences, but it may suffer from speckle noise and is a quite expensive equipment, typically several thousands of Euros [Halkon 2006].

We are proposing an OFI sensor as a particular arrangement of laser vibrometry specially suited to harsh measurement conditions. OFI has been studied in depth in the last decades and shown to perform nicely as a non-invasive sensor for displacement, vibration, distance and velocity measurements, as discussed in section 2.a. The compactness, simplicity and cost-effectiveness of the sensor, together with its non-contact nature, make it a very suitable solution to track runout in electric motors, with measurement accuracies below $\lambda/2$, with λ being the wavelength of the laser.

However, a complete measurement procedure needs be developed to account for the several different situations appearing in real-world motor testing. As a first issue, signal fading due to the speckle phenomenon can affect the measurement accuracies. One or two fading regions may appear in the signal in each turn. Therefore the classical refocusing procedure used to optimize the OOP signal through changes in spot size proposed at the beginning of this chapter will be used, as a simplified version of the technique presented in section 4.b.

The complete measurement methodology has been developed and will be described in detail. We will first present some considerations on the measurement principle, the adjustments made on the setup, and the procedure for estimation of the uncertainty due to the surface imperfections in the motor shaft and misalignments of the laser relative to the centre of the shaft. Experimental results of the OFI sensor for runout measurement will be validated by comparison with the results of a commercial LDV. Finally, measurement results for two-dimensional (2D) runout tracking in a PMSM are presented both for a healthy and a faulty motor, showing the potential of the technique for non-destructive motor testing purposes.

This work was developed in collaboration with the research group Motion Control and Industrial Electronics, from the Terrassa Campus, which contributed their experience in PMSM motor control and

modelling, while from CD6 (Centre for Sensors, Instruments, and systems development, UPC) we contributed with our experience in OFI, signal processing and non-contact metrology.

5.a.2. Discussion on measurement principle

Some considerations should be taken into account to design the measurement strategy related to the constraints introduced by the application. Due to the experimental conditions of the system being measured (where the shaft will present mechanical roughness and irregularities well above $\lambda/2$), the basic resolution of the OFI sensor using FCM is far below the uncertainty of the measurements (see section 5.a.4 for further details).

Furthermore, displacements to be analysed are in the frontier between the "small" (not speckled) and "large" (highly speckled) displacements, which is typically set at amplitudes around 100μm. This means speckle effects may appear in the signal, and also that FCM will be enough as phase reconstruction algorithm as accuracies below $\lambda/2$ would be hidden by uncertainties introduced by the measurement conditions in the setup.

In addition, in practical applications under industrial conditions, environmental conditions may be very relevant. A number of parasitic phenomena are typically present in those conditions, especially when large motors are involved. These phenomena include mechanical coupling, electromagnetic disturbances, or surface imperfections of the target, among others. These phenomena introduce different types of noise into the OOP of the LD, typically as white-like noise or sparkle-like noise out of electromagnetic or mechanical sources in the environment. In addition, as commented throughout this chapter, using a laser source may introduce speckle noise.

As described in section 2.d, some signal pre-processing solutions have been proposed to efficiently remove the white-like and sparkle-like noises and improve the SNR such as a low-pass averaging filter, a Kaiser based FIR filter after a median filter, adaptive digital filters [Caum 2012] or neural network interpolation. For our purposes, a simple low-pass averaging filter was enough to remove the high-frequency component of noise present in the signal (see section 5.a.3 for more details).

A number of solutions have been proposed in this Thesis to overcome the speckle noise problem. No real-time adaptive compensation of spot size is justified in this case, as the conditions influencing the appearance of speckle are stable along each experiment. In addition, the shaft is moving at high speeds but the measurements need be taken in a single point, and adjusted in perpendicular to the symmetry axis of the shaft, which discards the spatial sensor diversity proposal, as the two lasers would be pointing to different points on the shaft and we intend to monitor the vibration at a single point.

Under small displacements, the optimization of spot size by changing focal length typically permits to get regions without fading zones large enough, so displacements of tenths of microns without significant

fading regions will be possible for each case. This adjustment can be performed either by voltage changes in the AOH or by adjustments of the position of the lens.

Thereby, the spot size of the laser on the shaft will be adjusted (manually or using the AOH) prior to each measurement, in order to experimentally minimize the amplitude of the speckle noise and reduce the presence of fading zones.

5.a.3. Measurement procedure

Since the shaft displacement is the measurement subject, the LD has been arranged to point in perpendicular to the shaft centreline using a conventional focusing lens (FL), as depicted in Fig. 5.2.

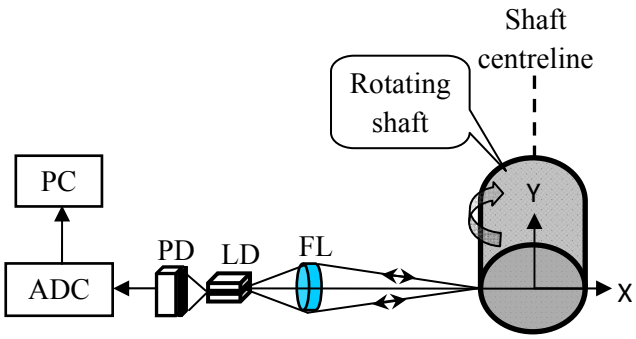

Figure 5.2. Schematic diagram of the experimental configuration.

Changes in optical path will be introduced by the lateral displacement of the shaft, whose component along the beam will be directly measured using the OOP. The OOP monitored by the photodiode (PD) integrated in the laser package is saved in the PC after an analogue-to-digital conversion. The vibration of the shaft in the laser beam direction (X axis in Fig. 5.2) is measured by offline signal processing. All measurements were performed using a Hitachi HL7851G single mode LD emitting at 793nm with a maximum output power of 50mW.

The motor used for the tests was a PMSM with reference No. ABB:8C1360, maximum power of 2.5kW and maximum rotation frequency of 33.3Hz. In the measurements, rotation frequencies were set to 12.5Hz and 25Hz, to test the motor in typical operating conditions.

Due to the system configuration speckle noise resulting in broad-scale OOP amplitude modulation was observed if no adjustment was performed. Figure 5.3 shows the acquired OOP generated by the displacement of a typical PMSM shaft after four complete turns. It may be observed how the acquired OOP includes one periodic fading region at each rotation (marked with dashed circles), where the signal amplitude reaches the noise level, leading to poor SNR and inaccurate reconstruction.

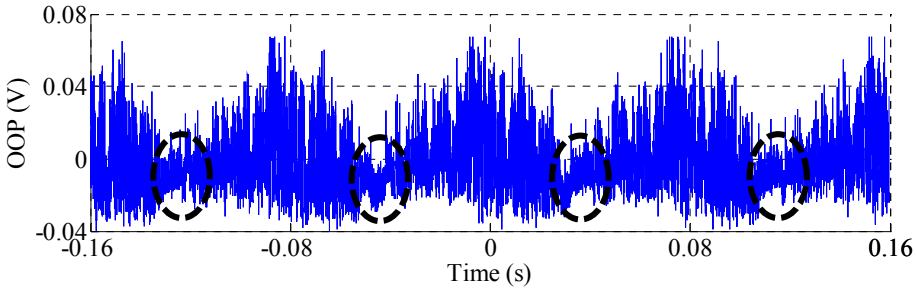

Figure 5.3. Speckle affected OOP generated by rotating shaft displacement. Four rotations at 12.5Hz are plotted.

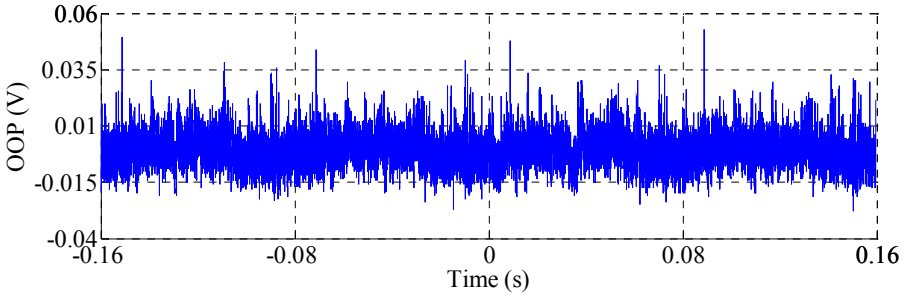

Figure 5.4. OOP generated by rotating shaft displacement after spot size adjustment. Four rotations at the frequency of 12.5Hz.

The speckle pattern has been modified by adjusting the laser spot size on the shaft, changing the beam focus along the optical axis by mechanical adjustment of the FL position prior to the measurement. This has enabled to keep the OOP amplitude above the threshold of signal loss along the whole acquisition period, and to get the minimum modulation frequency. Obviously, during the shaft rotation, the speckle pattern is almost repeated for each rotation as seen in Fig. 5.3.

By changing the focus position and observing the signal at the oscilloscope screen in real time, the best focus position to get minimally modulated signal amplitude is easily found. An automated focus adjustment algorithm based on stability of SNR, comparable to the one presented in section 4.b.4 would enable autonomous performance of the sensor using the AOH. Using this spot adjustment procedure prior to the measurement leads to adequate SNR values in the whole signal, and to the removal of the amplitude fading effect introduced by speckle modulation. Figure 5.4 shows the acquired OOP once spot size has been optimized, with no fading regions present.

The whole signal processing schema for displacement reconstruction out of the OOP obtained is presented in Fig. 5.5 as a flow diagram, showing the four main processing steps involved. As a first step, a low-pass Butterworth type filter is applied to the OOP to clean it from unwanted high-frequency noise. The cut-off frequency of the filter was set to 15% of the sampling frequency.

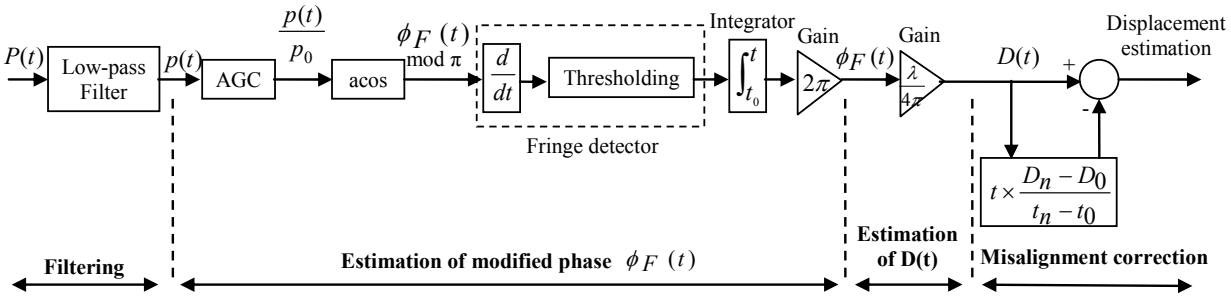

Figure 5.5.Flow diagram of the signal processing procedures for the estimation of displacement, including misalignment correction.

In the second step, the modified signal phase $\Phi_F(t)$ is roughly estimated in a procedure similar to that presented in section 2.d.2.3 for the rough estimation of the phase of the signal. In this step, since the modified phase is related to the OOP by equation (2.30), an AGC algorithm normalizes the signal to ±1, and the arcos function is applied to obtain the value of $\Phi_F(t)$ modulus π. Afterwards, to properly unwrap the phase, the derivative of $\Phi_F(t)$ is calculated and thresholded to detect the position of the fringes, and normalized to ±1. An integrator algorithm adds or subtracts the phase jumps (≈ 2π) at the detected fringe positions. Finally, the value of displacement related to the phase $\Phi_F(t)$ by equation (2.28) can be obtained by multiplying $\lambda/4\pi$ to $\Phi_F(t)$. Half-wavelength accuracy is thus expected for the measurements from the measurement procedure.

An additional compensation algorithm is then required in the current application to account for the misalignment error introduced if the LD is not pointing in perpendicular to the shaft surface. In case this misalignment error is present, virtual displacements of the shaft will appear in the reconstructed signal, caused by the component of the velocity of the surface in the direction of the beam (see Fig. 5.6).

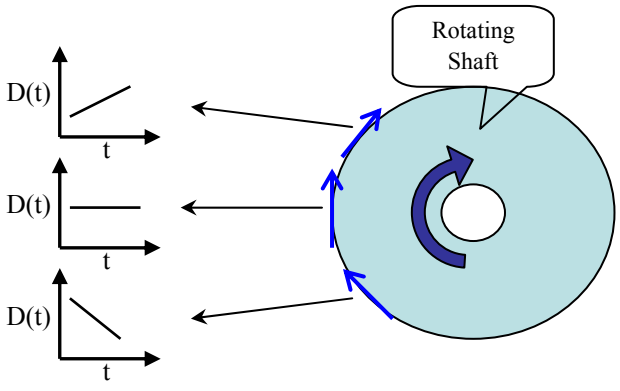

Figure 5.6. Displacements due to the misalignment of LD beam position on the shaft surface.

This error is hardly avoidable in practice due to the accuracy required in the alignment to the shaft axis. This component of the displacement is easily eliminated as the last step of the signal processing procedure, by estimating the average speed obtained and removing the introduced virtual displacement.

Figure 5.7 shows the experimental results of the reconstructed displacement after four rotations of the shaft at a frequency of 12.5Hz. It may be seen how the velocity component in the direction of the laser beam introduces a slope on the measured periodic displacement which turns into a false measured displacement of the shaft.

Figure 5.8 shows the reconstructed displacement after removing the contribution of the unwanted component of the displacement, leading to peak to peak amplitudes of about 52.9µm.

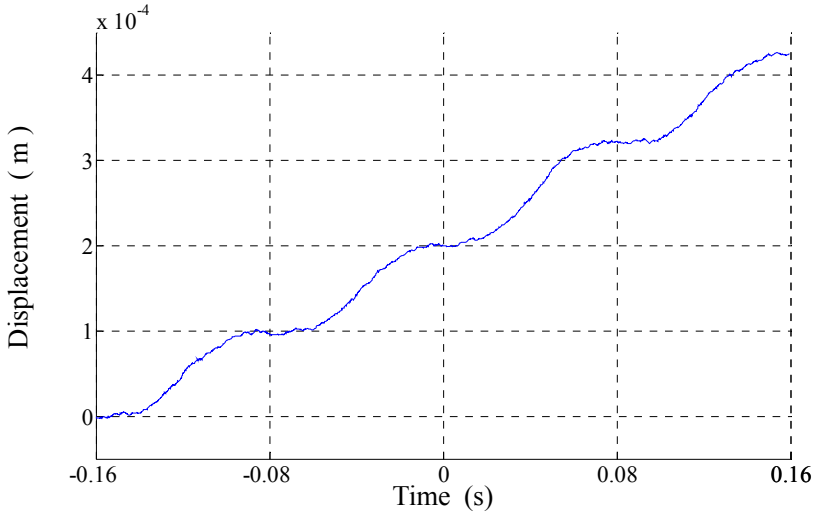

Figure 5.7. Reconstructed displacement of the rotating shaft for 4 rotations at the frequency of 12.5Hz.

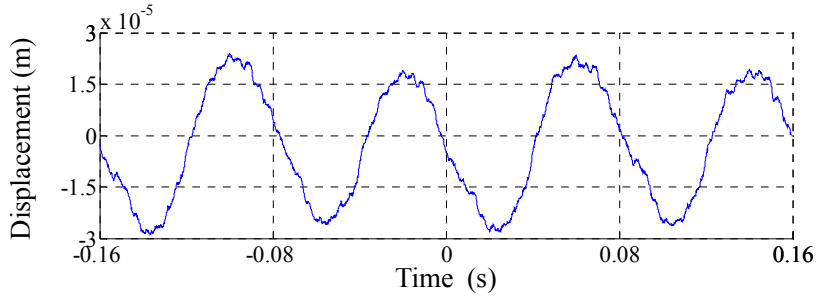

Figure 5.8. Reconstructed displacement for 4 rotations at the frequency of 12.5Hz after the removal of the unwanted displacement due to the misalignment.

5.a.4. Evaluation of the uncertainty of the measurement

An important source of uncertainty in the measurement of displacement is due to the mechanical imperfections of the rotor shaft surface, such as roundness errors, scratches, material irregularities, shape errors or other causes of eccentricity of the shaft, which are randomly added to the measurement. These imperfections bring on a level of uncertainty in the measurement which prevents it from reaching the half-wavelength resolution allowed by OFI.

To evaluate the level of uncertainty introduced by this effect, a new experiment was performed including two LDs which were collinearly aligned at both sides of the shaft, as shown in Fig. 5.9. The displacement

of one of the LDs relative to the other in absence of mechanical imperfections is expected to be linear in absence of errors, with only a constant phase delay in the absolute signals. Deviations from this linearity should be considered essentially as an effect of mechanical imperfections of the shaft, and in any case set a limit to the accuracy of the measurement.

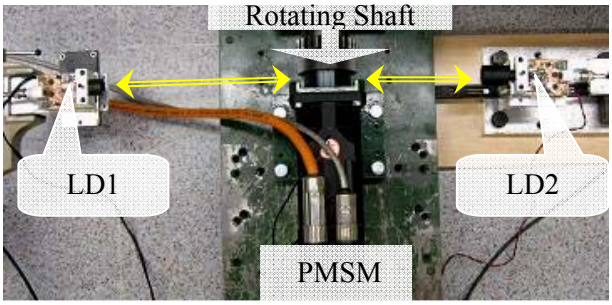

Figure 5.9. Two LD configuration to estimate the uncertainty of the measurements

Figure 5.10 shows the experimental results obtained. Using the setup of Fig. 5.9, the OOP was acquired for four rotations of the shaft at 12.5Hz. It may be observed how the uncertainty obtained in displacement reconstruction was below ±6μm, corresponding to ±11.3% of the total displacement range measured.

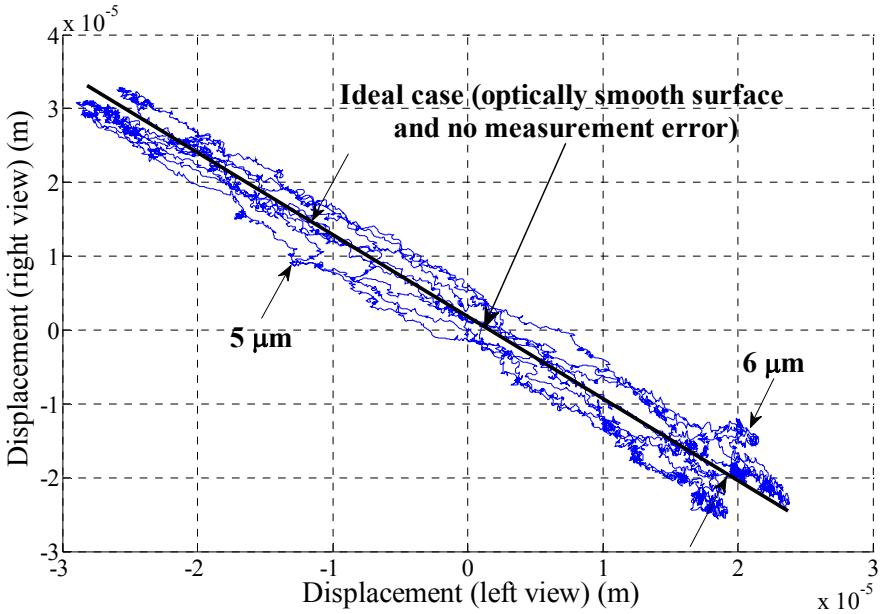

Figure 5.10. Reconstructed displacement from left view (obtained by LD1) against the reconstructed displacement from right view (obtained by LD2) for four rotations with the frequency of 12.5Hz. The straight black line stands for the ideal case of the displacement of a smooth surface.

5.a.5. Validation of the measurements

To validate the measurements obtained using the proposed technique, a commercial Polytec OFV-303 laser vibrometer has been used. Figure 5.11 shows the experimental setup, with the Polytec vibrometer pointing to one side of the shaft centreline and the LD pointing to the opposite side, collinearly and at the

same height. The goal is to measure the lateral displacement of the shaft centreline by both vibrometers comparing them once the difference in displacement direction and deviation from axis centreline has been compensated.

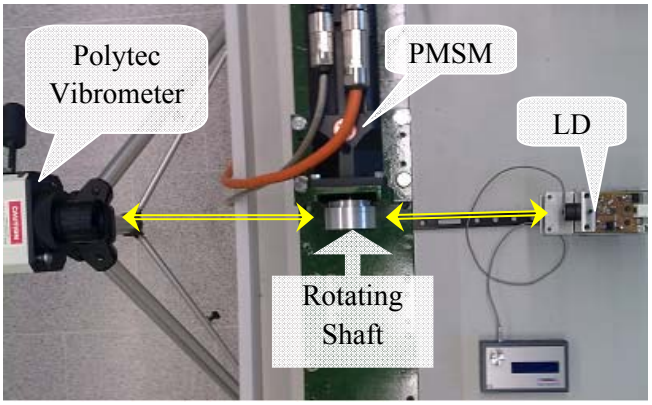

Figure 5.11. Experimental configuration for shaft runout measurement using two laser vibrometers for validation purposes.

Figure 5.12 shows the reconstructed signals of both vibrometers for the lateral displacement of the rotating shaft of a typical PMSM. In this measurement, the rotation frequency of the shaft was set to 25Hz and the acquisition time corresponded to two rotations of the shaft. The maximum variation of amplitude of the difference signal is about 12μm (±6μm) as presented in Fig. 5.12.

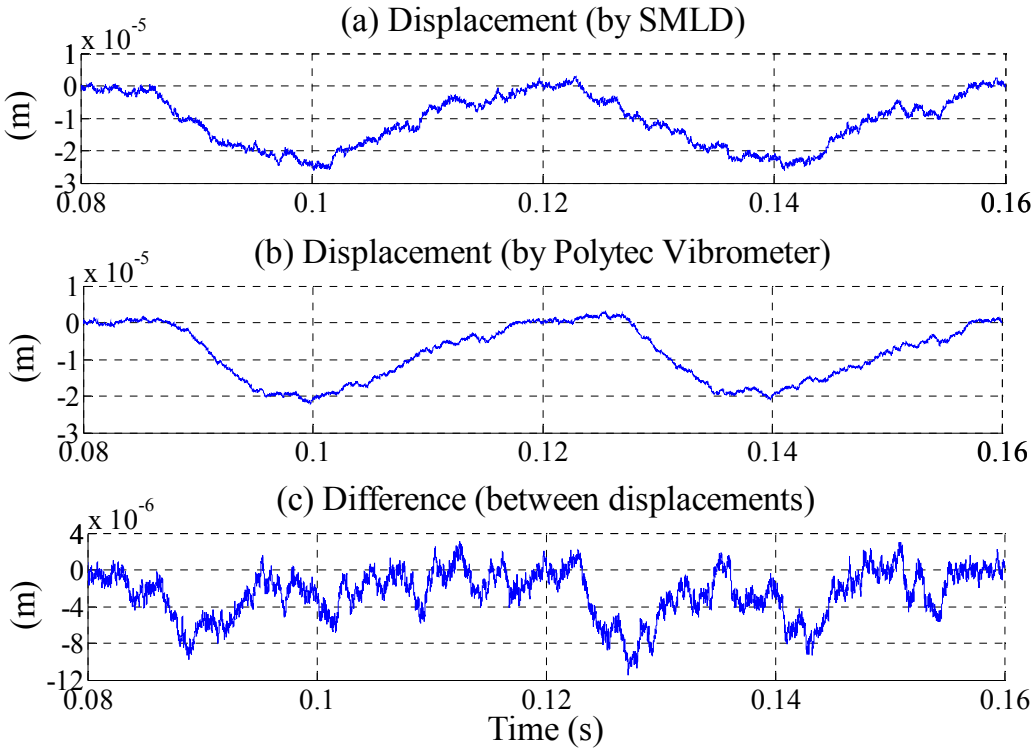

Figure 5.12. Signal reconstructions of a typical PMSM shaft displacement at horizontal direction using a Polytec vibrometer and an OFI vibrometer (SMLD) for two rotations at a frequency of 25Hz. The difference is the subtraction of the two reconstructed signals.

This difference is in full agreement with the ±6μm uncertainty calculated for the setup in section 5.a.4 due to mechanical imperfections on the shaft surface. Thus, the OFI sensor has been shown to deliver valid results with a much cheaper sensor, which shows only a higher level of noise than the reference ones.

5.a.6. Experimental results

Once the validity and accuracy of the technique has been analyzed in extent, we will present results for the 2D trajectory of the lateral axis displacement using two LD arranged orthogonally (see Fig. 5.13).

To observe the capabilities of the technique in NDT testing of PMSM motors, both a healthy PMSM and a faulty one which has some magnets demagnetized have been measured using the same setup.

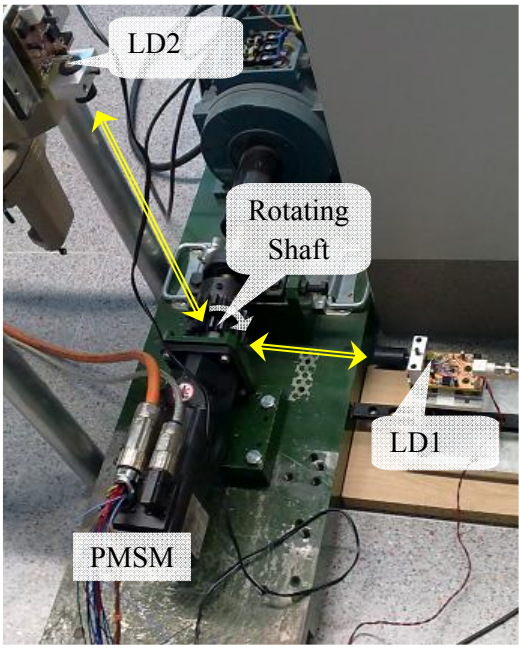

Figure 5.13. 2D measurement configuration for motor shaft runout tracking.

Figure 5.14 depicts the 2D displacement reconstruction of the shaft displacement in both motors. In the experiment, the signal of two rotations acquired when the motors were running at 25Hz is shown. Figure 5.15 shows the 2D trajectory of the displacement in polar coordinates. The shaft trajectory of the faulty PMSM may be seen to have a significantly higher amplitude and eccentricity. Detailed finite element method simulations have shown that a demagnetized machine generates unbalanced radial forces which may generate mechanical effects. The model of the measured shaft trajectory presents realistic results for fault diagnosis of demagnetization for a PMSM subject to test.

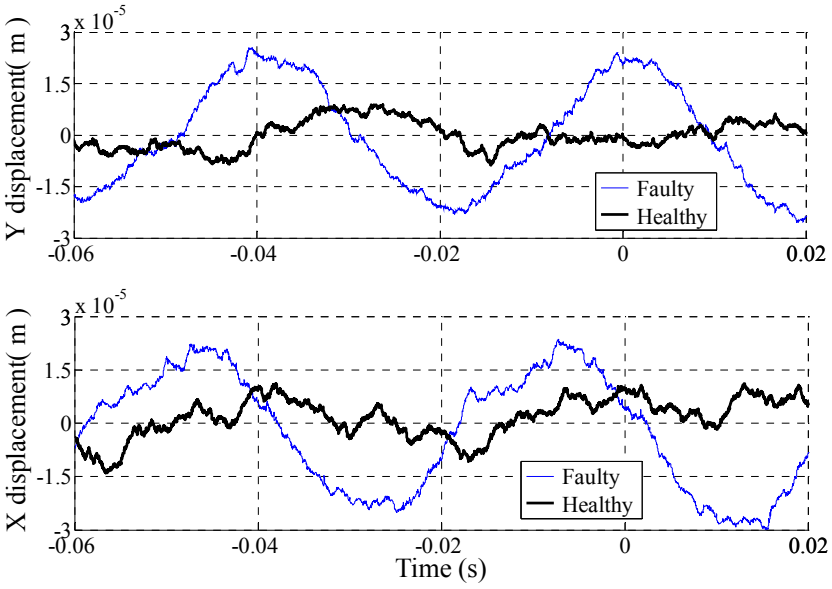

Figure 5.14. Reconstructed shaft displacements in X and Y axes for a healthy and a faulty PMSM when running at 25Hz. Two periods are acquired in the measurement.

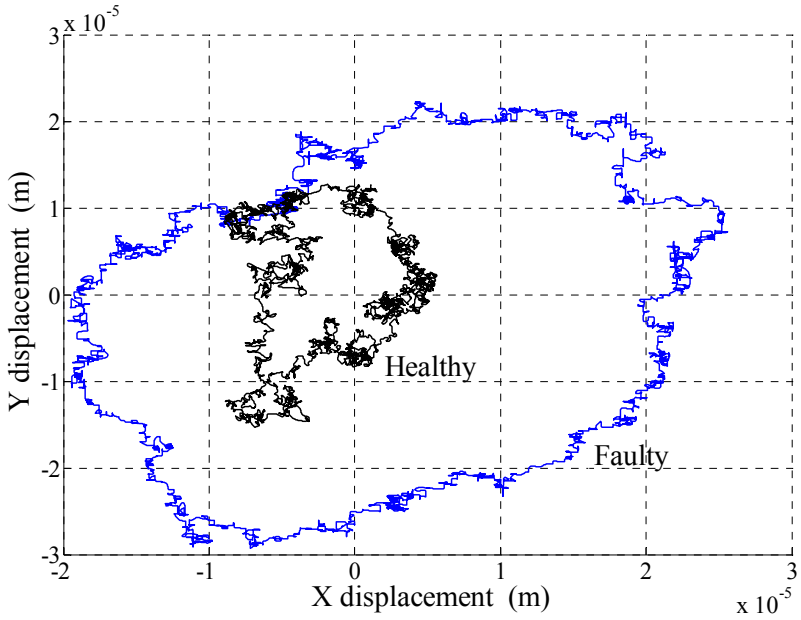

Figure 5.15. 2D trajectory of the shaft displacement in X-Y plane for a faulty and a healthy PMSM running at 25Hz. Faulty PMSM exhibits a much larger displacement and eccentricity

5.b. Beam deformation measurement

As a second experimental implementation, an OFI sensor has been applied as proximity probe to monitor the bending of large polymer reinforced beams used in civil engineering applications, under dynamic loading. As in the previous Section, a detailed description of the problem and the measurement procedure

used is presented with view to potential applications in the analysis of mechanical structures, where continuous monitoring on bridge conditions using bridge dampers was proposed. Structural non-destructive testing of composite elements was another potential application which could benefit from the results of this Section.

5.b.1. Introduction

The correct characterization of materials has been for several years a keystone of modern engineering design. It is possible to find references to mechanical properties of materials such as Young's module, yield strength or rupture limits in mechanical design books [Beer 2001]. However, those values only are well known for a limited number of materials. When the material used in a given design is out of the scope of such tables, or when properties are dependent on the geometry of the element, it becomes necessary to measure the performance of the material in a given application with a reliable sensor. A good example of materials which typically need to be tested are composites [Hashin 1983], which can easily vary its mechanical performance with shape due to its anisotropic structure. Even though material characterization is of general interest to every design, it is more important in the case of structural building materials, which are subjected constantly to different dynamic and static loading effects.

It is not possible to measure all characteristics of one given material in a direct fashion. Usually, indirect methods that consist on quantifying the strain ($\Delta L/L$) or the deformation produced on the loading axis are applied to measure those properties. The evaluated deformation is then compared with the known applied effort to get a relationship from which it is possible to extract a local value of the property. Thus, a sensor capable of quantifying accurately deformation in a linear fashion is a requirement for material characterization.

Most commonly, the deformations measured in material testing are limited to a range that goes from a few microns to a couple of millimeters. This implies the sensor used should have submicron resolution and a bandwidth from sub-Hz to several hundred Hz in the case of fatigue testing [El-Tawil 2001]. Many types of sensors are used in material testing [Medlock 1983], although amongst the most common we find LVDTs and strain gauges. Recently other sensors based in fiber-optics have started to be applied in this type of measurements [Lawrence 1999].

Strain gauges are probably the most usual sensors for material testing. They are contact sensors which increase or decrease their resistivity depending on the strain applied on them. The use of strain gauges is largely extended because of their low cost, linearity, and availability in many sizes [Chalmers 1993]. Usually they are used in resistive electronic arrays such as Wheatstone or Kelvin bridges. One main problem which appears while measuring strain with gauges is related to the selection of the geometry, its calibration and its contact with the sensed material. The selection of the geometry is not obvious if there is no information on the expected deformation. Contact depends on the use of good adhesives, and the ability of the user to place the gauges in the correct position. Finally, previous calibration with an external

comparison tool is needed to assure the measured values using the gauge agree with the real displacement.

LVDTs are electromechanical transducers which can convert rectilinear motion into its corresponding electrical signal. The output is quantified as a differential value between two secondary coils [Fan 2001], induced by an electromagnetic moving core. In this case, the contact between the tip of the LVDT moving core and the tested material has to be assured. Some of the main advantages in strain measurement with this type of sensors are the lack of mechanical hysteresis, the fast dynamic response and their insensitivity to radial movements. The main disadvantages rely on their limited displacement range, the sensitivity to temperature changes, their linearity and their cost.

Looking carefully at the measuring needs, and to the advantages and disadvantages which other sensors present, we propose the use of OFI as a suitable transducer for strain measuring. The technique is useful for measuring sub-micron vibrations with high accuracy. Furthermore, as described in chapter 2, OFI has shown to be a reliable method for measuring vibrations, displacement and absolute distance.

In this section, we demonstrate the use of an OFI sensor for measuring the beam deformation under dynamic loading. Since the deformations may be potentially large (may reach up to some millimeters or even centimeters) speckle effects are expected to appear in the acquired OOP of the LD, leading to frequent signal fading. Thereby, the adaptive speckle control technique which has been presented in this thesis is expected to be an efficient solution for speckle management in this application. However, once on the field application, the reflectivity conditions of the beam yielded just a fading zone in the complete displacement range, which could be easily managed using the same procedure for adjustment of spot size which was proposed for the motor runout application. It should be stressed that this is not the general condition, as far as displacements of some centimeters typically involve some unavoidable fading regions, which was not the case in this particular case.

Next we will cover the measurement procedure and the solution for speckle management. Then, the results of the test done using the OFI sensor for measuring the deformation of a composite beam subject to dynamic loading will be presented. Results will be compared with those of a LVDT sensor to show the agreement of results between the proposed OFI non-contact measuring method with a classical contact mechanical transducer. This work was performed in collaboration with Prof. Lluís Gil, from the LITEM research group at the Terrassa Campus of UPC.

5.b.2. Measurement procedure

In the measurements we used a Hitachi HL7851G LD emitting at a wavelength of 793nm and a maximum output power of 50mW. The LD is directly pointing to a beam which will undergo dynamic loading tests. This testing will introduce changes in the optical path in the LD external cavity which will result into frequency beats. The FCM algorithm has been applied for signal processing. The resolution of $\lambda/2$

provided is far over the requirements of most civil engineering applications. The whole signal processing scheme after signal acquisition is shown in Fig. 5.16. The process is equivalent to the one applied to motor shaft runout tracking at section 5.a.3 but for the misalignment correction stage, which has been removed as it has no sense in this application. As a first step, a moving-average low-pass filter (LPF) [Zabit 2009] is applied to the acquired OOP to eliminate the high frequency noise which typically appears in real applications, especially in harsh environment. The phase signal and displacement are then obtained as in the previous Section.

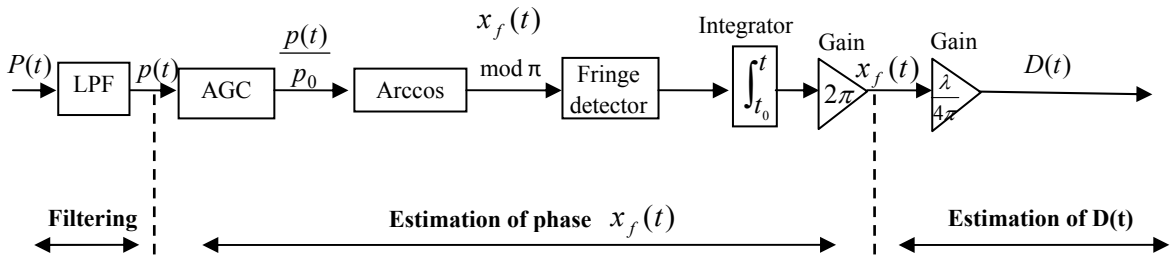

Figure 5.16. Block diagram of the signal processing procedure for displacement reconstruction in a beam deformation application.

5.b.3. Management of speckle effect

The main disadvantage of using an OFI sensor is the appearance of speckle effect modulating the amplitude of the OOP signal in large displacement ranges, due to the roughness of the target surface roughness. The fading regions which appear, as explained, lead to degradation of the accuracy of the data taken, and to loss of relevant information in the measurement.

Due to the small speed of the target, the adaptive speckle control solution and the optimization of spot size should be considered for speckle management in this application. It should be taken into account that spot size adjustment is suitable for relatively large displacements given that only one or two black-out zones may appear in the signal depending on surface roughness. For larger displacements this technique can't manage the speckle effect so it will not be possible to remove the fading zones of the OOP. In these cases, the adaptive solution is the most effective one, as its limitation to slow displacements (< 0.2mm/s) is not a problem in this application.

5.b.4. Experimental results

As an experimental proof to use OFI as a sensor for measuring beam deformation under dynamic loading, the deformation of a composite beam made of GFRP (Glass Fiber Reinforced Polymer) was measured. The measurement configuration is shown in Fig. 5.17. A GFRP beam was under loading at its center using a controlled electro-mechanic machine (Suzpecar 50kN), with both ends of the beam placed on the fixed, rounded metallic cylinders which acted as reliance points.

The OFI sensor together with a HBM WA/20mm LVDT sensor which will be used for comparison were placed at 155mm from the loading point, in order to monitor the vertical displacement of the GFRP beam surface at the measurement point. At the loading point a displacement of roughly a millimeter with low speed (about 0.067mm/s) is applied to the beam. At the measurement point the displacement is expected to be some hundreds of microns (below a millimetre).

Although it is physically impossible to place the LVDT sensor head exactly at the point where the laser spot is pointing, efforts were made in order to minimize the distance between both points and to place them under an optimized geometry where comparable displacements were expected. As may be seen in Fig. 5.18, both sensing points were placed at the same distance from the loading point and as close together as possible.

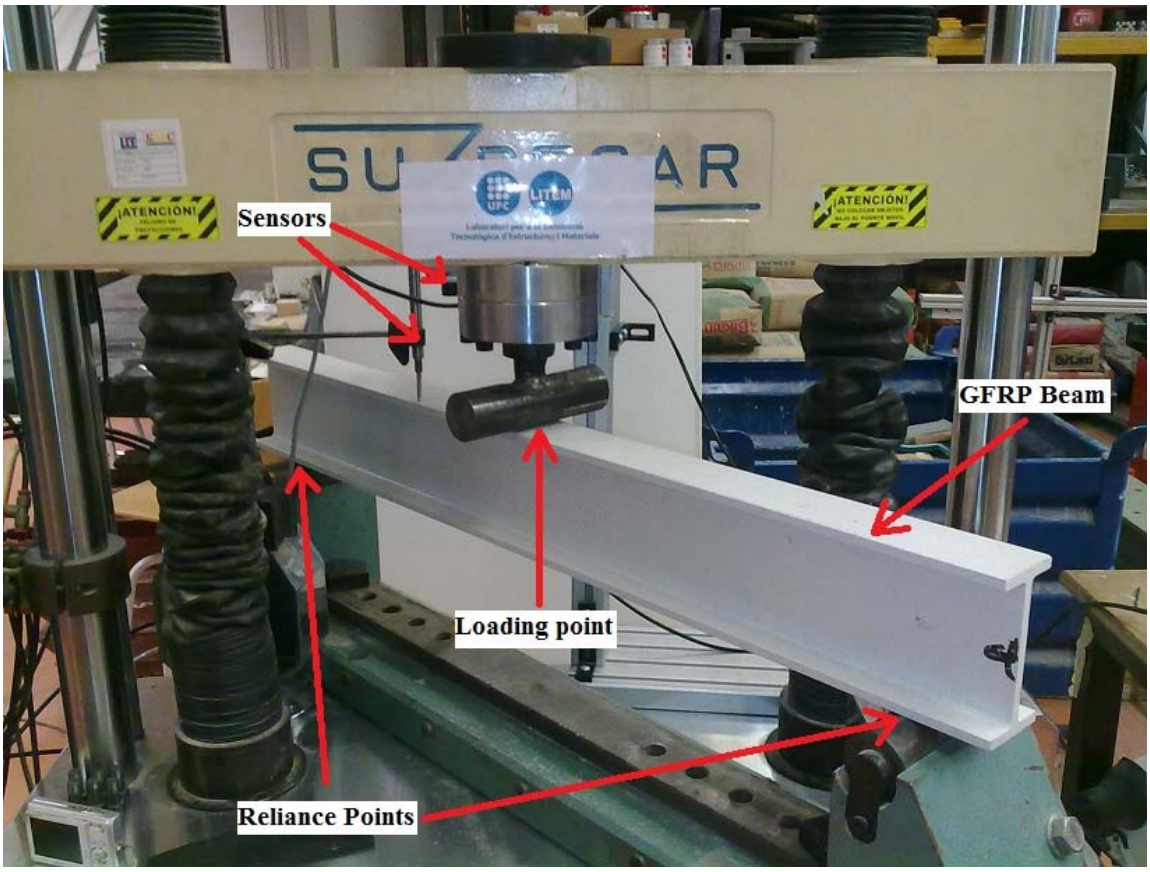

Figure 5.17. Experimental configuration for beam deformation measurement.

Figure 5.19 shows the experimental OOP signal affected by the speckle effect having one fading area in the signal. As seen in the figure, in the fringe detection algorithm of the normalized OOP, the fringes of the fading region were undetected due to its low SNR, which made impossible to recognize the fringes out of the noise. To recover the lost fringes and achieve the correct detection, the spot size was adjusted to change the position of the speckle spot in order to obtain the OOP signal without fading. Figure 5.20 shows the results of the same experiment under the new spot size condition. As seen, in the OOP now

there is neither a speckle modulation nor a black-out region, so the fringes are correctly detected leading to displacement reconstruction with half-wavelength resolution.

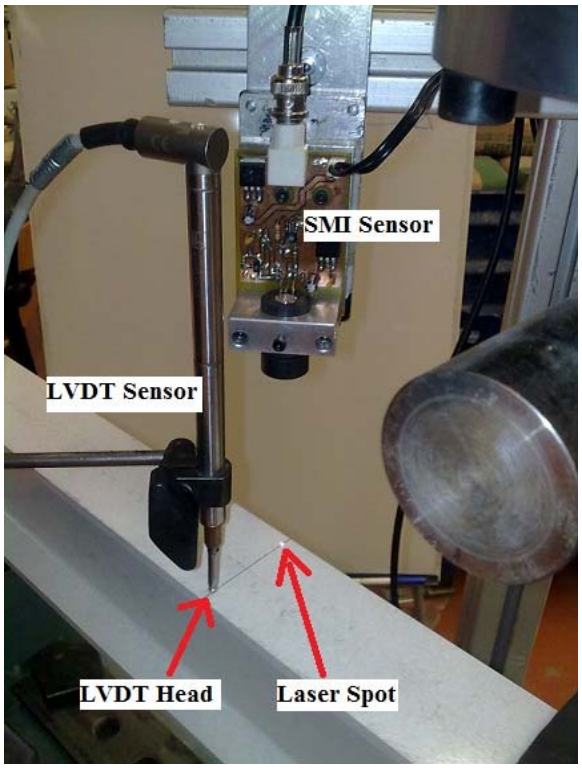

Figure 5.18. Sensor configuration; OFI sensor and commercial LVDT sensor used for comparison.

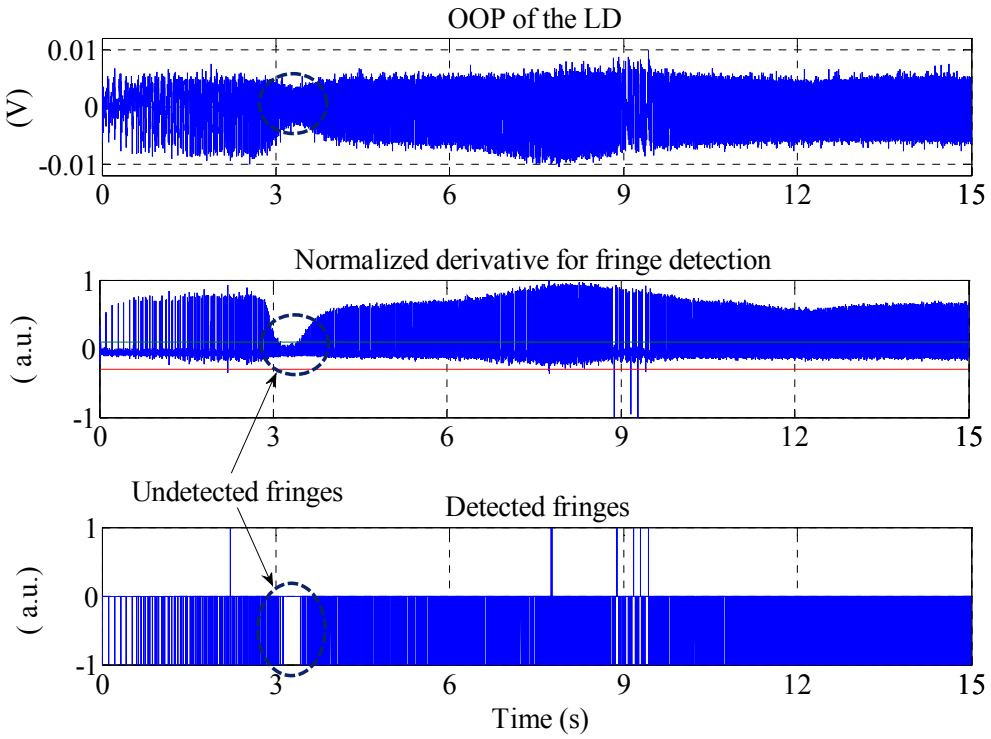

Figure 5.19. Experimental results; OOP of the LD affected by speckle effect showing a fading region in the signal, leading to undetected fringes in the signal processing.

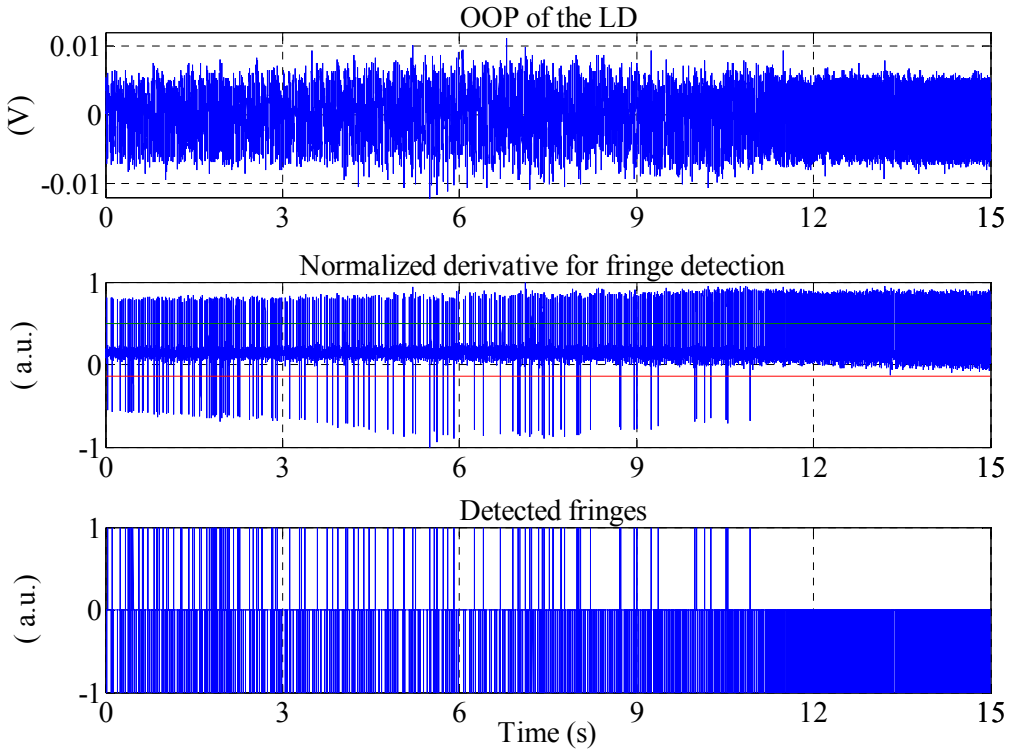

Figure 5.20. Experimental results; OOP of the LD without speckle modulation.

Figure 5.21 illustrates the displacements measured by both sensors (OFI and the LVDT sensor), and the difference of the obtained displacements for comparison purposes.

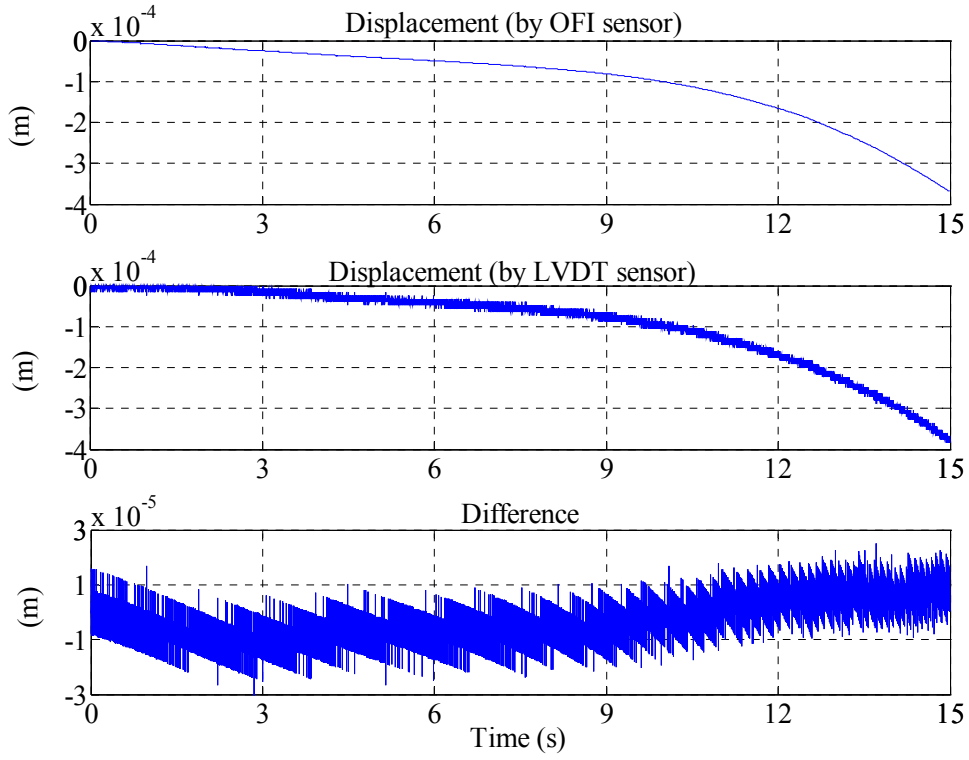

Figure 5.21. Beam displacement measured by OFI and LVDT sensors and their difference for comparison purposes.

Although the measurement resolution by OFI is the basic resolution of the sensor (396.5nm), the LVDT signal was quite noisy and presented a high-frequency variation equivalent roughly to a 20µm displacement, as seen in the figure.

To better compare the displacements achieved by the sensors, a low-pass filter has been applied to the LVDT signal to eliminate the high frequency noise. Figure 5.22 shows the filtered LVDT sensor signal together with the OFI signal for better comparison. The difference between the reconstructed displacements is shown in Fig. 5.23 was kept below 20µm (about 2.9% of the measurement range).

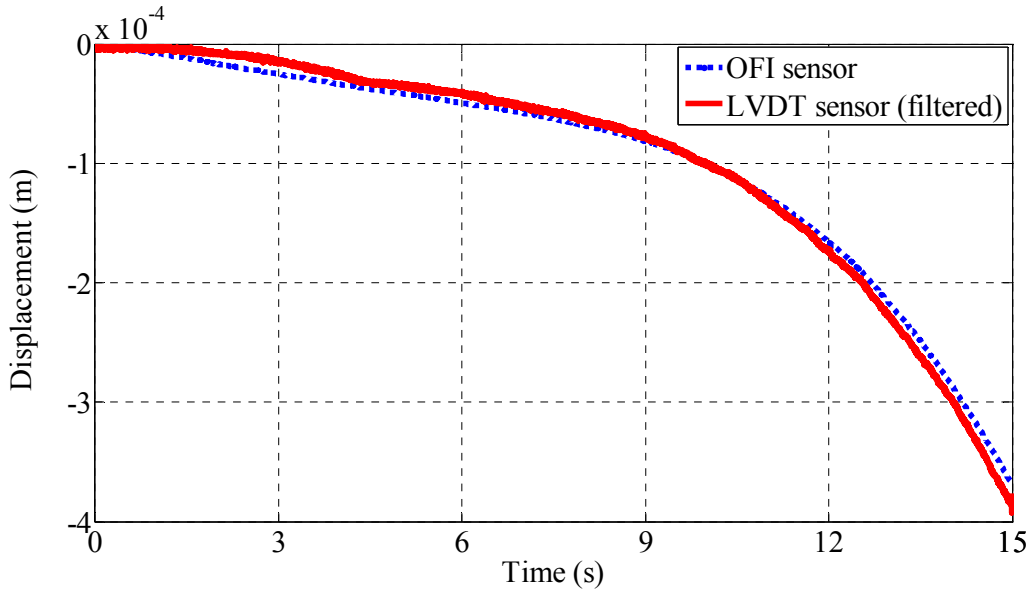

Figure 5.22. Beam Displacement measured by OFI and LVDT sensors.

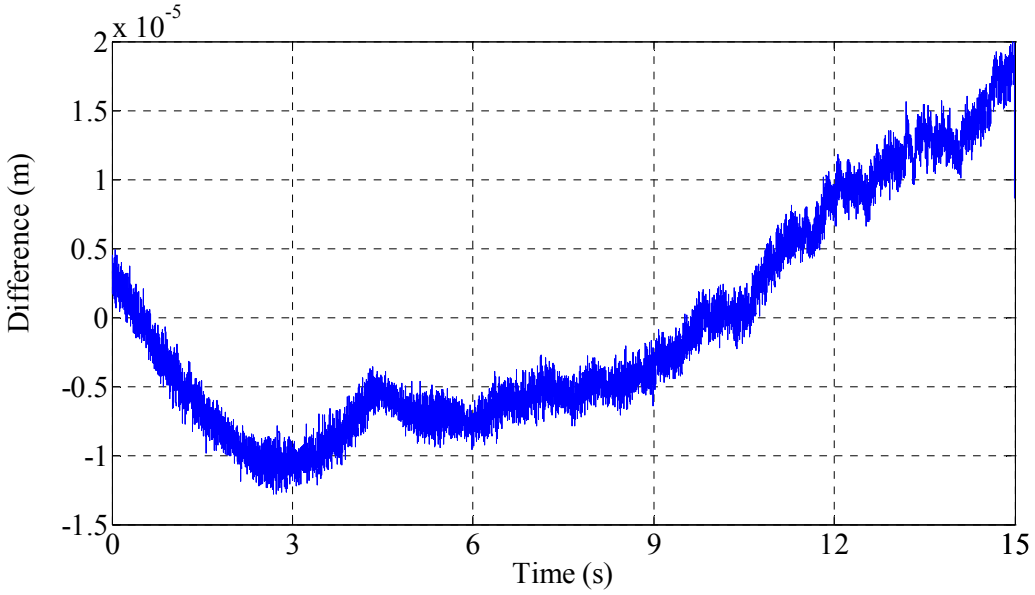

Figure 5.23. Difference in displacements measured by OFI and LVDT sensors.

The small differences present in both signals are interpreted essentially as due to the noise in the LVDT signal, and to the physical impossibility of measuring in slightly different points, so small torsions or other effects may appear in the measurement. The results prove the feasibility of using OFI as a sensor for material deformation measurements under dynamic loading conditions.

5.c. Conclusion

In this chapter, two new applications of OFI in which the speckle effect may significantly affect the measurements have been presented, and speckle noise has been managed properly in both of them. Results show the capabilities of the OFI sensor to be used as proximity probes in a number of applications in industrial, harsh environments.

In one of the applications, a complete methodology for the measurement of the motor shaft runout using OFI has been demonstrated in detail. The experimental results have shown the capability of OFI sensors to provide the detailed trajectory of a motor shaft, suitable for being used as a new proximity probe for non-contact motor fault diagnosis.

In the second application, an OFI sensor was proposed for measuring the deformation of composite GFRP beams under dynamic loading. Simultaneous displacement measurements were taken on a dynamically loaded beam with an OFI sensor and a LVDT sensor, to validate the performance of the proposed sensor. The reconstructed displacement signal shows that the difference of both signals is kept below 20μm during the experiment, validating the capabilities of the OFI sensor as proximity probe for the proposed application.

6. Conclusion & future works

The present thesis was started with the aim of improving the performance of OFI-based sensors combining them with optical systems, in particular with the incorporation of some adaptive optics capabilities, without large increments in the complexity of the setup. It broke ground at CD6 as it was the first PhD work related to OFI, and added a novel point-based interferometric technique to the background of the Optical Metrology Group. The technique has developed into a very interesting and innovative research line with both scientific and practical interest, with three more PhD works under development at present. The first conclusion of this Thesis, thus, is that a novel, very promising research line in Optical Metrology has appeared within CD6 enhancing the problem-solving capabilities of the Centre.

As a general scientific conclusion, we have shown for the first time that the control of the feedback level of a laser diode, and the control of the SNR of a speckled OOP, can be performed using an electro-optical lens. An auto-adaptive OFI sensor, operator-free, and precise even for large displacement ranges when speckle effect appears has been designed, built and demonstrated. Adaptive feedback control has been complemented with adaptive speckle control, a solution able to cure the signal fading affecting the OOP due to speckle effect in large range displacements. Some applications have been presented showing the usefulness of the approach.

A number of detailed conclusions with more reduced scope have also been presented along this Thesis, and are recovered here as a summary of the work performed.

Commercially available variable-focus liquid lenses have been analyzed in order to enable an electrically controlled focusing of the laser beam, and its active real-time control out of signal parameters. Among the available solutions, voltage-programmable electrowetting-based liquid lenses were found to be the best choice for our purposes. However, since it was not possible to use them alone in front of the laser for long range focusing, an appropriate optical system (the adaptive optical head, AOH) including an aspheric lens combined with the liquid lens was designed and built to enable a long range of focusing distances.

A number of experiments were presented showing the capabilities of controlling the feedback level using the proposed solution. By changing the focal distance of the liquid lens using the AOH, it was possible to modify the feedback level from the weak regime to a moderate regime with large hysteresis, yielding severe fringe loss conditions. The capability of the AOH to keep feedback level (or, equivalently, the coupling factor) in a desired condition was experimentally demonstrated. Experiments also showed how l fringes lost due to an excessive feedback level can be recovered by modifying the focal length of the liquid lens, and subsequently the spot size on the target, using the AOH.

This control of the coupling factor enabled the proposal of a novel high resolution sensor based in the comparison of the OOPs of two laser diodes. This novel technique improves the accuracy and the resolution of the measurements of displacement using OFI sensors, enabling for the first time

measurements of amplitudes below the λ/2 limit. The technique compares the positions of the fringes which appear in the OOP of the two lasers, one of them stationary and pointing to a moving stage, where the second laser is mounted while pointing at the target to be measured. The stationary laser plays the role of reference sensor and the vibrating laser is used as measurement sensor. The vibration of the measurement laser brings on the appearance of fringes in the OOP of both lasers. The performance of the system was validated by simulation yielding resolutions in the nm level, well beyond the displacements normally measured using OFI sensors, with magnitudes below the λ/2 value. Simulations also showed the relevance of the matching of the feedback levels to a coupling factor close to 1 in both lasers in order to achieve the best experimental results, a matching easily performed using the adaptive solution proposed. A preliminary experimental setup was built to test the capacities of the proposed high resolution sensor. Experimental results for a sampling rate of 160Hz showed an average error of 3.6nm for a target displacement of 265nm. This accuracy accounts for λ/200, well beyond the λ/25 values attained as maximum accuracy in the literature.

Beyond feedback control, it was also proposed to use spot size adjustment using the AOH to modify the speckle pattern of the laser and cure signal fading effects by improving the SNR of the OOP. Thereby, the speckle affected OOP signal was experimentally characterized, finding that over the undesired reduction of the SNR in the signal, the appearance of speckle modifies the coupling factor, and subsequently the feedback regime, along the displacement of the target. Based on experimental results on controlled roughness samples, it has been demonstrated that the speckle pattern is related to the roughness of the surface of the target, and that it changes with the size of the beam spot on the target. This results showed the potential feasibility of modifying the speckle pattern by adjusting the spot size of the beam on the target (by changing the focus at the AOH), in order to avoid signal fading along the measurement.

From these results, a real time speckle control algorithm based on the control of the SNR of the OOP was implemented to modify the spot size by focus adjustment when the signal faded below a threshold value. A real-time algorithm was programmed and tested in an experimental case of large displacements, a typical real-world experiment where speckle effects are bound to appear. The control algorithm showed its capability to actively adjust the spot size during the complete target displacement to compensate for reductions in SNR, and to acquire the complete OOP without fading. This enabled the acquisition of the full OOP signal without losing any fringe for target displacements up to 20mm.

However, this adaptive solution cannot be applied to fast displacements as the speckle control speed is limited by the time response of the liquid lens to modifications in focal length. The maximum target speed in which the speckle control algorithm could successfully manage to avoid signal fading was 0.2mm/s. For higher target velocities, another solution for speckle control based on the sensor diversity principle has been proposed. Sensor diversity uses two lasers pointing to the same target with slight differences in the experimental conditions. Differences can be either spatial (lasers pointing at different

points of the sample or with different spot sizes) or in the frequency domain (lasers with different wavelengths). Slightly different experimental conditions take advantage of having different speckle pattern in the OOPs in both lasers. This method has also been implemented and tested in this thesis, showing how the probability of fading reduces very significantly although it cannot guarantee the full disappearance of the problem.

Furthermore, two real experimental applications developed have been presented to demonstrate the applicability of the adaptive solution in the OFI based sensor configuration for speckle control when large target displacements are present.

In one of the applications, shaft runout measurements in electric motors where performed in order to enable non-destructive maintenance procedures. In this setup, the expected displacements were in the order of some tens of microns introducing speckle shift. Spot size adjustment enabled to have no fading area in the acquired OOP signal. A full measurement procedure for the measurement of the 2D trajectory of the runout in a motor shaft was also developed, and validated using a commercial vibrometer.

Another application of OFI based sensor was material characterization, applied to the measurement of reinforced polymer concrete beams used in civil engineering. The displacement range in these applications, where the beam is loaded to test its resistance, can be from a few millimetres to some centimetres. For such large displacements, the speckle phenomenon can obviously affect the measurements, so the adaptive solution is proposed as the best way to deal with the speckle for this type of applications. Measurements on beams have been compared with results obtained using a conventional LVDT sensor, showing total agreement.

All contributions have been presented as peer reviewed publications (two still under evaluation), patents and international conferences, listed in chapter 8.

Regarding future work, several options are open. Since an FPGA based electronic card incorporating the OFI sensor has been proposed for OOP signal processing, spot size control either for speckle or for feedback level management could be incorporated in the same electronic card. The algorithms for feedback adjustment, speckle control for large displacements, and specific algorithms for given applications (like the ones developed for shaft runout tracking in electric motors) can be included within the same card. In the event of a successful implementation, an autonomous, robust, operator-free, and user-friendly sensor for short and large displacements will be available to everyone at a very low cost.

Besides, the performance of the double laser solution here proposed was theoretically and experimentally investigated in this thesis, but a lot of space was left for detailed analysis and implementation of the proposed solution. A new PhD thesis is currently under development at CD6 for the analysis of such a solution, the analysis of the experimental constraints involved, the optimization of its performance, and the development of related applications.

7. References

M. A. **Amann**, T. Bosch, M. Lescure, R. Myllyla, and M. Rioux, "Laser ranging: a critical review of usual techniques for distance measurement," Optical Eng., 40, 10-19 (2001)

V. **Annovazzi-Lodi**, S. Merlo, M. Norgia, "Measurement on a micromachined silicon gyroscope by feedback interferometry," IEEE/ASME Transactions on Mechatronics, 6(1), 1-6 (2001)

V. **Annovazzi-Lodi**, S. Merlo, M. Norgia**,** G. Spinola, B. Vigna, S. Zerbini, "Optical detection of the coriolis force on a silicon micromachined gyroscope," IEEE/ASME Journal of Microelectromechanical systems, 12(5), 540-549 (2003)

R**. Atashkhooei**, U. Zabit, S. Royo, T. Bosch and F. Bony, "Adaptive optical head for industrial vibrometry applications," Proc. SPIE 8082, 80821W, Munich (2011a)

R. **Atashkhooei**, U. Zabit, S. Royo, F. Azcona and I. Sergievskaya, "Adaptive feedback control in Self-mixing Interferometry Using Active Optical element," Proc. AOIM (Adaptive Optics for Industry and Medicine) 8th Int. Conf., Murcia (2011b)

R. **Atashkhooei**, S. Royo, F. Azcona and U. Zabit, "Analysis and Control of Speckle Effects in Self-mixing Interferometry, " in Proc. IEEE sensors, Limerick (Ireland), pp. 1390-1393, 28-31 Oct. (2011c)

R. **Atashkhooei**, F. Azcona, S. Royo, L.G. Espert, "Optical feedback interferometry for measuring dynamic stress deformation of beams," in Proc. AIVELA 2012, Vol. 1457, Ancona (Italy), pp. 132-138 (2012)

R. **Atashkhooei**, S. Royo, F.J. Azcona, "Dealing with Speckle Effects in Self-mixing Interferometry Measurements", IEEE Sensors J., 13(5), 1641-7, (2013a)

R. **Atashkhooei**, J. Urresty, S. Royo, J-R Riba Ruiz, L. Romeral, "Runout Tracking in Electric Motors by Self-mixing Interferometry", IEEE Transaction on Mechatronics, in press (2013b) (Early access article)

R. **Atashkhooei**, S. royo, J. Pladellorence Malofre "Adaptive Auto-focusing Technique for Real-time Speckle Control in Optical Feedback Interferometry", Sensors actuators A, (2013c)

F.J. **Azcona**, R. Atashkhooei, S. Royo, J. Mendez, A. Jha, "A method to measure sub nanometric amplitude displacements based on optical feedback interferometry," in Proc. SPIE 8789, Munich (2013a)

F.J. **Azcona**, R. Atashkhooei, S. Royo, J. Mendez, A. Jha, "A Nanometric Displacement Measurement System Using Differential Optical Feedback Interferometry", Photo. Tech. Lett. (2013b) (submitted)

F. P. **Beer**, E. R. Johnston, J. T. DeWolf, "Apendix B" in Mechanics of Materials, edited by L. A. Valdez, Mexico DF: McGraw-Hill Interamericana, 746 – 749 (2001)

G. **Beni**, S. Hachwood and J.L. Jackel, "Continuous electrowetting effect" Appl. Phys. Lett., 40(10), 912-914 (1982)

B. **Berge** and J. Peseux, "Variable focal lens controlled by an external voltage: an application of electrowetting," Eur. Phys. J. E, 3, 159–163 (2000)

B. **Berge**, "Liquid lens technology: principle of electrowetting based lenses and applications to imaging," Proc. IEEE in MEMS, 227-230 (2005)

B. **Berge**, "Liquid lens technology for adaptive optics: principle, physical limitations and applications," Kogaku Shinpojiumu Koen Yokoshu (31st Kogaku symposium), 31, 55-56 (2006)

G. **Berkovic** and E. Shafir "Optical methods for distance and displacement measurements," Advances in Optics and Photonics, 4, 441-471 (2012)

C. **Bes**, G. Plantier and T. Bosch "Displacement Measurements Using a Self-mixing Laser Diode Under Moderate Feedback," IEEE Trans. On Instrumentation and Measurement, 55(4), 1101-1105 (2006)

C. **Bes**, T. Bosch, G. Plantier and F. Bony, "Characterisation of a self-mixing displacement sensor under moderate feedback," Optical Engineering, 45(8), 084402-1 – 084402-6 (2006b)

C. **Bes**, V. Belloeil, G. Plantier, Y. Gourinat and T. Bosch, "A self-mixing laser sensor design with an extended Kalman filter for optimal online structure analysis and damping evaluation," IEEE/ASME Trans. on Mechatronics, 12(3), 387-394 (2007)

T. **Bosch**, N. Servagent, R. Chellali, and M. Lescure, "Three-Dimensional object construction using a self-mixing type scanning laser range finder," IEEE Trans. On Instrumentation and measurement, 47(5), 1326-1329 (1998)

T. **Bosch**, N. Servagent, and S. Donati "Optical feedback interferometry for sensing application," Opt. Eng., 40(1), 20-27 (2001)

T. **Bosch** et al "Optical feedback interferometry," Encyclopedia of sensors (EOS), Vol. X, 1-20 (2006)

L. **Compagnolo**, S. Roman, J. Perchoux, and S. Lorthois, "A new optical feedback interferometer for measuring red blood cell velocity distributions in individual capillaries: a feasibility study in microchannels," Comput. Methods Biomech. Biomed Eng., 15, 104-5 (2012)

L. **Compagnolo** et al, "Flow profile measurement in microchannel using the optical feedback interferometry sensing technique," Microfluidics and Nanofluidics, in press (2012b)

L. **Compagnolo**, "Optical feedback interferometry sensing technique for flow measurements in microchannels," PHD Thesis, INPT-ENSEEIHT, University of Toulouse, France (2013)

J. **Caum**, J.Arasa, S.Royo, M.Ares "Design of adaptive digital filters for phase extrcation in complex fringe patterns obtained using the Ronchi test," J.Mod.Opt., 59(8), 721-728 (2012)

G. F. **Chalmers**, "Materials, Construction, Performance and Characteristics", in Strain Gauge Technology, edited by A. L. Window, Springer, 1 – 38 (1993)

J. **Chass**, F. Hills, "Linear Variable Differential Transformer," U.S. Patent 3 546 648, Dec. 8 (1970)

L. A. **Coldren** and S. W. Corzine, "Diode lasers and photonic integrated circuits," New York: John Wiley & Sons Inc. (1995)

M. **Dabbicco**, A. Intermite, and G. Scamarcio, "Laser-self-mixing fiber sensor for integral strain measurements," J. Lightwave Tech., 29(3), 335-340 (2011)

J.C. **Dainty,** "Laser Speckle and Related Phenomena," Springer Berlin (1975)

M.J. **DeBlock**, B.M. Wood, J.W. McDonnell, "Predicting Shaft Proximity Probe Track Runout on API Motors and Generators," in Proc. Petroleum and Chemical Industry Technical Conf., Calgary, 1-8 (2007)

S. **Donati**, "Laser interferometry by induced modulation of the cavity field", Journal of Applied Physics, 49, 495-497 (1978)

S. **Donati**, G. Giuliani and S. Merlo "Laser diode feedback interferometer for measurement of displacements without ambiguity," IEEE J. Quantum Electron., 31, 113-119 (1995)

S. **Donati**, L. Falzoni and S. Merlo "**A** PC-Interfaced, Compact Laser-Diode Feedback Interferometer for Displacement Measurements," IEEE Trans. On Instrumentation and measurement, 45(6), 942-947 (1996)

S. **Donati**, "Electro-Optical Instrumentation – Sensing and Measuring with Laser," Prentice Hall, USA, see chapter 4 (Interferometry) and 5 (Speckle Pattern) (2004)

S. **Donati**, "Developing Self-Mixing Interferometry for Instrumentation and Measurements," Laser Photonics Rev., 6(3), 393-417 (2012)

A. **Doncescu**, C. Bes and T. Bosch, "Displacement Estimation with an Optical Feedback Interferometer Using an Evolutionary Algorithm," Proceedings of 2007 IEEE Sensors, 382-386 (2007)

Edmund Optics Inc., Surface roughness standard, http://www.edmundoptics.com/testing-targets/calibration-standards/surface-roughness-standard/2468

J. **El Assad**, "Analysis of self-mixing moderate and strong feedback regimes for mechatronics applications," PHD Thesis, INPT-ENSEEIHT, University of Toulouse, France (2008)

B. S. **El-Tawil**, C. Ogunc, A. Okeil, M. Shahawy, "Static and Fatigue Analysis of RC Beams Strengthened with CRFP Laminates," Journal of Composites for Construction 5, 258-267 (2001)

J. **Fan**, S. Jia, W. Lu, Z. Wang, X. Li, J. Sheng, "Application of LVDT Sensor Data Acquisition System Based on PCI-1716"in IEEE International Conference on Computer Science and Automation Engineering (CSAE)-2011, Shanghai, 54 (2001)

Y.H. **Fan**, H. Ren and S.T. Wu, "Switchable Fresnel lens using polymer-stabilized liquid crystals," Opt. Exp., 11(23), 3080-3086 (2003)

Y. **Fan**, "Improvement of measurement performance for self-mixing interferometry based displacement sensing system," Master of Eng. By research Thesis, School of Elec., Comp. And Telecom. Eng., University of Wollongong, Australia (2011)

J.Y. **Fang** et al, "Optical feddback height control system using laser diode sensor for near-field data storage applications," J. Lightwav. Technol., 25(12), 3704-3709 (2007)

M. T. **Fathi** and S. Donati, “Tickness measurement of transparent plates by a self-mixing interferometer,” Optics Letters, 35(11), 1844-7 (2010)

A. **Froumkine,** “Couche double. Electrocapillarite´. Surtension.,” Actualit´es Scientifiques, 373, 5-36 (1936)

H. **Fujii**, J. Uozumi and T. Asakura, “Computer simulation study of image speckle patterns with relation to object surface profile,” J. Opt. Soc. Am., 66(11), 1222-36 (1976)

C. **Gabay**, B. Berge, G. Dovillaire and S. Bucourt, “Dynamic study of a Varioptic variable focal lens,” Proc. SPIE 4767, 159-165 (2002)

A. **Gautam**, Y-D. Lee and W-Y. Chung, “ECG Signal Denosing with Signal Averaging and Filtering Algorithm,” in Proc. Third International Conference on Convergence and Hybrid Information Technology (ICCIT 2008), pp.409-415, (2008)

G. **Giuliani**, M. Norgia, “Laser diode linewidth measurement by means of self-mixing interferometry,” IEEE Photonics Technology Letters., 12(8), l028-1030 (2000)

G. **Giuliani**, M. Norgia, S. Donati, and T. Bosch, ”Laser diode self-mixing technique for sensing applications,” J. Opt. A: Pure Appl. Opt., 4, S283-S294 (2002)

F. **Gouaux**, N. Servagent, and T. Bosch “Absolute distance measurement with an optical feedback interferometer,” Applied Optics, 37, 6684-6689 (1998)

D. V. **Griffiths**, I. M. Smith, “Numerical methods for engineers: a programming approach,” Boca Raton: CRC Press. p. 218 (1991)

B.J. **Halkon**, S.J. Rothberg, “Rotor Vibration Measurements Using Laser Doppler Vibrometry: Essential Post-Processing for Resolution of Radial and Pitch/Yaw Vibrations,“ J. Vib. Acoust., 128(1), 8-20 (2006)

Z. **Hashin**, “Analysis of Composite Materials – A Survey,” Journal of Applied Mechanics 50, 481-505 (1983)

J. **Hast**, R. Myllyla, H. Sorvoja, J. Miettinen, "Arterial pulse shape measurement using self-mixing effect in a diode laser," IOP Quantum Electron., 32, 975-982 (2002)

R.A. **Hayes** and B.J. Feenstra, "Video-speed electronic paper based on electrowetting," Nature, 425, 383-385 (2003)

E. **Hecht**, "Optics," 4th edition, Addison Wesley (2002)

B.H.W. **Hendriks**, S. Kuiper, M.A.J. Van As, C.A. Renders and T.W. Tukker, "Electrowetting-based variable-focus lens for miniature systems," Optical Review, 12(3), 255-259 (2005)

I. D. **Henning** and J. V. Collins, "Measures of the semiconductor laser linewidth broadening factor," Elect. Lett., 19, 927 (1983)

J. **Hong**, S. Park, D. Hyun, T. Kang, S. B. Lee, C. Kral, A. Haumer, "Detection and Classification of Rotor Demagnetization and Eccentricity Faults for PM Synchronous Motors," IEEE Trans. Ind. Appl.,48(3), pp. 923 – 932 (2012)

W. **Huang** et al. "Effect of angle of incidence on self-mixing laser Doppler velocimeter and optimization of the system," Optics Communications, 281, 1662-7 (2008)

R. **Juskaitis** and T. Wilson "Direct-view fiber-optic confocal microscope," Optics Letters, 19(22), 1906-1908 (1994)

D.M. **Kane**, K.A. Shore "Unlocking Dynamical Diversity: Optical Feedback Effects on Semiconductor Lasers," John Wiley & Sons (2006)

R. **Kliese**, Yah Leng Lim, K. Bertling, A.A.A Bakar, T. Bosch, A.D. Rakic, "Self-mixing displacement sensing using the junction voltage variation in a GaN laser" Proceedings of the 2008 IEEE Conference on Optoelectronic and Microelectronic, Materials and Devices, 23-25 (2008)

M. H. **Koelink** et al, "Laser doppler velocimeter based on the self-mixing effect in a fiber-coupled semiconductor laser: theory," Applied Optics, 31(18), 3401-3408 (1992)

M.H. **Koelink** et al "Fiber-coupled self-mixing diode-laser Doppler velocimeter: technical aspects and flow velocity profile disturbances in water and blood flows," Applied Optics, 33(24), 5628-5641(1994)

L. **Krehut**, J. Hust, E. Alarousu, and R. Myllyla, "Low cost velocity sensor based on the self-mixing effect in a laser diode," Opto-Electronics Rev., 11(4), 313-319 (2003)

F. **Krogmann**, W. Moench and H. Zappe, “Tunable liquid micro-lens system,” Proc. IEEE in Solid state sensors, actuators and Microsystems, 1, 1014-1017 (2005)

F. **Krogmann**, W. Moench and H. Zappe, “A MEMS-based variable micro-lens system,” J. Opt. A: Pure Appl. Opt., 8, S330-S336 (2006)

R. **Lang** and K. Kobayashi, “External optical feedback effects on semiconductor injection laser properties,” IEEE J. Quant. Elec., 16(3), 347–355 (1980)

C. M. **Lawrence**, D. V. Nelson, E. Udd, T. Bennet, “A Fiber Optic Sensor for Transverse Strain Measurement”, Experimental Mechanics, 39, 202-209 (1999)

S.W. **Lee** and S.S. Lee “Focal tunable liquid lens integrated with an electromagnetic actuator,” Appl. Phys. Lett., 90, 121129-3 (2007)

M. **Liess** et al “A miniaturized multidirectional optical motion sensor and input device based on laser self-mixing,” Measurement science and technology, 13(12), 2001-2006 (2002)

J. **Lin**, M. Bissonnette, , “A New Capacitive Proximity Probe Immune to Electrical Runout,” in Proc. Canadian Machinery Vibration Association, Toronto, 1-5 (1997)

G. **Lippmann**, “Relation entre les ph´enom`enes ´electriques et capillaries,” Ann. Chim. Phys, 5, 494-549 (1875)

C.A. **Lopez**, C. Lee and A.H. Hirsa , “Electrochemically activated adaptive liquid lens,” Appl.Phys.Lett., 87, 134102-2 (2005)

L. **Lu**, K. Zhang, J. Dai, J. Zhu, S. Zhen and B. Yu, “Study of speckle pattern effect for self-mixing laser diodes in vertical-cavity surface-emitting lasers”, Opt. Eng., 49(9), 094301-094301-6 (2010)

R. S. **Medlock**, “Sensors for Mechanical Properties”, J. Phys. E: Sci. Instrum., 16(10), 964 (1983)

S. **Merlo** and S. Donati, “Reconstruction of displacement waveforms with a single-channel laser-diode feedback interferometer,” IEEE J. Quant. Elec., 33(4), 527-531 (1997)

G. **Mourat**, "Etude de diodes laser pour des applications métrologique de la rétro-injection optique," PHD Thesis, INPT-ENSEEIHT, University of Toulouse, France, No. 1561 (2006)

F. **Mugele** and J. Baret, "Electrowetting: from Basics to Applications," J. Phys.: Condens. Matter, 17, R705-R774 (2005)

F.F.M. de **Mul** et al "Self-mixing laser-Doppler velocimetry of liquid flow and of blood perfusion in tissue," Applied Optics, 31(27), 5844-5851 (1992)

A.F. **Naumov**, M.Yu. Loktev, I.R. Guralnik, and G. Vdovin, "Liquid-crystal adaptive lenses with modal control," Opt. Lett., 23(13), 992-994 (1998)

M. **Norgia**, S. Donati and D. D'Alessandro, "Interferometric measurements of displacement on a diffusing target by a speckle tracking technique," IEEE J. Quantum Elec., 37(6), 800-6 (2001)

M. **Norgia**, S. Donati "A displacement-measuring instrument utilizing self-mixing interferometry," IEEE Transactions on Instrumentation and Measurements, 52(6), 1765-1770 (2003)

M. **Norgia**, G. Giuliani and S. Donati "Absolute distance measurement with improved accuracy using uaser diode self-mixing interferometry in a closed loop," IEEE Trans. on Instrumentation and Measurements, 56(5), 1894-1900 (2007)

M. **Norgia**, A. Pesatori, and L. Rovati, "Low-cost optical flowmeter with analog front-end electronics for blood extracorporeal circulators," IEEE Trans. on Instrum. and Meas., 59(5),1233 –1239 (2010)

OkoTech, Flexible Optical B.V. http://www.okotech.com

H. **Oku** and M. Ishikawa, "Rapid Liquid Variable-Focus Lens with 2-ms Response," Proc. IEEE in Lasers & Electro-Optics Society, 947-948 (2006)

Optotune, http://www.optotune.com/

S. **Ottonelli**, F. De Lucia, M. di Vietro, M. Dabbicco, G. Scamarcio, and F. P. Mezzapesa, "A Compact Three Degrees-of-Freedom Motion Sensor Based on the Laser-Self-Mixing Effect" IEEE Photonics Technology Letters, 20(16), 1360 – 1362 (2008)

S. **Ottonelli**, M. Dabbicco, F. de Lucia, M. di Vietro and G. Scamarcio, "Laser Self Mixing Interferometry for Mechatronics Applications," Sensors, 9(5), 3527-3548 (2009)

S.K. **Ozdemir** et al "Compact optical instrument for surface classification using self-mixing interference in a laser diode," Opt. Eng., 40(1), 38–43 (2001)

K. **Petermann**, "External optical feedback phenomena in semiconductor lasers," IEEE Journal of Selected Topics on Quantum Electron., 1(2), 480–489 (1995)

J. **Perchoux** and T. Bosch, "Multimode VCSELs for self-mixing velocity measurements," Proc. Of IEEE sensors 2007 conference, 419-422 (2007)

J. **Perchoux**, L. Compagnolo, Yah Leng Lim, A.D. Rakic, " "Lens-free" self-mixing sensor for velocity and vibrations measurements," COMMAD conference, 43-44 (2010)

Royal **Philips** Electronics, http://www.research.philips.com/

G. **Plantier**, C. Bes and T. Bosch, "Behavioral model of a self-mixing laser diode sensor," IEEE Journal of Quantum Electronics, 41(9), 1157-1167 (2005)

A. **Pruijmboom** et al, "VCSEL-based miniature laser-Doppler interferometer," Proc. of SPIE conf. on Vertical-Cavity Surface-Emitting Lasers, 6908, 690801-1 – 690801-7 (2008)

C. **Quilliet** and B. Berge, "Electrowetting: a Recent Outbreak," Current Opinion in Colloid and Interface Science, 6, 34-39 (2001)

A. V. **Raisanen**, A. Lehto, "Radio Engineering for Wireless Communication and Sensor Applications," Artech House (2003)

S. **Rajagopalan**, W. Roux, T. G. Habetler, and R. G. Harley, "Dynamic Eccentricity and Demagnetized Rotor Magnet Detection in Trapezoidal Flux (Brushless DC) Motors Operating Under Different Load Conditions," IEEE Trans. Power Electron., vol. 22, pp. 2061-2069 (2007)

N. P. **Rea**, T. Wilson, and R. Juskaitis, "Semiconductor laser confocal and interference microscopy," Optics Communications, 125, 158-167 (1996)

H. **Ren** and S.T. Wu, "Variable-focus liquid lens by changing aperture," Appl. Phys. Lett., 86, 211107-3 (2005)

H. **Ren** and S.T. Wu "Adaptive liquid crystal lens with large focal length tunability," Opt. Exp., 14(23), 11292-11298 (2006)

H. **Ren** and S.T. Wu, "Variable focus liquid lens," Opt. Exp., 15(10), 5931-5936 (2007)

S. **Royo**, R. Atashkhooei, and F. Azcona, "A Method of Measuring a Displacement-Related Parameter Using a Laser Self-mixing Measuring System, and a Laser Self-mixing Measuring System", EP1038130 (2010)

S. **Royo**, R. Atashkhooei, J.Urresty, J-R Riba Ruiz, "Sistema y Metodo de medida del desplazamiento transversal de un eje fisico giratorio", P201132100 (2011)

M.J. **Rudd**, "A laser Doppler velocimeter employing the laser as a mixer-oscillator", Journal of Physics, E1, 723-726 (1968)

E. **Sadikoglu**, E. Bilgic, and B. Karaboce, "A laser pistonphone based on self-mixing interferometry for the absolute calibration of measurement microphones," Applied Acoustics, 65, 833-840 (2004)

L. **Scalise**, Y. Yu, G. Giuliani, G. Plantier, and T. Bosch "Self-mixing laser diode velocimetry: application to vibration and velocity measurement," IEEE Transactions on Instrumentation and Measurement, 53, 223-232 (2004)

N. **Servagent**, F. Gouaux and T. Bosch "Measurements of displacement using the self-mixing interference in a laser diode," J. Opt., 29, 168-173 (1998)

J. **Shieh**, J.E. Huber, N.A. Fleck and M.F. Ashby, "The Selection of Sensors," Progress in Materials Science, 46, 461-504 (2001)

S. **Shinohara**, A. Mochizuki, H. Yoshida and M. Sumi, "Laser Doppler velocimeter using the self-mixing effect of a semiconductor laser diode", Applied Optics, 25, 1417-1419 (1986)

Y. **Sun**, Y. Yu, W. Fan, and J. Xi, "FPGA based filter design for self-mixing interferometry signals," Proc. of SPIE conf. on Optical Instr. And Tech.: Opt. Sensors and Appl., 8199, 819909-1 – 819909-7 (2011)

N. **Takahashi**, S. Kakuma, and R. Ohba "Active heterodyne interferometric displacement measurement using optical feedback effects of laser diodes," Optical Engineering, 35, 802–807 (1996)

G.H.M. van **Tartwijk** and D. Lenstra, "Semiconductor lasers with optical injection and feedback," Quantum Semiclass. Opt., 7, 87-143 (1995)

R. W. **Tkach** and A. R. Chraplyvy, "Regimes of feedback effects in 1.5 pm distributed feedback lasers," Journal of Lightwave Technology, LT-4(11), 1655-1661 (1986)

J. **Urresty**, R. Atashkhooei, J-R Riba Ruiz, L. Romeral, S. Royo "Mechanical Effects of Demagnetization Faults in Permanent Magnet Synchronous Motors", IEEE Transaction on Industrial Electronics, 60(8), 3454-3461 (2013)

Varioptic SA, http://www.varioptic.com

A. **Villafranca**, G. Giuliani, S. Donati, and I. Garces, "Investigation on the linewidth enhancement factor of multiple longitudinal mode semiconductor lasers," proc. of SPIE conf. of semiconductor lasers and laser dynamics, 6997, 699719-1 – 699719-9 (2008)

W.M. **Wang**, W.J.O. Boyle, K.T.V. Grattan, and A.W. Palmer, "Self-mixing interference in a diode laser: Experimental observations and theoretical analysis," Applied Optics, 32 (9), 1551-1558 (1993)
W.M. **Wang**, et al "Self-mixing interference inside a single-mode diode laser for optical sensing applications," IEEE, Journal of Lightwave Technology, 12 (9), 1577-1587 (1994)

W. **Wang**, P. L. Wong, J. B. Luo and Z. Zhang, "A new optical technique for roughness measurement on moving surface," Tribology International, 31(5), 281-287 (1998)

M. **Wang**, G. Lai "Self-mixing microscopic interferometer for the measurement of microprofile," Opt. Comm., 238, 237-244 (2004)

L. **Wei**, J.F. Chicharo, Y. Yu, J. Xi, "Pre-processing of signals observed from laser diode self-mixing interferometries using neural networks," IEEE International Symposium on Intelligent Signal Processing (WISP 2007), 1-5 (2007)

R.W.C.G.R. **Wijshoff**, M. Mischi, J. Veen, A.M. Van der Lee, and R.M. Aarts, "Reducing motion artifacts in photoplethysmograms by using relative sensor motion: phantom study," J. Biomedical Opt., 17(11), 117007-1-117007-15 (2012)

J. S. **Wilson**, "Sensor technology handbook" Elsevier Inc. (2005)

Y. **Yanguang**, G. Giuliani, and S. Donati, “Measurement of the linewidth enhancement factor of semiconductor lasers based on the optical feedback self-mixing effect,” IEEE Photon. Technol. Lett., 16(4), 990–992 (2004)

Y. **Yu**, G. Giuliani, S. Donati, "Measurement of the linewidth enhancement factor of semiconductor lasers based on the optical feedback self-mixing effect," IEEE Photon. Technol. Lett., 16, 990-992 (2004)

Y. **Yu**, J. Xi, and J.F. Chicharo, “Improving the performance in an optical feedback self-mixing interferometry system using digital signal pre-processing,” IEEE International Symposium on Intelligent Signal Processing (WISP 2007), 1-6 (2007)

U. **Zabit**, T. Bosch, and F. Bony, “Adaptive transition detection algorithm for a self-mixing displacement sensor,” IEEE Sensors Journal, 9(12), 1879 – 1886 (2009)

U. **Zabit**, T. Bosch, F. Bony and A. D. Rakic, “A self-mixing displacement sensor with Fringe-loss compensation for harmonic vibrations”, IEEE Photonics Technology Letters, 22(6), 410 – 412 (2010)

U. **Zabit**, “Optimization of a self-mixing laser displacement sensor” PHD Thesis, INPT-ENSEEIHT, University of Toulouse, France (2010b)

U. **Zabit**, R. Atashkhooei, T. Bosch, S, Royo, F. Bony and A. D. Rakic, “Adaptive self-mixing vibrometer based on a liquid lens,” Optics Letters, 35(8), 1278-80 (2010c)

8. List of publications

International Journals with Peer Review

[J1] U. Zabit, **R. Atashkhooei**, T. Bosch, S, Royo, F. Bony and A. D. Rakic, "Adaptive self-mixing vibrometer based on a liquid lens," Optics Letters, 35(8), 1278-80, 2010. DOI: 10.1364/OL.35.001278 (with 14 citations)

[J2] **R. Atashkhooei**, S. Royo, F.J. Azcona, "Dealing with Speckle Effects in Self-mixing Interferometry Measurements", IEEE Sensors J., 13(5), 1641-7, 2013. DOI: 10.1109/JSEN.2013.2240156

[J3] J. Urresty, **R. Atashkhooei**, J-R Riba Ruiz, L. Romeral, S. Royo "Mechanical Effects of Demagnetization Faults in Permanent Magnet Synchronous Motors", IEEE Transaction on Industrial Electronics, 60(8), 3454-3461, 2013. DOI: 10.1109/TIE.2012.2213565

[J4] **R. Atashkhooei**, J. Urresty, S. Royo, J-R Riba Ruiz, L. Romeral, "Runout Tracking in Electric Motors by Self-mixing Interferometry", IEEE Transaction on Mechatronics, in press, 2013. (Early access article). DOI: 10.1109/TMECH.2012.2226739

Recently Submited:

[J5] **R. Atashkhooei**, S. royo, J. Pladellorence Malofre "Adaptive Auto-focusing Technique for Real-time Speckle Control in Optical Feedback Interferometry", Sensors actuators A, (2013)

[J6] F.J. Azcona, **R. Atashkhooei**, S. Royo, J. Mendez, A. Jha, "A Nanometric Displacement Measurement System Using Differential Optical Feedback Interferometry", Photo. Tech. Lett. (2013)

Patents

[P1] S. Royo, **R. Atashkhooei**, and F. Azcona, "A Method of Measuring a Displacement-Related Parameter Using a Laser Self-mixing Measuring System, and a Laser Self-mixing Measuring System", EP1038130 (15/10/2010).

[P2] S. Royo, **R. Atashkhooei**, J.Urresty, J-R Riba Ruiz, "Sistema y Metodo de medida del desplazamiento transversal de un eje fisico giratorio", P201132100 (23/12/2011).

Conferences

[C1] **R. Atashkhooei**, U. Zabit, S. Royo, T. Bosch and F. Bony, "Adaptive optical head for industrial vibrometry applications," Proc. SPIE 8082, 80821W, Munich 2011. (Oral)

[C2] **R. Atashkhooei**, U. Zabit, S. Royo, F. Azcona and I. Sergievskaya, "Adaptive feedback control in Self-mixing Interferometry Using Active Optical element," Proc. AOIM (Adaptive Optics for Industry and Medicine) 8th Int. Conf., Murcia 2011. (Poster)

[C3] **R. Atashkhooei**, S. Royo, F. Azcona and U. Zabit, "Analysis and Control of Speckle Effects in Self-mixing Interferometry, " in Proc. IEEE sensors, Limerick (Ireland), 28-31 Oct. 2011, pp. 1390-1393 (Oral).

[C4] **R. Atashkhooei**, F. Azcona, S. Royo, L.G. Espert, "Optical feedback interferometry for measuring dynamic stress deformation of beams," in Proc. AIVELA 2012, Vol. 1457, Ancona (Italy), Jun. 2012, pp. 132-138 (Oral).

[C5] F.J. Azcona, **R. Atashkhooei**, S. Royo, J. Mendez, A. Jha, "A method to measure sub nanometric amplitude displacements based on optical feedback interferometry," in Proc. SPIE 8789, Munich 2013. (Oral)